

## ABSTRACT

Title of Dissertation:                   NANOSCALE THERMODYNAMICS OF  
MECHANOSENSITIVE ION CHANNELS  
AND THEIR ROLE IN THE MECHANISM OF  
OSMOTIC FITNESS OF MICROBES

Ugur Cetiner, Doctor of Philosophy, 2018

Dissertation Directed By:           Professor Sergei Sukharev  
Department of Biology

Bacterial mechanosensitive channels are major players in cells' ability to cope with hypo-osmotic stress. Excess turgor pressure due to fast water influx is reduced as the channels, triggered by membrane tension, open and release osmolytes. In bacteria, the bulk release of ions and other osmolytes is mainly mediated by two families of mechanosensitive channels: MscS and MscL. The MscL family channels form large non-selective pathways in the membrane and gate near the lytic tension. In this way, they act as a final back up mechanism against osmotic downshock. MscS family channels require less tension to open and display great diversity in structure and functionality. Chapter 2 describes the first multifaceted phenomenological study of the emergency osmolyte release system in wild type *Pseudomonas aeruginosa* in comparison with *E.coli*. We recorded the kinetics of cell equilibration reported by light scattering responses to osmotic up- and down-shocks using the stopped flow

technique. We also performed the first electrophysiological characterization of the mechanosensitive ion channels in *Pseudomonas aeruginosa*. We presented a quantitative biophysical description of “osmotic fitness” which would be of interest to microbiologists, epidemiologists, ecologists and general environmental scientists. Chapter 3 presents the combined theoretical and experimental analysis of the full functional cycle of the bacterial channel MscS, which plays a major role in osmotic adjustments and environmental stability of most bacteria. We modeled MscS gating as a finite state continuous-time Markov chain and obtained analytical expressions for the steady state solution and the inactivated state area (which is experimentally hard to determine). In Chapter 4, we derived a general formalism to extract the free energy difference between the closed and open states of mechanosensitive ion channels ( $\Delta F$ ) from non-equilibrium work distributions associated with the channels’ gating. Our new approach bridges the gap between recent developments in non-equilibrium thermodynamics of small systems and ion channel biophysics. Our study also serves as an experimental verification of non-equilibrium work relations in a biological system. Therefore, the results in this thesis are sufficiently general and would be of interest to a broad community.

NANOSCALE THERMODYNAMICS OF MECHANOSENSITIVE ION  
CHANNELS AND THEIR ROLE IN THE MECHANISM OF OSMOTIC  
FITNESS OF MICROBES

by

Ugur Cetiner

Dissertation submitted to the Faculty of the Graduate School of the  
University of Maryland, College Park, in partial fulfillment  
of the requirements for the degree of  
Doctor of Philosophy  
2018

Advisory Committee:  
Professor Sergei Sukharev, Chair  
Professor Marco Colombini  
Professor Christopher Jarzynski  
Professor Garegin Papoian  
Professor Kimberly Stroka

© Copyright by  
Ugur Cetiner  
2018

# Preface

## **Declaration of intent to use author's own previously published text**

The main text and figures in their entirety for:

Chapter 2: Tension-activated channels in the mechanism of osmotic fitness in *Pseudomonas aeruginosa*

Chapter 3: Spatiotemporal relationships defining the adaptive gating of the bacterial mechanosensitive channel MscS

And

Chapter 4: Recovery of equilibrium free energy from non-equilibrium thermodynamics with mechanosensitive ion channels in *E. coli*

Were used and only slightly modified for accessibility and formatting purposes. Full citations are as follows:

- **Uğur Çetiner**, Ian Rowe, Anthony Schams, Christina Mayhew, Deanna Rubin, Andriy Anishkin, Sergei Sukharev. “Tension-activated channels in the mechanism of osmotic fitness in *Pseudomonas aeruginosa*” *The Journal of General Physiology* May 2017, 149 (5) 595-609; DOI: 10.1085/jgp.201611699
- **Uğur Çetiner**, Andriy Anishkin, Sergei Sukharev. “Spatiotemporal relationships defining the adaptive gating of the bacterial mechanosensitive channel MscS” *European Biophysics Journal* 2018  
<https://doi.org/10.1007/s00249-018-1303-5>
- **Uğur Çetiner**, Oren Raz, Sergei Sukharev, Christopher Jarzynski. “Recovery of equilibrium free energy from on-equilibrium thermodynamics with mechanosensitive ion channels in *E. coli*” bioRxiv 229088; doi: <https://doi.org/10.1101/229088>

## Dedication

*To my mother Huri etiner and my partner Olga Karpekina*

## Acknowledgements

First and foremost, I would like to thank my advisor, Dr. Sergei Sukharev for his patience and thoughtful advice. Without his contribution, I would not be where I am today. I would also like to express my most sincere gratitude to Dr. Christopher Jarzynski for his support and for his written recommendations. I feel also very fortunate to have had the chance to interact and collaborate with the former members of his research group: Drs. Yiğit Subaşı and Oren Raz. They inspired me in many ways and I learned a lot from them.

To my committee members, Dr. Jarzynski, Dr. Stroka, Dr. Papoian and Dr. Colombini, I thank you for the guidance and other help you have provided along the way.

My gratitude extends to Dr. Ian Rowe for teaching me how to patch clamp and Stephanie Sansbury for helping me with micro- and molecular biology part of this research.

To the members of Sukharev Lab, former and present: Christina Mayhew, Deanna Rubin, Anthony Yasmann, Anthony Schams, Madolyn Britt, Joseph Maramba, Kristen Ramsey and Dr. Andriy Anishkin, I thank you for your support and friendship. Nothing could have been completed without your help.

I am indebted to the U.S. Department of Education for GAANN, “Mathematics in Biology” Fellowship.

Lastly, I would like to thank my family for their constant help and support.

# Table of Contents

<b>Preface</b> .....	<b>ii</b>
<b>Dedication</b> .....	<b>iii</b>
<b>Acknowledgements</b> .....	<b>iv</b>
<b>Table of Contents</b> .....	<b>v</b>
<b>Tables and Figures</b> .....	<b>vii</b>
<b>Chapter 1: Introduction</b> .....	<b>1</b>
<u>Mechanosensation</u> .....	1
<u>Bacterial Mechanosensitive Ion Channels</u> .....	2
Osmoregulation.....	2
Electrophysiology and Patch-Clamp Experiment.....	6
Relating MscS channel structure with its functional cycle.....	9
<u>Statistical Mechanics of Mechanosensitive Ion Channel Gating</u> .....	13
Equilibrium Picture.....	13
Markov Chain Models of Ion Channel Gating .....	15
<u>Non-equilibrium Work Relations</u> .....	20
The Clausius Inequality and Macroscopic Thermodynamics .....	22
Hamiltonian Derivation .....	28
Markov Jump Process .....	31
<u>Problem Statements and Questions</u> .....	37
Tension-activated channels in the mechanism of osmotic fitness in <i>Pseudomonas aeruginosa</i> .....	37
Spatiotemporal relationships defining the adaptive gating of mechanosensitive ion channel MscS.....	38
Recovery of equilibrium free energy from non-equilibrium thermodynamics with mechanosensitive ion channels in <i>E.coli</i> .....	40
<b>Chapter 2: Tension-activated channels in the mechanism of osmotic fitness in <i>Pseudomonas aeruginosa</i></b> .....	<b>42</b>
<u>Abstract</u> .....	42
<u>Introduction</u> .....	43
<u>Materials and Methods</u> .....	47
Strains and media .....	47
Stopped-flow experiments. ....	48
<u>Results</u> .....	53
<i>P. aeruginosa</i> versus <i>E. coli</i> : osmotic survival and kinetics of osmolyte and water exchange.....	53
<i>E. coli</i> and <i>P. aeruginosa</i> spheroplast preparation, patch-clamp channel activation in situ.....	59
Genomic databases predict one MscL and two MscS-like channels in <i>P. aeruginosa</i> .....	64
Determination of tension sensitivities for <i>P. aeruginosa</i> MscS-like channels and their spatial and energetic parameters for activation. ....	66



<b>Chapter 3: Spatiotemporal relationships defining the adaptive gating of the bacterial mechanosensitive channel MscS .....</b>	<b>77</b>
<u>Abstract</u> .....	77
<u>Introduction</u> .....	78
The Model .....	82
Experimental electrophysiological recordings and data treatment .....	83
Estimation of the in-plane area for crystallographic structures and molecular models. ....	84
<u>Results</u> .....	86
<u>Discussion</u> .....	105
<b>Chapter 4: Recovery of equilibrium free energy from non-equilibrium thermodynamics with mechanosensitive ion channels in E. coli .....</b>	<b>113</b>
<u>Abstract</u> .....	113
<u>Introduction</u> .....	114
<u>Experimental and Theoretical Setup</u> .....	119
<u>Results</u> .....	125
<u>Discussion</u> .....	128
<u>Material and Methods</u> .....	133
<b>Chapter 5: General conclusions and future directions.....</b>	<b>135</b>
<u>Conclusion 1</u> .....	136
<u>Conclusion 2</u> .....	137
<u>Conclusion 3</u> .....	145
<b>Chapter 6: Supplement.....</b>	<b>147</b>
<u>Tension-activated channels in the mechanism of osmotic fitness in Pseudomonas aeruginosa</u> .....	147
<u>Spatiotemporal relationships defining the adaptive gating of the bacterial mechanosensitive channel MscS</u> .....	158
<u>Recovery of equilibrium free energy from non-equilibrium thermodynamics with mechanosensitive ion channels in E.coli</u> .....	168
Bibliography .....	176

# Tables and Figures

## Chapter 1

Figure 1.1. Bacterial response to osmotic down-shock. ....	4
Figure 1.2. Cartoon of experimental set up for the excised patch configuration.....	7
Figure 1.3. Phase contrast images of the spheroplasting process of <i>Pseudomonas aeruginosa</i> .....	8
Figure 1.4. Crystal structures of the mechanosensitive channel proteins MscL and MscS.. ....	12
Figure 1.5. Two-state Boltzmann model for the gating of a mechanosensitive ion channel... ..	14
Figure 1.6. Stretching a rubber band.....	22
Figure 1.7. Macroscopic system vs microscopic system. ....	26
Figure 1.8. The distribution of work values obtained from a thermodynamic process applied to a small system, e.g., MscS. ....	30
Figure 1.9. A single realization of the protocol and the corresponding trajectory in the phase space for a Markov jump process... ..	32

## Chapter 2

Figure 2.1. Osmotic survival correlates with osmolyte exchange rates.....	56
Figure 2.2. Stopped-flow recordings of small-angle light scattering upon mixing of suspensions of PA (A) or EC (B) grown in MLB (250 mOsm) with 10-fold excess of higher-osmolarity media.. ....	58
Figure 2.3. Steps in the giant spheroplast preparation as viewed by DIC microscopy.. ..	60
Figure 2.4. Pressure ramps applied to excised patches of native MS channel populations in EC and PA produce comparable conductance responses.....	61
Table 2.1. Numbers and densities of channels in native inside-out patches from ramp traces recorded from PE (PA14) and EC (Frag1) giant spheroplasts.. ....	62
Figure 2.5. The low- and high-threshold sub-populations of native channels in <i>E. coli</i> (A, B) and <i>P. aeruginosa</i> (C, D) exhibit distinctive adaptive behaviors.....	63
Figure 2.6. Current-to-voltage relationships for unitary currents measured for PaMscL, PaMscS-1 and PsMscS-2. ....	65
Figure 2.7. Midpoint determination of <i>P. aeruginosa</i> MscS-like channels using MscL as an intrinsic tension gauge.. ....	66
Figure 2.8. The inactivation and recovery of PaMscS1 and PaMscS2.....	69
Figure 2.9. Functional analysis of PaMsc-1 mutants using step protocols shows conservation of elements involved in inactivation between <i>P. aeruginosa</i> and <i>E. coli</i> . ....	70

Table 2.2. The summary of experimentally determined parameters for the two PaMscS channels in comparison to <i>E. coli</i> MscS .....	70
---	----

Figure 2.10. Relative ability of <i>P. aeruginosa</i> MS channels to rescue <i>E. coli</i> MJF641 from osmotic down shock.....	71
--	----

### Chapter 3

Figure 3.1. The discrete conformational state space of allowed transitions indicated by the experiments .....	87
Figure 3.2. Exploration of time scales characteristic for the separate $C \leftrightarrow O$ and $C \leftrightarrow I$ transitions in MscS populations.....	91
Figure 3.3. MscS responses to triangular pressure ramps.....	94
Figure 3.4. Probing the Open $\rightarrow$ Closed transition by the pulse-step protocol... ..	96
Figure 3.5. Probing the Closed $\leftrightarrow$ Inactivated transition.....	99
Table 3.1. The energy profiles for MscS transitions were tested experimentally and compared with values from literature.. ..	100
Figure 3.6. Comparison of experimental steady state MscS inactivation with 3-state model.....	102
Figure 3.7. The spatial scale for inactivation in <i>Pseudomonas aeruginosa</i> PaMscS-1 .....	103
Figure 3.8. The rate dependency of MscS inactivation .....	105
Figure 3.9. The reconstructed energy landscape predicted for MscS in a relaxed membrane ( $\gamma = 0$ ) and under tension $\gamma_{0.5} = 7.85$ mN/m, at which open and closed states are equally populated. ....	108

### Chapter 4

Figure 4.1. Bacterial response to osmotic down-shock. ....	116
Figure 4.2. Patch-clamp applied to giant bacterial spheroplasts has been the most informative way of obtaining functional characteristics of bacterial mechanosensitive channels. ....	120
Figure 4.3. The gating (red) and closure (blue) of a single channel in response to linear increase and decrease of the membrane tension with the same rate.....	124
Figure 4.4. Histograms of the work distributions at $3 k_B T / nm^2 s^{-1}$ .....	126
Table 4.1. Summary of Results.....	127
Figure 4.5. An inevitable complication due to indistinguishability of single channel events in the patch clamp experiments. ....	132

## Chapter 5

Figure 5.1. Size dependent effect of crowding agents on the gating properties of the EcMscS channels .....	139
Figure 5.2. VcMscS-1 activity under molecular crowding.....	143
Figure 5.3. MscL channels are insensitive to macromolecular crowding.....	145

## Supplement

### Tension-activated channels in the mechanism of osmotic fitness in *Pseudomonas aeruginosa*

Figure S1. Unadjusted stopped-flow scattering traces obtained after subtraction of stray light signal.....	151
Figure S2. Examples of fitting curves (black) overlaid with experimental traces obtained with PA-14 cultures.....	152
Figure S3. Examples of fitting curves (black) overlaid with experimental traces (red) obtained with EC (Frag-1) cultures.....	153
Figure S4. Pressure ramps applied to excised patches of EC (A, C) always reveal a larger MscS population as compared to PA (B, D).....	154
Figure S5. A two-state energy diagram for a tension-gated channel.....	155
Table S.1. <i>Pseudomonas aeruginosa</i> PA-14 putative proteins homologous to known MS channel proteins of <i>Escherichia coli</i> .....	156
Figure S6. Alignments of <i>E coli</i> and PA MS channels orthologs.....	157

### Spatiotemporal relationships defining the adaptive gating of the bacterial mechanosensitive channel MscS

Figure S1. The characteristics of MscS inactivation observed in an excised patch containing approximately 200 MscS channels.....	158
Figure S2. Locking the channels in the open state.....	159
Figure S3. <i>E. coli</i> MscS inactivation as a function of time and tension measured by pulse-step-pulse protocol where the step duration was varied from 5s to 90s.....	160
Figure S4. The representative crystal structures and structural models representing the MscS functional cycle.....	167

Recovery of equilibrium free energy from non-equilibrium thermodynamics with mechanosensitive ion channels in E.coli

Figure S1. Two-state model of MscS gating..... 168  
Figure S2. An Edge Detector program ..... 169  
Figure S3. Semi-logarithmic plot of the ratio of the work distributions in the Fig 4 as a function of work provides the Crooks' estimate for the free energy. .... 170  
Figure S4. Overlapping Distributions Method..... 171  
Figure S5. Histograms of the work distributions. .... 172  
Figure S6. The work distributions obtained from two different membranes for the typical experimental protocol... ..... 173  
Table S.1. Reproducibility of work distributions..... 173  
Figure S7. Histogram of work distributions obtained from a different experimental protocol ..... 174  
Table S.2. Histogram of work distributions obtained from a different experimental protocol.. ..... 175  
Table S.3. A sanity check for  $\Delta A$  ..... 175

## List of Abbreviations

MS – mechanosensitive

MscS – mechanosensitive channel of small conductance

MscL – mechanosensitive channel of large conductance

TM – transmembrane helices

WT – wild type

IPTG - Isopropyl thiogalactopyranoside

HEPES - 4-(2-hydroxyethyl)-1-piperazineethanesulfonic acid

HSPC – high speed pressure clamp

LB - Luria Bertani medium

EDTA – Ethylenediaminetetraacetic acid

BSA – bovine serum albumin

MD – molecular dynamics

DB – detailed balance

NESS – non-equilibrium steady state

pN – piconewton

mN – millinewton

EC- *Escherichia coli*

PA- *Pseudomonas aeruginosa*

LR – linear response

# Chapter 1: Introduction

## Mechanosensation

All living systems are capable of exchanging information with the ambient environment. This ubiquitous process is essential for survival and homeostasis. In order to convert different types of mechanical stresses into electrochemical signals, cells are equipped with a quite diverse set of force-sensing molecules. The necessary condition for mechanosensation is that the force-sensing molecule undergoes a conformational change and occupies a larger membrane-displaced area in the open configuration [1]. Thus, in the presence of membrane tension, the open state is energetically more favorable and the transition from the closed to open state (gating) allows ions to flow down their electrochemical gradient across the membrane [2]. We should note that mechanosensation is not restricted to conformational changes of force sensing molecules. There are other ways to translate mechanical stimuli into biological responses [3–5]. For example, endothelial cells use surface glycocalyx to sense the shear stress associated with blood flow [4,6] whereas integrin-mediated adhesions transmit the mechanical stress between the extracellular matrix and actin cytoskeleton [7,8]. This mechanochemical coupling between extracellular matrix and actin cytoskeleton plays an important role in cell migration, differentiation and homeostasis [9]. However, mechanosensitive (MS) ion channels are the best studied force-sensing molecules to date and they are found in all three domains of life: Bacteria, Archaea, and Eukarya [10,11].



In higher organisms, mechanosensitive ion channels play key roles in touching, sensing, and hearing. Examples of such channels in higher organisms include the epithelial sodium channels, DEG/ENaC family channels found in many animals (metazoans) that participate in mechanotransduction in neuronal cells [12], transient receptor potential (TRP) channels involved in sensations of pain, hotness, warmth or coldness, pressure, and vision [13]. Recently identified Piezo family membrane proteins are the key participants in various physiological processes that involve mechanosensitivity, such as touching, breathing, and vascular development [14–16]. Even though higher plants (*A. thaliana*) do not have Deg/ENaC and TRP family channels, three families of plant MS ion channels have been identified: the MscS-like (MSL), Mid1-complementing activity (MCA), and two-pore potassium (TPK) families. These mechanosensitive ion channels in plants are likely to participate in the sensation of diverse mechanical stimuli such as gravity, touch, and osmotic pressure [17–20]. Interested readers are referred to many excellent reviews on mechanosensation in higher organisms [3,19,21–23].

### *Bacterial Mechanosensitive Ion Channels*

#### Osmoregulation

In terms of the habitat and species diversity, microbes, undoubtedly, are the most successful and important organisms on the planet. They are the most prevalent cell types in the human body such that the number of bacterial cells ( $10^{13}$ ) outnumber our own cells ( $10^{12}$ ). In the presence of sufficient food, microbes can double in every 20 minutes or so yielding approximately  $2^{288}$  individuals in four

days [24]. This number is greater than the number of protons ( $2^{266}$ ) that exist in the observable universe. The free transfer of hereditary material from one to another empowers them with great adaptability and resilience to encounter environmental changes, and thus they can be found in almost all of the harshest niches on Earth [24,25]. The delusion that we have some privileged position in the evolutionary history is definitely challenged by these tiny organisms. Here, - in a diverse microcosm- we narrow the scope of our attention to bacterial osmoregulation and briefly introduce how microbes cope with osmotic stress.

Bacterial cells are surrounded by the cytoplasmic membrane, which is responsible for maintaining all vital solutes as well as ionic and electrical gradients. The cell is covered by an elastic cell wall made of covalently cross-linked peptidoglycan, which mechanically restrains swelling (Fig. 1.1). Gram-negative bacteria considered here have an additional outer membrane covering the cell, which is perforated with pore-forming proteins (porins) mediating solute diffusion. All bacteria are capable of accumulating high concentrations of solutes in their cytoplasm to maintain positive turgor pressure necessary for the maintenance of cell volume and shape, as well as cell growth and division. In Gram-negative bacteria (such as *E. coli*), under typical laboratory culturing conditions, turgor pressure is estimated to be between 1 and 4 atm [26,27].

Bacteria often face sudden changes in the osmolarity of their surroundings. In order to keep up with osmotic fluctuations in the environment, bacteria follow different strategies. Under hyperosmotic conditions, when water leaves the cell and turgor pressure drops, bacteria accumulate compatible osmolytes either through

synthesis or through uptake. In doing so, bacteria utilize multiple transport mechanisms in order to restore the positive turgor needed for growth [28]. However, when external osmolarity suddenly drops, such as when microbes get caught in the rain or thrown into a lower osmolarity medium during a hand-pipetting experiment in a laboratory, the water influx generates large turgor pressure inside the cell that stretches the elastic peptidoglycan layer. This happens in a matter of milliseconds [28,29]. When the inner membrane completely unfolds, it starts experiencing tension.

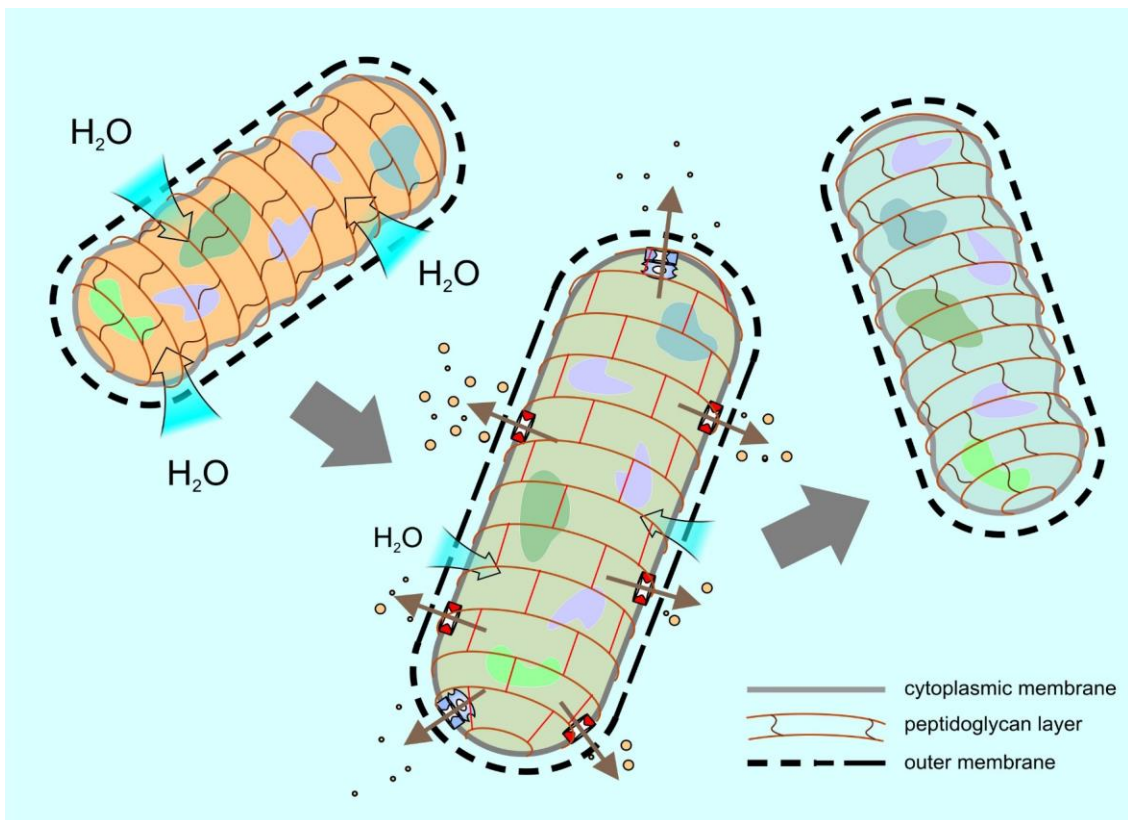


**Figure 1.1. Bacterial response to osmotic down-shock.** Water influx is accompanied by elastic deformation of the cell wall and stretching the cytoplasmic (inner) membrane. Mechanosensitive channels open and release small osmolytes. When tension and volume return to normal, channels close. (Courtesy of A. Anishkin).

This tension drives the opening of MS channels, which dissipate the osmotic gradient and release water together with osmolytes (Fig. 1.1). Under strong and abrupt osmotic down-shock, the inner membrane may stretch the peptidoglycan layer beyond a certain threshold and cause a local break. The membrane may protrude out, forming a “bleb”, and then rupture [30]. Both outcomes will lead to cell death. The amount of tension in the membrane under a given osmotic gradient will depend on the amount of excess bilayer stored inside the cell and the elasticity and degree of cell wall distension (stretch). This model also implies that the maximum tension that the membrane might experience during a down-shock (which can be either below or above the limit of mechanical stability) will depend on the competition between the rate of osmotically-driven water influx, the speed of channel activation, and the overall rate of osmolyte efflux through MS channels. If the channels are able to dissipate the osmotic gradient quickly enough, the cell will be rescued. If the water flow and associated tension buildup overwhelm the efflux system, the cell will burst.

Most molecular components mediating water and solute fluxes have been identified and partially characterized primarily in one bacterial species, *E. coli*. Water influx accompanying osmotic down-shock takes place directly through the lipid bilayer and is augmented by the presence of ubiquitous water channels (aquaporins) [31–33]. Seven tension-activated channel species (MscL, MscS and five other proteins with different degree of homology to MscS) have been identified in the genome of *E. coli*. These genes have been cloned and functionally characterized [34,35]. Using multiple knock-out strains with various channels removed, it has been shown that the low-threshold (5-7 mN/m) mechanosensitive

channel of small conductance (MscS, 1 nS) and the high-threshold (10-14 mN/m) mechanosensitive channel of large conductance (MscL, 3.1 nS) are the major players in mediating osmolyte release, pressure adjustment and rescuing. Expression of either of them extends the range of tolerable osmotic down-shocks about four fold (from 300 mOsm to 1200 mOsm) [35].

### Electrophysiology and Patch-Clamp Experiment

It has been long known that *Escherichia coli* jettisons internal osmolytes upon an osmotic down-shock. In 1962, Britten and McClure reported that during a 1:100 aqueous dilution of culture media, bacteria can release ~95% of their total amino acid pool and remain completely viable [36]. They assumed that the metabolites are released when “the cell passes through a transient state in which the structures (e.g. the cytoplasmic membrane and/ or the cell wall) are distended.” However, discovery of mechanosensitive ion channels- the emergency valves that are responsible for solute efflux- took almost another quarter-century.

The patch clamp technique was developed by Erwin Neher and Bert Sakmann in the late 70s and early 80s [37–39]. It enables researchers to characterize the electrophysiological properties of ion channels by clamping a piece of a membrane as a giga-ohm seal in a polished glass micropipette (Fig. 1.2).

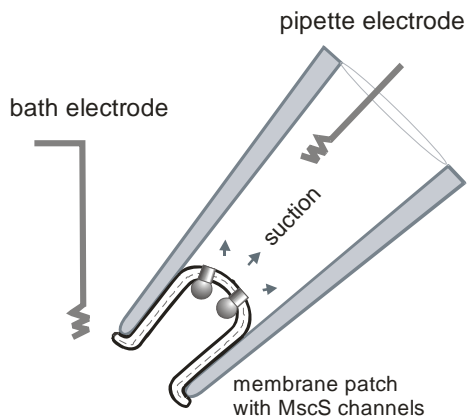


**Figure 1.2. Cartoon of experimental set up for the excised patch configuration.**

Tightly sealed membrane provides an electrical isolation. However, activation of single channels in response to membrane tension forms conducting pathways which can be monitored with pico-ampere precision. Observations of discrete currents passing through individual channels made patch-clamp essentially the very first single-molecule technique.

The high resistance of the seal provides an electrical isolation across the membrane. However, conducting pathways can be generated by activation of mechanosensitive ion channels in response to applied tension. Patch clamp experiments can be executed in various configurations (whole cell, excised patch, cell-attached mode etc) to examine the transport of ions and charged solutes across biological membranes. The wide variety of data acquisition modes provides a great deal of flexibility to the study of ion channel kinetics.

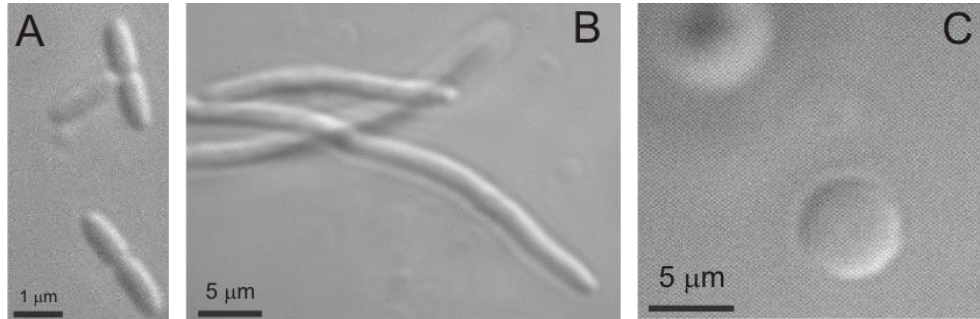


**Figure 1.3. Phase contrast images of the spheroplasting process of *Pseudomonas aeruginosa*.** (A) Intact *Pseudomonas aeruginosa* cells. (B) Carbenicillin induced filaments (also called snakes) and (C) Lysozyme-treated filaments yield giant spheroplasts.

Bacterial cells, however, are small and also surrounded by a thick cell wall, and therefore the cytoplasmic membrane of intact bacteria cannot be studied with the patch-clamp technique. A significant advance was made in 1985 when Ruthe and Adler grew *E. coli* cells in the presence of cephalixin. Cephalixin inhibits cytokinesis and causes cells to grow as long filamentous snakes. The snaked cells are then treated with lysozyme to digest the cell wall and collapse the filament into a sphere, creating giant spheroplasts in the range of 2-10  $\mu\text{m}$  in diameter. Fig.1.3 describes the spheroplasting process of *Pseudomonas aeruginosa* cells\*.

The long-awaited breakthrough finally came in 1987, when Martinac and co-workers recorded the first mechanosensitive ion channel activity in native *E. coli* membranes via patch-clamp technique. Electrical recordings from the native patches of *E. coli*, obtained from spheroplasts, revealed that the cytoplasmic membrane

---

\* The procedure of *P. aeruginosa* giant spheroplast preparation is similar to *E. coli*, but with two modifications: (i) since *P. aeruginosa* is completely insensitive to cephalixin, the *P. aeruginosa* filaments were grown in the presence of 0.2 mg/ml carbenicillin (1.5–2 h), (ii) the spheroplasting reaction required double amount of lysozyme and an extended reaction time (15–20 min) compared with *E. coli*.

harbors at least two distinct tension-activated channels: a mechanosensitive channel with very large conductance (MscL) and one with a smaller conductance (MscS) [40–42]. Subsequently, the *mscL* gene was cloned through a brute force biochemical purification experiment by Sukharev in 1994 [34]. Later, using homology to the potassium efflux protein KefA, Levina et al. and coworkers isolated the *yggB* gene which encodes for MscS [35], the protein responsible for the bulk of the 1 nS conductance present in the wild-type *E. coli* (Fig.1.4).

Another channel with a large amount of C-terminal homology to MscS, named MscK, was identified along with its gene *kefA* [35]. Although, both MscK and MscS have similar single channel conductance and slightly anionic preference, MscK gates at lower tension values than MscS [35,43]. Either MscS or MscL can single-handedly rescue MscS/MscL double null cells from osmotic down-shocks, whereas MscK does not significantly contribute to cells' survival under similar conditions [23,35].

#### Relating MscS channel structure with its functional cycle

MscS is a homoheptamer of 286 amino acid subunits with a crystal structure resolved at 3.9 angstroms [44]. Each subunit has three transmembrane (TM) helices. The C-termini from all subunits come together to form a hollow cytoplasmic cage domain (Fig.1.4 -right). The first crystal structure showed a 30° splay of TM1 and TM2 relative the pore axis. The hydrophobic gate of the channel is formed by two rings of leucines (L105, L109) on TM3 segments. One of the key features of the MscS crystal structure is the sharp kink in the pore-forming TM3 helices at glycine 113. This kink divides TM3 into two segments: TM3a and TM3b. The latter forms



the top portion of the cytoplasmic domain. The crystal structure of MscS was initially interpreted as the open state of the channel but molecular dynamics simulations later suggested that the pore is too hydrophobic to be fully hydrated and therefore the structure is nonconductive. Notably, the gate is located at the level of the cytoplasmic polar head groups of the lipid bilayer that transmit most of the lateral tension from the bilayer to the channel surface, and tension in the inner leaflet was predicted to drive the opening transition most effectively [45,46]. Both closed and open states in this gating model exhibit splayed peripheral helices uncoupled from the gate, and there was no provision for the inactivated state [47,48]. The alternative model proposed in [49] and supported by functional data interprets the initial non-conductive structure with the uncoupled TM1-TM2 helices as the inactivated state. The physical connection between the peripheral TM1-TM2 helices receiving force from the membrane and the gate-forming TM3s was restored through the cycles of modeling that achieved a tight, almost parallel packing of TM1-TM2 pairs along TM3s [45,50]. The gating cycle was presented as tension-driven alternative transitions into either open state characterized by straightened TM3s or inactivated state with the pore closed by kinked TM3s and TM1-TM2 pairs uncoupled from the gate [49]. Both transitions imply outward motion of the protein-lipid boundary, with the opening producing a larger protein expansion and thus are driven by the membrane tension.

It is also worth investigating the role of channel inactivation in the context of bacterial osmoregulation and osmotic fitness. In a typical patch clamp experiment, upon exposure to moderate tension just above the gating threshold, MscS channels

gradually inactivate. Channels in the inactivated state become non-conductive and insensitive to the membrane tension. Inactivated channels are defined by their lack of response to applied membrane tension whereas channels in the closed state can open if the membrane tension is high enough. One of the most salient features of the MscS gating is its ability to distinguish the rate of tension application. In particular, MscS channels prefer to fully respond to abrupt stimuli while ignoring the slowly applied ones. This smart behavior was previously called the “dashpot” behavior, and may be important in environmental situations where the sense of urgency is critical for microbes [51]. Under non-emergency conditions, transient opening of channels causes dissipation of vital metabolic gradients, which is not desirable. If the osmotic forces do not pose a serious threat to the organism, say, when there is no danger of membrane rupture, instead of jettisoning cellular osmolytes through transient opening, channel inactivation might give enough time to other osmoregulatory systems to kick in [28]. It has been shown that leaky – non-inactivating channels – can be damaging the cells by disrupting vital gradients [52,53]. Therefore, inactivation gives an adaptive edge to bacteria under different dynamic conditions of osmotic fluctuations.

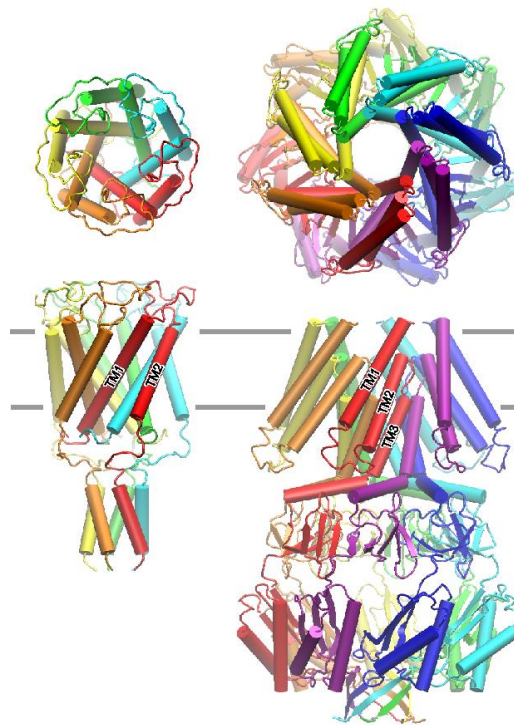


**Figure 1.4. Crystal structures of the mechanosensitive channel proteins MscL and MscS.** **(Left)** *Mycobacterium tuberculosis* MscL crystal structure at 3.5 Å (2OAR.pdb) (Chang et al. 1998). MscL consists of five identical subunits, each 136 amino acids long. There are two transmembrane domains (TM) that sense the tension and form a large pore in the membrane that is ~30 Å in diameter. The C-terminal domains constitute an alpha helical bundle that acts as a molecular pre-filter. The channel gates at tensions approaching the lytic threshold (10-14 mN/m) and is classified as an emergency valve. **(Right)** *Escherichia coli* MscS crystal structure at 3.9 Å (2OAU.pdb) (Bass et al. 2002). MscS is formed by seven identical subunits of 286 amino acids each. Unlike MscL, MscS has three TM domains and requires less tension to gate. C terminal ends of subunits form a large hollow cytoplasmic cage domain. The top and side views are provided for both channels (Courtesy of A. Anishkin).

## Statistical Mechanics of Mechanosensitive Ion Channel Gating

### Equilibrium Picture

Mechanosensitive channels (MS) are the main players in bacterial osmoregulation. They can be visualized as emergency valves that open in the event of osmotic down-shock and rescue cells from bursting by reducing the internal turgor pressure. Any mathematical model describing bacterial survival under extreme osmotic stress has to take into account the delicate interplay between two rates: the rate at which water rushes into the cells building up the internal turgor and the rate at which the excess turgor is reduced as the channels, triggered by membrane tension, open and release osmolytes. In order to introduce mechanosensation into this kinetic game, everything boils down to finding the open probability of channels as a function of tension,  $P_{Open}(\gamma)$ . Once  $P_{Open}(\gamma)$  is known, the total solute efflux can be traced as a function of time. For the simplest case, let us start with a single channel with two states. The channel can be in the closed state with energy,  $E_{Closed}$  or in the open state with energy  $E_{Open}$ . The channel in the open configuration has a larger membrane-displaced area compared to the closed state. This area difference is denoted by  $\Delta A$ . In the absence of tension ( $\gamma=0$ ), the closed state is favored since it has a lower energy than the open state, however, when the external tension increases, the energy contribution due to the external driving force,  $\gamma\Delta A$ , lowers the energy difference between the closed and open state (Fig. 1.5). At high enough tension, the open state eventually becomes energetically more favorable [23,54]. The lateral area change due to channel opening,  $\Delta A$ , is the key ingredient of mechanosensitivity [1,55–57].

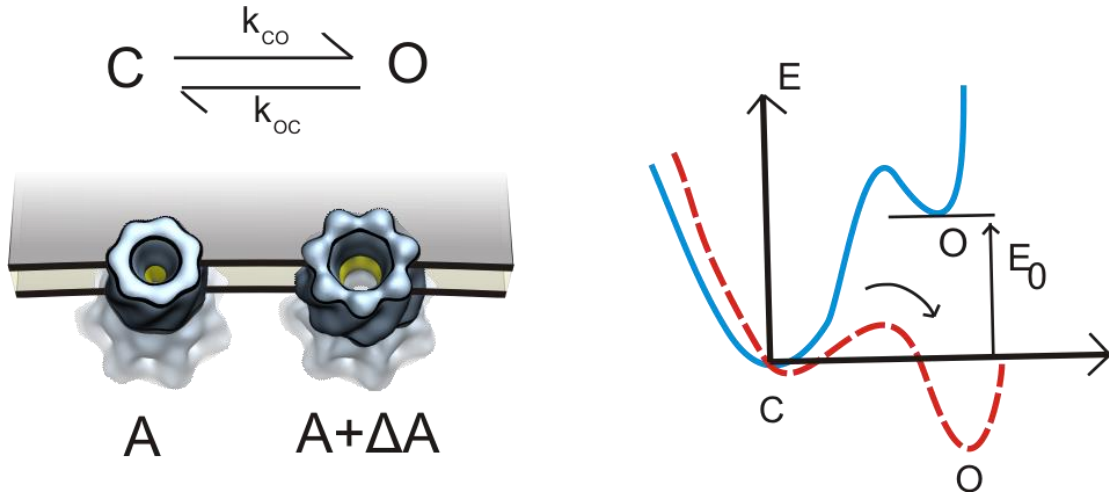


**Figure 1.5 Two-state Boltzmann model for the gating of a mechanosensitive ion channel.** In this approximation, the channel is assumed to have two states: C(closed) and O(open) with energies  $E_{Closed}$  and  $E_{Open}$ . The open state has a larger in-plane expansion area. In the absence of membrane tension, the system resides in the lower energy state. In the presence of tension ( $\gamma$ ), the work done on the system,  $\gamma \Delta A$  lowers the free energy difference between the states and makes the open state energetically more favorable than the closed state. We assume that transition rates for the closed  $\leftrightarrow$  open transition obey detailed balance condition:  $\frac{k_{off}}{k_{on}} = e^{-\beta (E_{Closed} - E_{Open})} e^{-\beta \gamma \Delta A}$ . Thus, once the tension is held fixed the system relaxes to a unique equilibrium distribution where the states are populated according to Boltzmann weight (Sukharev and Corey 2004).

At thermal equilibrium the distribution between the states depends on the external tension and can be described by the Boltzmann distribution. In other words, at thermal equilibrium, the probability of finding a state with a given energy  $E_i$  is:

$$P(E_i) = \frac{e^{-\beta E_i}}{Z} \quad [1.1]$$

where  $Z \equiv \sum_i e^{-\beta E_i}$  is the partition function which ensures that the sum of the probabilities is normalized,  $\sum_i P(E_i) = 1$  and  $\beta$  is defined as the inverse  $k_B T$  where  $k_B$  is the Boltzmann constant and  $T$  is the temperature. Thus, for a two-state system at equilibrium, it is possible to express the probability of finding a channel in the open state as a function of applied tension:

$$P_{Open}(\gamma) = \frac{e^{-\beta(E_{Open}-\gamma\Delta A)}}{e^{-\beta(E_{Open}-\gamma\Delta A)} + e^{-\beta E_{Closed}}} = \frac{1}{1 + e^{\beta(E_0-\gamma\Delta A)}} \quad [1.2]$$

Here,  $E_0 \equiv E_{Open} - E_{Closed}$  is the free energy difference or gating energy in the absence of applied tension. It is important to note that even though the free energy difference between the closed and open state of the channel is represented as a constant, there is an implicit dependency on membrane properties such as thickness and lipid composition [58].

### Markov Chain Models of Ion Channel Gating

Markov chains have been widely used in modeling ion channel gating [59–61]. The symbolic formalization of the rate constants together with a well-developed theory of stochastic processes enable researchers to obtain experimentally falsifiable analytical results. One advantage of using Markov chains over the equilibrium approach is that the probabilities can be traced as a function of time and since the system is coupled to a heat reservoir, in the long-time limit these probabilities converge to their corresponding equilibrium values described by the Boltzmann distributions. In this regard, thermodynamic and kinetic approaches are unified in the long-time limit.

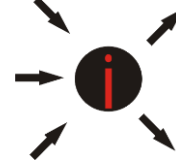
Here, we introduce our mathematical formalism and review some of the main results that will be mainly used in Chapter 3. Let us define  $W_{ij}$  as the probability per unit time to make a transition to state  $i$  from state  $j$  and  $P_i(t)$  as the probability of being in state  $i$  at time  $t$ . We continue with the following assumptions:

- *The system of interest has finitely many states.*
- *The system is memoryless and ergodic (strongly connected).*

- $W_{ij} \neq 0$  whenever  $W_{ji} \neq 0$

Under these conditions, there exists a unique steady state [62] (see below). The rate of change of  $P_i(t)$  can be described by the sum of two contributions: (i) arrows going into  $i$  from  $j$ 's and (ii) arrows going out of  $i$  to some other states  $j$ 's. The net result is the following:

$$\frac{dP_i(t)}{dt} = \sum_{\substack{j \\ j \neq i}} P_j(t)W_{ij} - P_i(t)W_{ji} \quad [1.3]$$



One can define the escape rate as:  $W_{ii} \equiv -\sum_{j \neq i} W_{ji}$ . Therefore [1.3] becomes:

$$\frac{dP_i(t)}{dt} = \sum_j P_j(t)W_{ij} \quad [1.4]$$

Eqn. [1.4] can be also put into matrix form:  $\frac{d\vec{p}}{dt} = W\vec{p} \rightarrow \vec{p}(t) = e^{Wt}\vec{p}(0)$  where  $\vec{p}$  is the probability vector and  $W$  is the transition rate matrix whose off diagonal elements,  $W_{ij}$ , represent the probability per unit time to make a transition from state  $j$  to  $i$  and the diagonal elements are the escape rates from the corresponding states. Now, assuming that there is no degeneracy among eigenvalues of  $W^\dagger$ ,  $W$  is diagonalizable and it can be written as  $W = UDV$ :

$$W = \begin{bmatrix} \vdots & \vdots & \cdots & \vdots \\ u_1 & u_2 & \cdots & u_N \\ \vdots & \vdots & \cdots & \vdots \end{bmatrix} \begin{bmatrix} \lambda_1 & 0 & \cdots & 0 \\ 0 & \lambda_2 & \cdots & 0 \\ \vdots & \vdots & \ddots & \vdots \\ 0 & 0 & 0 & \lambda_N \end{bmatrix} \begin{bmatrix} \cdots & v_1 & \cdots \\ \cdots & v_2 & \cdots \\ \cdots & \cdots & \cdots \\ \cdots & v_N & \cdots \end{bmatrix} \quad [1.5]$$

Here,  $u_i$  and  $v_i$  are the right and the left eigenvectors of  $W$  and are defined as:

$$Wu_i = \lambda_i u_i$$

---

<sup>†</sup>  $W$  can still be diagonalizable, even though the eigenvalues are degenerate. As long as the algebraic multiplicity of the eigenvalue  $\lambda$  - the number of times  $\lambda$  repeated as a root of the characteristic polynomial- is equal to the geometric multiplicity  $\lambda$  - the dimension of  $\lambda$  eigenspace, there will be  $N$  independent eigenvectors and  $W$  is diagonalizable. Regardless of diagonalizability of  $W$ , for a finite and strongly connected system, there is always a unique stationary state.

$$v_i W = \lambda_i v_i \quad [1.6]$$

and  $\lambda_i$  is the corresponding eigenvalue. As  $\vec{p}(t) = e^{Wt}\vec{p}(0)$ , it will prove convenient to define:  $T(t) \equiv e^{Wt}$  and express as  $\vec{p}(t)$  as  $\vec{p}(t) = T(t)\vec{p}(0)$  where:

$$T(t) = e^{Wt} = \sum_{n=0}^{\infty} \frac{(Wt)^n}{n!} = I + Wt + \frac{(Wt)^2}{2} + \dots \quad [1.7]$$

And taking advantage of  $W=UDV$ , we get the following expression for  $T$ :

$$T(t) = \begin{bmatrix} \vdots & \vdots & \dots & \vdots \\ u_1 & u_2 & \dots & u_N \\ \vdots & \vdots & \dots & \vdots \end{bmatrix} \begin{bmatrix} e^{\lambda_1 t} & 0 & \dots & 0 \\ 0 & e^{\lambda_2 t} & \dots & 0 \\ \vdots & \vdots & \ddots & \vdots \\ 0 & 0 & 0 & e^{\lambda_N t} \end{bmatrix} \begin{bmatrix} \dots & v_1 & \dots \\ \dots & v_2 & \dots \\ \dots & \dots & \dots \\ \dots & v_N & \dots \end{bmatrix} \quad [1.8]$$

We note that  $R$  and  $T$  are closely related.  $Ru_i = \lambda_i u_i$  and  $Tu_i = \mu_i u_i$  where  $\mu_i = e^{\lambda_i t}$ .  $T$  is a primitive matrix –there exists a power  $k$  such that  $T_{ij}^k > 0$  for all  $i, j$ .

Therefore the Perron-Frobenius theorem states the following for the primitive matrices:

- $\exists \mu_{PF} \in \mathbb{R}$
- $\mu_{PF} > |\mu_i|$
- $Tu = \mu_{PF}u$  where each elements of  $u$  is positive.
- $\mu_{PF}$  is simple root of  $|T - \lambda I|$ .

Moreover since  $[1 \ 1 \ \dots \ 1] T = [1 \ 1 \ \dots \ 1]$ ,  $\exists \pi$  such that  $T\pi = \pi$  giving us  $\mu_{PF} = 1$ . Since

$T$  is diagonalizable, it has  $N$  independent eigenvectors forming a complete set.

Therefore,  $\vec{p}(0)$  can be expressed as a linear combination of  $u$ 's, namely:

$$\vec{p}(0) = \sum_i^N c_i u_i.$$



$$\begin{aligned}\vec{p}(t) &= T\vec{p}(0) = T \sum_i^N c_i u_i = \sum_i^N c_i \mu_i u_i = \sum_i^N c_i e^{\lambda_i t} u_i \\ &= \pi + \sum_{\mu_i \neq \mu_{PF}}^N c_i e^{\lambda_i t} u_i \quad [1.9]\end{aligned}$$

$$\lim_{t \rightarrow \infty} \vec{p}(t) = \lim_{t \rightarrow \infty} \left( \pi + \sum_{\mu_i \neq \mu_{PF}}^N c_i e^{\lambda_i t} u_i \right) = \pi \quad [1.10]$$

Since  $\mu_{PF} = 1 > |\mu_i|$

$$\lim_{t \rightarrow \infty} \sum_{\mu_i \neq \mu_{PF}}^N c_i e^{\lambda_i t} u_i \rightarrow 0 \quad [1.11]$$

Expressing [1.3] in terms of probability currents also provides some useful insight into the character of the underlying dynamics. Let us define the probability current from state  $j$  to state  $i$  as:  $J_{ij}(t) = P_j(t)W_{ij} - P_i(t)W_{ji}$  and similarly the steady state currents can be written as  $J_{ij}^{SS} = \pi_j W_{ij} - \pi_i W_{ji}$ . Therefore eqn. [1.3] can be written as:

$$\frac{dP_i(t)}{dt} = \sum_{\substack{j \\ j \neq i}} J_{ij}(t) \quad [1.12]$$

At steady state, the sum of all currents in the system is zero:  $\sum_j J_{ij}^{SS} = 0$ . Detailed balance (DB) condition imposes an even stronger relationship on the probability currents at steady state such that every single probability current has to vanish if the system satisfies DB condition:

$$J_{ij}^{SS} = 0 \quad \forall i, j \quad [1.13]$$

$$J_{ij}^{SS} = \pi_j W_{ij} - \pi_i W_{ji} \Rightarrow \frac{W_{ij}}{W_{ji}} = \frac{\pi_i}{\pi_j} \quad [1.14]$$

For a physical system that is in contact with a heat reservoir, detailed balance condition takes the following form:

$$\frac{W_{ij}}{W_{ji}} = \frac{\pi_i}{\pi_j} = \frac{e^{-\beta E_i}}{e^{-\beta E_j}} \quad [1.15]$$

However, when driven by constant thermodynamics forces such as temperature gradients or chemical potential differences, systems might violate the detailed balance condition and maintain non-vanishing currents in the steady state. In order to sustain non-zero currents in the steady state (NESS), the price paid is the entropy production and the depletion of the thermodynamic force, e.g., ATP consumption [63]. In the context of biological motors, currents maintained in the system result in a net movement of the motor in an appropriate direction and provide the directionality [64,65]. For example, a kinesin molecule consumes a single ATP molecule per step to generate mostly unidirectional movement. The overall efficiency of the kinesin motor is around 60%, which roughly corresponds to  $650 k_B T$  energy lost to the environment as dissipation in a second [66]. Detailed balance condition is also closely linked to time's arrow which is –roughly speaking– a measure (or sense) of the distinguishability of past from the future or vice versa [67]. For systems satisfying DB condition, at thermal equilibrium, time's arrow vanishes. Therefore, many molecular motors must dissipate at least  $4-8 k_B T$  of free energy per cycle to achieve the directionality in time [68].

## Non-equilibrium Work Relations

Thermodynamics, in broad terms, deals with the energy transfer from one place to another in various forms such as mechanical, chemical, heat or electrical. The formulation of thermodynamics coincided with the industrial revolution of the late 1700s and early 1800s and thus, thermodynamics, at its heart, was built upon ideas that mainly describe the working principles of steam engines and refrigerators. In 1824, Sadi Carnot published *Reflections on the Motive Power of Fire*, in which he obtained the maximum efficiency of a heat engine, today known as a Carnot engine, and introduced the concept of reversibility. Around 1850, Rudolf Clausius and William Thomson formulated the first and second laws of thermodynamics. These developments in thermodynamics also laid the groundwork for the birth of statistical mechanics. Boltzmann, Maxwell, Gibbs and others established the connection between the macroscopic properties of matter in bulk and its constitutive elements—atoms and molecules. In this regard, classical statistical mechanics uses probability theory to describe the average behavior of macroscopic systems.

Among all branches of physics, thermodynamics holds a privileged position as emphasized by Albert Einstein (M.J. Klein, Thermodynamics in Einstein's Universe, in Science, 157 (1967), p. 509):

*“[A law] is more impressive the greater the simplicity of its premises, the more different are the kinds of things it relates, and the more extended its range of applicability. Therefore, the deep impression which classical thermodynamics made on me. It is the only physical theory of universal content which I am convinced, that within the framework of applicability of its basic concepts will never be overthrown.”*

And by Sir Arthur Stanley Eddington (The Nature of the Physical World (1930), p. 74):

*“The law that entropy always increases – the Second Law of Thermodynamics – holds I think, the supreme position among the laws of Nature. If someone points out to you that your pet theory of the Universe is in disagreement with Maxwell’s equations – then so much worse for Maxwell equations. If it is found to be contradicted by observation -- well experimentalists do bungle things sometimes. But if your theory is found to be against the second law of Thermodynamics, I can give you no hope; there is nothing for it but to collapse in deepest humiliation.”*

The fame and success of thermodynamics result from the law of large numbers, which simply states that deviations from average behavior are fantastically small for macroscopic systems. To be more specific, let us consider a gas of  $N \sim 10^{23}$  molecules confined in a cylinder and in thermal equilibrium with its surroundings. For this system, the relative fluctuations are order of  $10^{-11}$ . Therefore, for macroscopic systems ( $N \sim 10^{23}$ ), statistical fluctuations around the averages are negligible [66,69]. However, for small systems where fluctuations are order of  $\sim 1$ , large deviations from averages become more visible. It turns out that these fluctuations are not random background noise due to poor statistics ( $N \sim 1$ ), but rather they satisfy strong, yet unexpected relations [70,71]. Moreover, once these fluctuations are treated properly, thermodynamic inequalities can be replaced by equalities [71]. In what follows, we first provide a brief review of thermodynamic processes and then derive the non-equilibrium work relations that establish an exact relation between work and free energy.

## The Clausius Inequality and Macroscopic Thermodynamics

Consider a finite, classical system in contact with a thermal reservoir at temperature  $T$ . The system might be a rubber band, and the surrounding air in this case serves as a thermal reservoir. Let us introduce an externally controlled degree of freedom,  $\lambda$ . We also refer to  $\lambda$  as our work parameter since by changing  $\lambda$ , we can do work on the system [72,73] (Fig. 1.6).

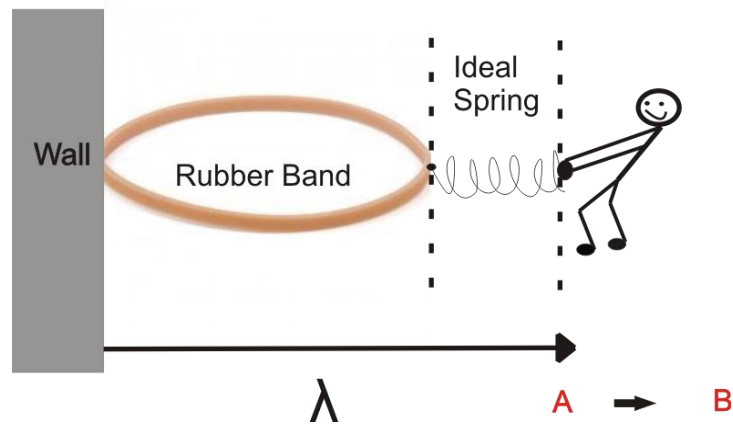


**Figure 1.6. Stretching a rubber band** (Not to scale!)

Let us now imagine the following thermodynamic process: initially the rubber band is in thermal equilibrium with the surrounding air and  $\lambda = A$ . Next, we rapidly vary our work parameter,  $\lambda$ , from  $A$  to a new value  $B$  (which results in stretching the rubber band). We fix the  $\lambda$  at  $B$  and let the system reach a new equilibrium with the surroundings. The first law of thermodynamics states that the energy is conserved, and therefore the work done on the system ( $W$ ) plus the heat received from the environment ( $Q$ ) is equal to the change in the internal energy of the system ( $\Delta U$ ):

$$W = \Delta U - Q \quad [1.15]$$

The Clausius inequality establishes a boundary between the amount of heat absorbed from the surroundings at temperature  $T$  and the change in the entropy of the system according to:

$$\int_A^B \frac{\delta Q}{T} \leq S_B - S_A = \Delta S \quad [1.16]$$

Here, the thermodynamic process starts with the equilibrium state  $A$  and ends in a new equilibrium state  $B$ .  $\delta Q$  is the heat received from the environment during the process. The equality holds if the process is reversibly carried out. Plugging the Clausius inequality into eqn. [1.15], we obtain the following:

$$W = \Delta U - T \int_A^B \frac{\delta Q}{T}$$

$$W \geq \Delta U - T\Delta S = \Delta F \quad [1.17]$$

Note that  $F$  is the Helmholtz free energy of the system,  $F=U-TS$ . The equality, again, holds only if the process is carried out slowly enough such that the system isothermally evolves through subsequent equilibrium states from  $A$  to  $B$ . In this case, the work done under reversible conditions equals the free energy difference,  $W_{rev} = \Delta F$ .

Let us consider a cyclic process where the work parameter  $\lambda$  takes the same value at the beginning and at the end,  $\lambda: A \rightarrow B \rightarrow A$ . It will prove convenient to split the cyclic process into a *forward* and a *reverse* process. During the forward process,  $\lambda$  is varied from  $A$  to  $B$  using the protocol  $\lambda_F(t)$  and during the reverse process  $\lambda$  is varied from  $B$  to  $A$  under a time-reversed protocol,  $\lambda_R(t)$ , where  $\lambda_R(t) = \lambda_F(\tau - t)$ . Here  $\tau$  is the duration of either process. The protocol is pre-defined but otherwise

arbitrary. Since free energy is a state function, for cyclic processes  $\Delta F = 0$ , hence eqn. [1.17] states that:

$$W_{cyclic} \geq 0 \quad [1.18]$$

Moreover, eqn. [1.17], when applied to both forward and the reverse processes separately, yields:

$$\begin{aligned} W_F &\geq \Delta F = F_B - F_A \\ W_R &\geq -\Delta F = F_A - F_B \end{aligned} \quad [1.19]$$

or equivalently

$$W_F + W_R \geq 0 \quad [1.20]$$

Eqn. [1.20] is also known as Kelvin-Planck statement of the second law of thermodynamics. Kelvin-Planck statement simply implies that there is “no free lunch” in nature [71].

Let us briefly discuss how thermodynamics at nano-scale differs from macroscopic thermodynamics discussed above. The mechanosensitive ion channel of small conductance, MscS, constitutes a good example of a microscopic system for which thermal fluctuations are non-negligible. We should also emphasize that MscS does not bear perfect analogy to the rubber band –indeed, the microscopic analogue of stretching a rubber band would be stretching a strand of RNA using optical tweezers [72–74] yet the MscS example will suffice to illustrate how the laws of thermodynamics apply to microscopic systems.

MscS is naturally embedded in *E. coli*'s membrane. In a typical patch clamp experiment, the micropipette with the clamped membrane is immersed into the bath solution at room temperature, which serves as a thermal reservoir. The “work

parameter” is the membrane tension,  $\gamma$  and the conjugate variable to the work parameter is the lateral protein area expansion,  $\Delta A$  (Fig. 1.2). The application of suction changes the pressure between the two sides of the membrane and hence varies its tension, which allows us to perform work on the system and lower the free energy difference between the open and the closed states. Now, let us imagine the following cyclic process: initially we start with  $\gamma=A$  and the channel resides in the closed state, then we increase the membrane tension to a new value  $\gamma=B$ , which is high enough to open the channel, and let the system thermalize again. Therefore, the second half of the process also starts in thermal equilibrium. We then decrease the tension back to  $\gamma=A$  using the time-reversed protocol.

- Forward process:  $\gamma: A \rightarrow B$
- Reverse process:  $\gamma: B \rightarrow A$

Let  $W_F$  and  $W_R$  denote the work performed as the channel gates, Closed $\rightarrow$ Open and closes, Open $\rightarrow$ Closed, respectively. An important remark is now in place. Even if we repeat the same experimental protocol many times,  $W_F$  and  $W_R$  will take on different values in different realizations; namely, they will fluctuate from one realization to another due to the randomness of the micro-world where everything is constantly jiggling. On some rare occasions, this randomness might act “constructively” on the channel, and the channel might gate at lower work values than the free energy difference,  $W < \Delta F$ , violating the second law of thermodynamics transiently. Such rare events are “impossible” to observe for macroscopic systems. In this regard, the second law of thermodynamics can be interpreted statistically when applied to



smaller systems. At the nano-scale, thermal fluctuations give rise to work distributions and the inequalities such as eqns. [1.16] and [1.17] hold on average:

$$\langle W \rangle \geq \Delta F \quad [1.20]$$

$$\langle W \rangle_{cyclic} = \langle W_F \rangle + \langle W_R \rangle \geq 0 \quad [1.21]$$

Cyclic Process

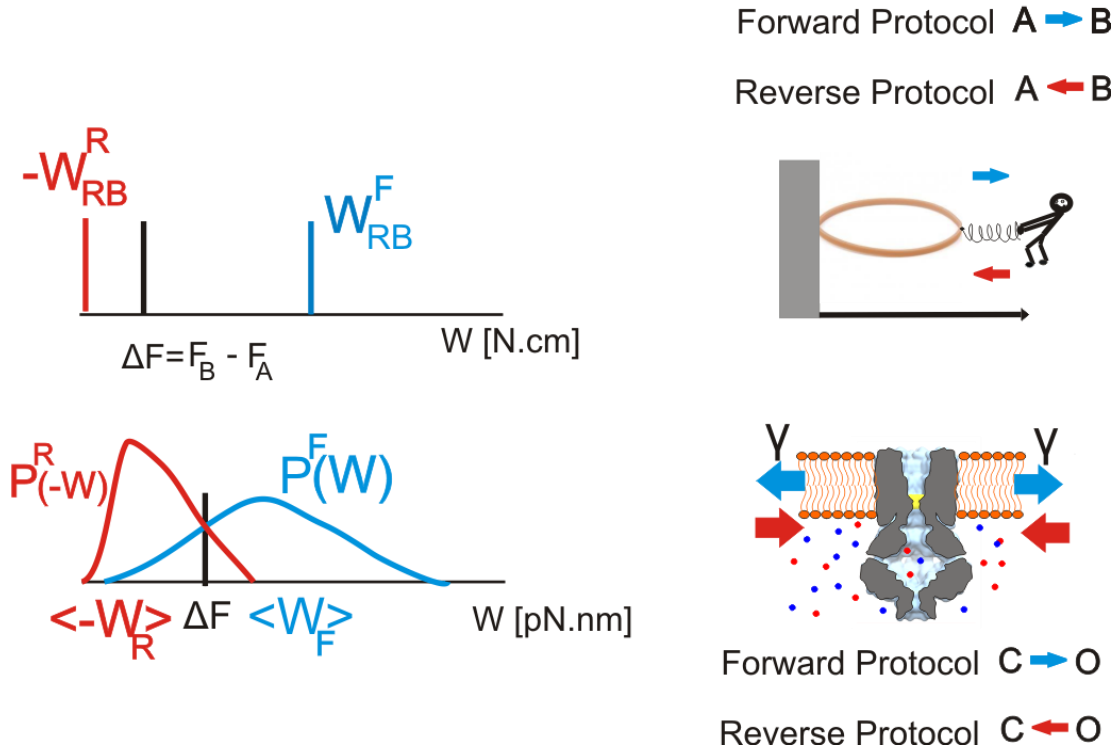


**Figure 1.7. Macroscopic system vs microscopic system.** When applied to small systems the second law of thermodynamics is subject to statistical interpretation. The cyclic process defined in the text consists of a forward and a reverse protocol. The work values obtained during the application of the forward and reverse protocols are denoted by superscripts F and R, respectively. For macroscopic systems such as the rubber band, thermal fluctuations are negligible and the second law of thermodynamics imposes strict inequalities on the work performed during either process and the change in the corresponding free energy of the system:  $W_F \geq \Delta F = F_B - F_A$  and  $W_R \geq -\Delta F = F_A - F_B$  or  $W_{cyclic} = W_F + W_R \geq 0$ . On the other hand, for small systems, e.g. MscS, thermal fluctuations matter and the inevitable randomness in the micro-world gives rise to work distributions. The inequalities now hold on average:  $\langle W_F \rangle \geq \Delta F$  and  $\langle W_R \rangle \geq -\Delta F$  or  $\langle W_{cyclic} \rangle \geq 0$ . Therefore, on some rare occasions, it is possible to observe the violation of the second law of thermodynamics. For example, the channel might harvest some energy from the randomness in the bath solution and might gate at lower work values than the free energy difference,  $W < \Delta F$ , violating the second law of thermodynamics transiently. Note that the work distributions of the forward and reverse protocols cross at  $\Delta F$  according to eqn [1.23].

In summation, for small systems, fluctuations matter and the second law thermodynamics becomes a statistical statement about averages. These fluctuations are not just random noise due to the nanoscopic size of the system or poor statistics, but rather they satisfy strong symmetry relations. Above all, once the fluctuations are taken into account, it is possible to obtain equilibrium information from the microscopic response of a system driven arbitrarily far from equilibrium. The last statement will be addressed in the next section.

Non-equilibrium work relations:

Even though the foundations of non-equilibrium statistical mechanics were laid almost a century ago, the field has been experiencing a renaissance recently. Fluctuation theorems in general can be expressed in different forms [75–87]. Here, we narrow our attention to non-equilibrium work fluctuations. One of the main themes of this section is that inequalities can be rewritten as equalities once the fluctuations are properly incorporated into the picture.

1. Jarzynski Equality [85]:

$$\langle e^{-\beta W} \rangle_{A \rightarrow B} = e^{-\beta \Delta F} \quad [1.22]$$

Here the angular brackets represent the ensemble average taken over many realizations of the same switching protocol ( $\lambda: A \rightarrow B$ ) starting from an equilibrium state ( $\lambda = A$ ) in contact with a heat reservoir at temperature  $T$ .  $\beta$  is always defined as inverse  $k_B T$  where  $k_B$  is the Boltzmann constant.

2. Crooks Fluctuation Theorem [86]:

$$\frac{P_{A \rightarrow B}(W)}{P_{B \rightarrow A}(-W)} = e^{\beta(W - \Delta F)} \quad [1.23]$$

The work distributions,  $P_{A \rightarrow B}(W)$  and  $P_{B \rightarrow A}(-W)$ , are associated with the thermodynamic process of switching the system from A to B and with the corresponding time-reversed protocol of switching the system from B to A (where the system starts in the corresponding equilibrium state, A or B) (Fig. 1.7)

### Hamiltonian Derivation

Here we use Hamilton's equations to describe the microscopic evolution of the system and derive eqn. [1.22]. Let  $\mathbf{x}$  be a vector carrying the information about the canonical coordinates of the system  $\mathbf{x}=\mathbf{x}(\mathbf{q}, \mathbf{p})$ . Here,  $\mathbf{x}$  is a point in the phase space of the system of interest and does not include the degrees of freedom of the thermal reservoir<sup>‡</sup>. The system is first prepared in equilibrium, at  $\lambda =A$ , then the heat bath is removed as the work parameter is varied from  $\lambda_0 = A$  to  $\lambda_\tau = B$ . Therefore, during the application of the protocol the system is isolated and the microscopic evolution can be described by the deterministic Hamiltonian dynamics.

$$\dot{q} = \frac{\partial H}{\partial p}, \dot{p} = -\frac{\partial H}{\partial q} \quad [1.24].$$

We assume that the system's Hamiltonian is a function of the microstate of the system and the work parameter,  $\lambda$ :  $H = H(\mathbf{x}, \lambda)$ . At the end of the protocol, the work parameter is held fixed at  $\lambda=B$  and the heat bath is brought back to let the system thermalize again. Since the system is isolated ( $Q=0$ ) during the switching process, the work done on the system is equal to the change in the energy of the system:

$$W(x_0) = H(x_\tau(x_0), B) - H(x_0, A) \quad [1.25].$$

---

<sup>‡</sup> It is also possible to treat the system of interest and the thermal reservoir as one big isolated system and carry out similar calculations in the combined phase space of system of interest and thermal reservoir [88].

Here  $x_\tau(x_0)$  is the terminal station of the phase space trajectory launched at  $x_0$ . Since the Hamiltonian dynamics is deterministic,  $x_\tau$  is uniquely determined by  $x_0$ .

However, we note that  $x_0$  is sampled from the Boltzmann Distribution,  $P(x_0) = e^{-\beta H(x_0,A)} / Z_A$  giving rise to stochasticity in the dynamics. Therefore, the average is taken over the initial distribution of the phase space points:

$$\begin{aligned} \langle e^{-\beta W} \rangle &= \int dx_0 P^{eq}(x_0, A) e^{-\beta W(x_0)} \\ &= \frac{1}{Z_A} \int dx_0 e^{-\beta H(x_\tau(x_0), B)} \\ &= \frac{1}{Z_A} \int dx_\tau \left| \frac{\partial x_\tau}{\partial x_0} \right|^{-1} e^{-\beta H(x_\tau(x_0), B)} = \frac{1}{Z_A} \int dx_\tau e^{-\beta H(x_\tau, B)} \end{aligned}$$

In the last line, the variable of integration was changed from  $x_0$  to  $x_\tau$  which is a valid operation since  $x_0$  uniquely determines  $x_\tau$  and Liouville 's theorem states that

$\left| \frac{\partial x_\tau}{\partial x_0} \right|^{-1}$  is 1 [73,85]. Thus, we finally arrive at:

$$\langle e^{-\beta W} \rangle = \frac{Z_B}{Z_A} = e^{-\beta \Delta F}$$

It is instructive to recover the second law of thermodynamics in the form of eqn.

[1.17] from eqn. [1.22] by making use of Jensen's inequality  $\langle e^x \rangle \geq e^{\langle x \rangle}$ , we get

$$\langle W \rangle \geq \Delta F.$$

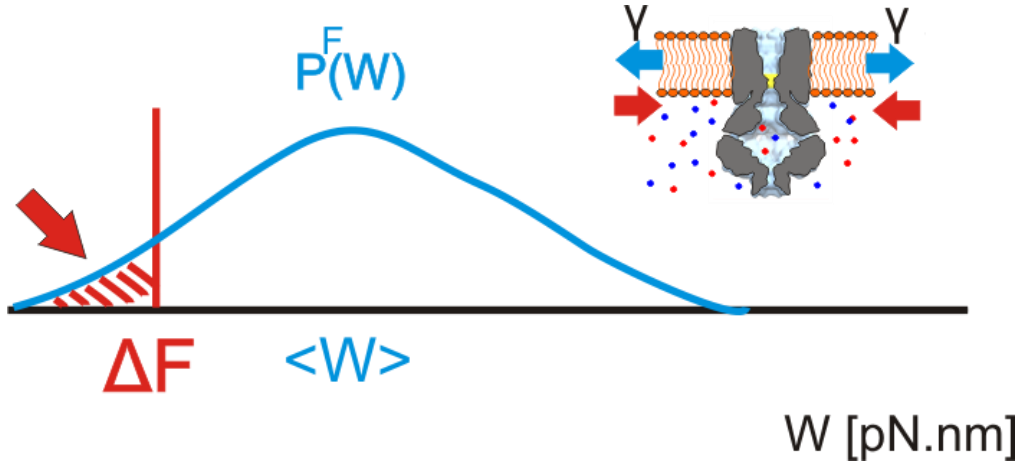


**Figure 1.8. The distribution of work values obtained from a thermodynamic process applied to a small system, e.g., MscS.** The second law of thermodynamics holds on average:  $\langle W \rangle \geq \Delta F$ . The work values that fall below  $\Delta F$  violate the second law (red region). However, the left tail of the distribution—indicated by the red arrow—is exponentially suppressed meaning that observing a work value that is far less than  $\Delta F$  is almost impossible, which is in agreement with our daily life experience.

Moreover, for a given thermodynamic process, we can estimate the probability of observing a work value that violates the second law of thermodynamics that is  $W < \Delta F$ . Let  $P^F(W)$  be the probability distribution of work values for a thermodynamic process, say, the gating of MscS. Then the work values for which  $W < \Delta F$  correspond to the left-hand tail of the distribution indicated by the red arrow (Fig.1.8). In particular, we can calculate the probability of observing a work value that is smaller than  $\Delta F$  by an amount of  $\xi$  where  $\xi$  is an arbitrary positive number with units of energy [71]:

$$\begin{aligned}
 P(W \leq \Delta F - \xi) &= \int_{-\infty}^{\Delta F - \xi} dW P^F(W) \\
 &\leq \int_{-\infty}^{\Delta F - \xi} dW P^F(W) e^{\beta(\Delta F - \xi - W)} \\
 &\leq e^{\beta(\Delta F - \xi)} \int_{-\infty}^{\infty} dW P^F(W) e^{-\beta W} \\
 &\leq e^{-\beta \xi} \quad [1.26]
 \end{aligned}$$

Eqn. [1.26] states that the probability to observe a work value that is smaller than  $\Delta F$  decays exponentially or faster [71,73]. In other words, it is possible to “tunnel” into the thermodynamically forbidden regions for microscopic systems where  $\xi \sim k_B T$ . However, observing large violations where  $\xi \gg k_B T$  is almost impossible [71]. Therefore, we never observe macroscopic violations of the second law in our daily lives. As Feng and Crooks stated [68]:

*“In our everyday lives we have the sense that time flows inexorably from the past into the future; water flows downhill; mountains erode; we are born, grow old, and die; we anticipate the future but remember the past.”*

We conclude this section by reiterating that in the derivation of eqn. [1.22], the assumption is that the system is isolated from the heat reservoir as the work parameter is switched from A to B. A generalized approach, which also includes the degrees of freedom of the system and the heat reservoir, can be found in [88]. Non-equilibrium work relations are robust regardless of how the microscopic dynamic is modeled. Below, we derive non-equilibrium work relations for discrete time Markov dynamics.

### Markov Jump Process

Let us now derive eqns. [1.22] and [1.23] using discrete-time Markov dynamics. We assume that the system is in contact with the heat bath during the application of a pre-defined but otherwise arbitrary protocol,  $\lambda(t)$ . The heat bath is the source of randomness in the system’s dynamics. Following Crooks, we describe the microscopic history of the system as a sequence of points visited in the phase space,  $v = \{x_0, x_1, x_2, \dots, x_{\tau-1}, x_\tau\}$  at times  $\{t_0, t_1, t_2, \dots, t_{\tau-1}, t_\tau\}$  as the work parameter is varied from  $\lambda_0 = A \rightarrow \lambda_1 \rightarrow \dots \rightarrow \lambda_{\tau-1} \rightarrow \lambda_\tau = B$  (Fig 1.9).

The step size is  $t_{i+1} - t_i = \Delta t$ , and therefore  $t_i = i\Delta t$ . We assume that the system is memoryless (Markovian) meaning that probability of making a transition from state  $x_i$  to  $x_j$  at time  $t_i$  depends only on the current state  $x_i$  but not the other phase space points visited before  $x_i$ .

$$P(x_{i+1}|x_0 \rightarrow x_1 \rightarrow \dots \rightarrow x_{i-1} \rightarrow x_i) = P(x_{i+1}|x_i) \quad [1.27]$$

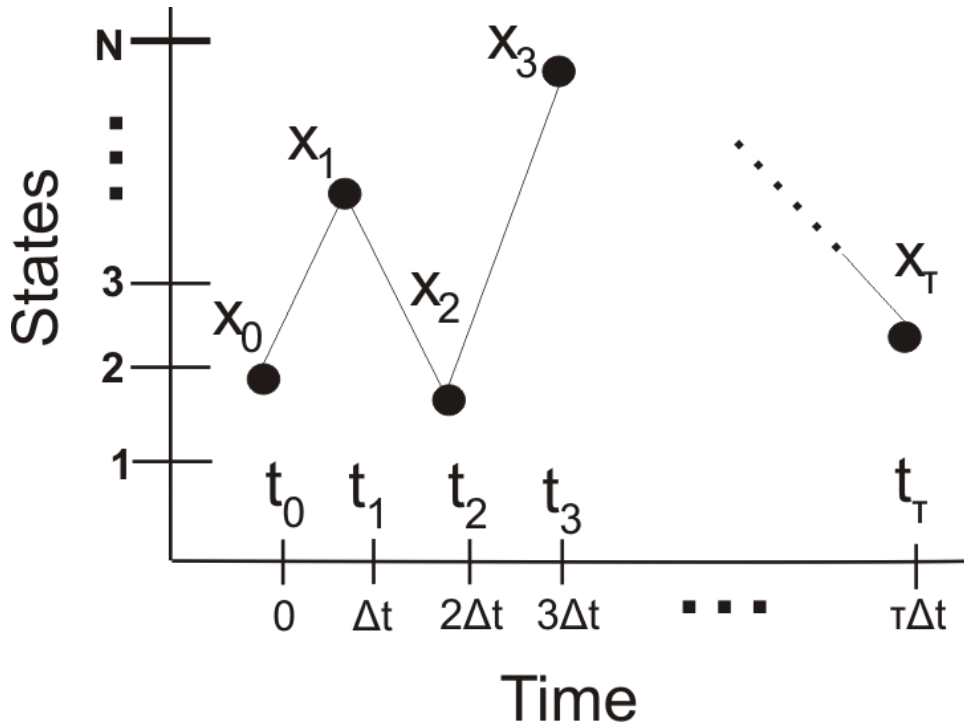


**Figure 1.9.** A single realization of the protocol and the corresponding trajectory in the phase space for a Markov jump process.

The transition probability to the next state can also be manipulated by the work parameter and is therefore a function of  $\lambda$ . For example, in the context of mechanosensitive ion channels, the transition to the open state at higher tensions

becomes more likely (Fig 1.5). Finally, we assume that each single step transition is microscopically reversible and obeys the detailed balance condition [67,89]:

$$\frac{P(x \rightarrow x'; \lambda)}{P(x \leftarrow x'; \lambda)} = \frac{e^{-\beta H(x', \lambda)}}{e^{-\beta H(x, \lambda)}} \quad [1.28]$$

Here  $P(x \rightarrow x'; \lambda)$  implies dependence on the work parameter.

Detailed balance condition guarantees that once  $\lambda$  is held fixed, the system relaxes to an equilibrium state described by the Boltzmann Distribution [69]. Now, imagine the following multi step processes where the system makes jumps in the phase space as the work parameter is varied in discrete steps from A to B during the forward process and B to A during the reverse process. A microscopic trajectory (Fig.1.9.) during the forward process is represented by:

$$v^F = \{\lambda_0^F = A \ x_0 \xrightarrow{\lambda_1^F} x_1 \xrightarrow{\lambda_2^F} x_2 \dots \xrightarrow{\lambda_{\tau-1}^F} x_{\tau-1} \xrightarrow{\lambda_\tau^F} x_\tau \ \lambda_\tau^F = B\}$$

Crooks defined the total heat exchange with the heat bath,  $Q$  and the work performed on the system,  $W$  as [90]:

$$Q = \sum_{k=1}^{\tau} H(x_k, \lambda_k) - H(x_{k-1}, \lambda_k) \quad [1.29]$$

$$W = \sum_{k=1}^{\tau} H(x_{k-1}, \lambda_k) - H(x_{k-1}, \lambda_{k-1}) \quad [1.30]$$

And the first law of thermodynamics takes the following form in this model:

$$Q + W = H(x_\tau, \lambda_\tau = B) - H(x_0, \lambda_0 = A) \quad [1.31]$$

We can now relate the probability of observing a certain trajectory in the phase space,  $P(v^F)$  to its time reversal given that the protocol  $\lambda(t)$  is employed.



$$\frac{P(v^F)}{P(v^R)} = \frac{P(\lambda_0^F = A \ x_0 \xrightarrow{\lambda_1^F} x_1 \xrightarrow{\lambda_2^F} x_2 \dots \xrightarrow{\lambda_{\tau-1}^F} x_{\tau-1} \xrightarrow{\lambda_\tau^F} x_\tau \ \lambda_\tau^F = B)}{P(\lambda_\tau^R = A \ x_0 \xleftarrow{\lambda_{\tau-1}^R} x_1 \xleftarrow{\lambda_{\tau-2}^R} x_2 \dots \xleftarrow{\lambda_1^R} x_{\tau-1} \xleftarrow{\lambda_0^R} x_\tau \ \lambda_0^R = B)} \quad [1.32]$$

Using the Markov property (eqn. [1.27]) and noting that  $\lambda_R(t) = \lambda_F(\tau - t)$ , eqn [1.32] can be rewritten as

$$\frac{P(v^F)}{P(v^R)} = \frac{P^{eq}(x_0, A) P(x_0 \xrightarrow{\lambda_1^F} x_1) \dots P(x_{\tau-1} \xrightarrow{\lambda_\tau^F} x_\tau)}{P^{eq}(x_\tau, B) P(x_0 \xleftarrow{\lambda_1^R} x_1) \dots P(x_{\tau-1} \xleftarrow{\lambda_\tau^R} x_\tau)} \quad [1.33]$$

Combining detailed balance condition (eqn. [1.28]) with the heat definition above (eqn. [1.29]), we arrive at:

$$\frac{P(v^F)}{P(v^R)} = \frac{P^{eq}(x_0, A)}{P^{eq}(x_\tau, B)} e^{-\beta Q^F} \quad [1.34]$$

Where  $Q^F$  is the heat –the amount of energy transferred to the system from the heat bath. We note that  $Q^F$  is a functional of phase space trajectories,  $Q^F(v^F)$ , and it is odd under time reversal,  $Q^F = -Q^R$ . If both forward and reverse processes start at equilibrium, then  $P^{eq}(x_0, A)$  and  $P^{eq}(x_\tau, B)$  follow the Boltzmann Distribution and eqn [1.34] can be written as [71,86]:

$$\frac{P(v^F)}{P(v^R)} = e^{\beta(W^F - \Delta F)} = e^{\beta W_{Diss}^F} \quad [1.35]$$

where  $W^F$  is the work done on the system during the forward process and  $W_{Diss}^F$  is the amount of work that is dissipated during the forward process. Similar to heat, both  $W^F$  and  $W_{Diss}^F$  are functional of the phase space trajectories and are also odd under time reversal,  $W^F = -W^R$ ,  $W_{Diss}^F = -W_{Diss}^R$ .

Let us now calculate  $\langle e^{-\beta W} \rangle_F$  where subscript F denotes the ensemble of average taken over the forward trajectories.

$$\begin{aligned} \langle e^{-\beta W} \rangle_F &= \sum_{v^F} e^{-\beta W} P(v^F) = \sum_{v^R} e^{-\beta W} P(v^R) e^{\beta(W-\Delta F)} \\ &= e^{-\beta \Delta F} \sum_{v^R} P(v^R) = e^{-\beta \Delta F} \end{aligned}$$

We recover eqn. [1.22] using discrete-time Markov dynamics where in the last line we used the fact that the probability distributions are normalized and  $\sum_{v^F} \dots =$

$$\sum_{v^R} \dots = \sum_{x_0, x_1 \dots x_\tau} \dots$$

The work distributions for the forward and reverse process can be obtained as follows:

$$\begin{aligned} P^F(W) &= \langle \delta(W - W(v^F)) \rangle = \sum_{v^F} \delta(W - W(v^F)) P(v^F) \\ &= e^{\beta(W-\Delta F)} \sum_{v^R} \delta(W + W(v^R)) P(v^R) = e^{\beta(W-\Delta F)} \langle \delta(W + W(v^R)) \rangle \\ &= e^{\beta(W-\Delta F)} P^R(-W). \end{aligned}$$

We obtain Crooks Fluctuation Theorem (eqn. [1.23]). We are now in a position to derive a more general result. Following Crooks [87], let F be an arbitrary function of the phase space trajectories,  $F=F(v)$ . Using eqn. [1.35], the path ensemble average of F can be written as:

$$\begin{aligned} \langle F \rangle_F &= \sum_{v^F} F P(v^F) = \sum_{v^F} F e^{\beta W_{Diss}^F} P^R(v^R) \\ &= \sum_{v^R} \tilde{F} e^{-\beta W_{Diss}^R} P^R(v^R) = \langle \tilde{F} e^{-\beta W_{Diss}^R} \rangle_R \quad [1.36] \end{aligned}$$

where  $\tilde{F}$  is time reversal of F. It would be more convenient for us to replace F with  $F e^{-\beta W_{Diss}^F}$ , which yields [87]:

$$\langle F e^{-\beta W_{Diss}^F} \rangle_F = \langle \tilde{F} \rangle_R \quad [1.37]$$

The importance of eqn. [1.37] cannot be overstated. Many other fundamental relations in non-equilibrium thermodynamics can be derived from it [87]. For example:

- For  $F=1$ , we recover the Jarzynski Equality:

$$\langle e^{-\beta W_{Diss}^F} \rangle_F = 1$$

$$\langle e^{-\beta W + \beta \Delta F} \rangle_F = 1 \Rightarrow \langle e^{-\beta W} \rangle_F = e^{-\beta \Delta F}$$

- For  $F = \delta(W - W(v^F))$ , we recover the Crooks fluctuation theorem:

$$\langle \delta(W - W(v^F)) e^{-\beta W_{Diss}^F} \rangle_F = \langle \delta(W + W(v^R)) \rangle_R$$

$$e^{\beta \Delta F} \langle \delta(W - W(v^F)) e^{-\beta W(v^F)} \rangle_F = \langle \delta(W + W(v^R)) \rangle_R$$

$$e^{\beta \Delta F} e^{-\beta W} P^F(W) = P^R(-W)$$

$$\frac{P^F(W)}{P^R(-W)} = e^{+\beta(W - \Delta F)}$$

- If we choose  $F = f(x_\tau^F)$ , then  $\tilde{F} = f(x_0^R)$ , we have the following:

$$\langle f(x_\tau^F) e^{-\beta W_{Diss}^F} \rangle_F = \langle f(x_0^R) \rangle_R \quad [1.38]$$

*Since each process starts at equilibrium, the right hand side is simply the average over the initial equilibrium ensemble of the system, whereas the left hand side is the average over a non-equilibrium ensemble. The key to equate the two ensembles involves a weighting procedure via  $e^{-\beta W_{Diss}^F}$  as shown above.*

We end this section by adding that the choice of  $F = \delta(W_{Diss}^F - W_{Diss}^F(v^F))$  recovers

the entropy production fluctuation theorem while  $F = f(x_\tau^F) e^{\beta W_{Diss}^F}$  gives the

Kawasaki nonlinear response relation. The details can be found in [87].

## Problem Statements and Questions

Tension-activated channels in the mechanism of osmotic fitness in *Pseudomonas aeruginosa*

Summarizing the background information in the introduction, we may state that the low-threshold MscS and high-threshold MscL are the two major channels providing fast osmotic permeability response that saves bacteria from drastic osmotic downshifts. These two channel species have been extensively studied in terms of their structure and gating mechanisms. Yet, despite the progress in biophysical studies of these individual mechanosensitive channels (more than 500 papers published on MscS and MscL to date), little is known about the actual release process that takes place in the cell upon abrupt osmotic downshift. There are almost no data on the extent and rate of swelling, the kinetics of osmolyte release, the molecules that escape through specific channels, when and how the transient permeability ceases, and finally, how all these parameters are linked to osmotic fitness. Also, most of the previous studies have been limited to *E. coli*, and the composition of the osmo-protective system and its mode of action have not been functionally characterized in other medically-relevant microorganisms, such as *P. aeruginosa*. This prompts us to take a combined approach and use fast mixing light scattering (stopped-flow) measurements together with patch-clamp and molecular cloning techniques to compare the osmolyte release systems in *Pseudomonas aeruginosa* and *E. coli*. The data presented in Chapter 2 support the hypothesis that under strong hypotonic conditions the release system can prevent lytic tension in the membrane only through dissipation of the osmotic gradient that is faster than the process of generation of

internal hydrostatic pressure. To frame this hypothesis in the form of a quantitative kinetic/mechanical model, we needed to specify the parameters required for a realistic quantitative model of bacterial osmotic survival and work toward their experimental evaluation. Therefore, we aim to answer the following questions:

- The kinetics of cell swelling is defined by the osmotic gradient and water permeability of the cell envelope; the latter parameter is not known for most bacteria. What are the osmotic water permeabilities of *E. coli* and *P. aeruginosa* membranes?
- There are practically no data about real-time kinetics of osmolyte exchange between the bacterial cytoplasm and the external media under any osmotic shock conditions. What is the time course of osmolyte release under non-lytic and lytic shock conditions for both microbes?
- The osmotic survival experiment revealed that *P. aeruginosa* survives larger osmotic shocks than *E. coli*. What explains *P. aeruginosa*'s relative ruggedness? What is the role of mechanosensitive ion channels in the mechanism of osmotic fitness of *P. aeruginosa*?

Spatiotemporal relationships defining the adaptive gating of mechanosensitive ion channel MscS

Although the release system in *E. coli* is comprised of MscL, MscS and five other MscS-related channel species [35,91,92], the low-threshold MscS and the high-threshold MscL were shown to mediate the bulk of osmolyte exchange and either one is sufficient to rescue the majority of bacterial population from osmotic lysis [35].

Despite the earlier assumption that MscS and MscL perform essentially the same function [93–95], there are more data that each of the channels has evolved to perform its own specific role. In particular, MscL does not ever inactivate [46]. MscS, in contrast, displays a significant amount of inactivation under moderate tension wherein it enters a non-conductive state that is unable to open by tension [49,51]. In Chapter 3, we answered the following questions:

- Tension-dependent inactivation of low-threshold MscS channels is common for the three gram-negative bacterial species studied by patch-clamp: *E. coli* [46,51], *V. cholerae* [96], and *P. aeruginosa* [29]. What is the role of inactivation in the osmotic permeability response of microbes?
- The existence of a non-conductive, tension-insensitive (inactivated) state and the location of the inactivated state well on the energy landscape relative to other states are not coincidental. It rather suggests a delicate interplay between physics and evolution. What is the physics of inactivation?
- Can we model the rich gating dynamics of MscS and obtain further analytical predictions from the model? Can we obtain closed-form expressions for the parameters that are experimentally hard to determine?
- Is it possible to relate the obtained protein area expansion parameters to the structural aspect of MscS gating?

## Recovery of equilibrium free energy from non-equilibrium thermodynamics with mechanosensitive ion channels in E.coli

The free energy difference ( $\Delta F$ ) is an indispensable part of the biophysical and structural characterization of ion channels. However, in vitro electrophysiological measurements of the free energy difference between the open and closed states of ion channels are challenging due to hysteresis effects and inactivation. The most common way to obtain  $\Delta F$  is to fit the open probability of the channel to a two-state Boltzmann distribution function and extract the relevant parameters such as  $\Delta F$  assuming that the Boltzmann distribution properly describes the open probability of the channel. However, for systems out of equilibrium, the Boltzmann distribution may not hold. Indeed, if the protocol is delivered in a time symmetric manner such that the membrane tension is increased and decreased with the same rate as in a triangular ramp protocol, the system displays a clear hysteresis loop – the fingerprint of non-equilibrium processes. Therefore, the choice of an equilibrium-based formalism to extract the free energy difference for a non-equilibrium process may contribute to the variability in  $\Delta F$  in the literature, ranging from  $5 k_B T$  to  $28 k_B T$  for the same MscS channel [46,97]. New approaches are needed. In Chapter 4, we provided the answers to the following questions:

- Can we exploit the recent developments in statistical physics especially non-equilibrium work relations to obtain  $\Delta F$ ?
- If yes, what is the correct definition of work in the context of ion channel

gating that is also faithful to both the first and the second law of thermodynamics?

- Is it possible to provide a general formalism that is valid for not only mechanosensitive but also for voltage-gated ion channels? Can we bridge the gap between recent developments in non-equilibrium thermodynamics of small systems and ion channel biophysics?



## **Chapter 2: Tension-activated channels in the mechanism of osmotic fitness in *Pseudomonas aeruginosa***

Ugur Cetiner<sup>1,3,4</sup>, Ian Rowe<sup>1,2</sup>, Anthony Schams<sup>1</sup>, Christina Mayhew<sup>1</sup>, Deanna Rubin<sup>1</sup>, Andriy Anishkin<sup>1</sup> and Sergei Sukharev<sup>1,3,4</sup>

<sup>1</sup>Department of Biology, <sup>2</sup>Department of Chemistry and Biochemistry, <sup>3</sup>Institute of Physical Science and Technology, <sup>4</sup>Maryland Biophysics Program, University of Maryland, College Park, MD 20742

### **Abstract**

*Pseudomonas aeruginosa* (PA) is an opportunistic pathogen with an exceptional ability to adapt to a range of environments. Part of its adaptive potential is the ability to survive drastic osmolarity changes. Upon a sudden dilution of external medium, such as during exposure to rain, bacteria evade mechanical rupture by engaging tension-activated channels that act as osmolyte release valves. In this study, we compare fast osmotic permeability responses in suspensions of wild-type PA and *Escherichia coli* (EC) strains in stopped-flow experiments and provide electrophysiological descriptions of osmotic-release channels in PA. Using osmotic dilution experiments, we first show that PA tolerates a broader range of shocks than EC. We record the kinetics of cell equilibration reported by light scattering responses to osmotic up- and down-shocks. PA exhibits a lower water permeability and faster

osmolyte release rates during large osmotic dilutions than EC, which correlates with better survival. To directly characterize the PA tension-activated channels, we generate giant spheroplasts from this microorganism and record current responses in excised patches. Unlike EC, which relies primarily on two types of channels, EcMscS and EcMscL, to generate a distinctive two-wave pressure ramp response, PA exhibits a more gradual response that is dominated by MscL-type channels. Genome analysis, cloning, and expression reveal that PA possesses one MscL-type (PaMscL) and two MscS-type (PaMscS-1 and 2) proteins. In EC spheroplasts, both PaMscS channels exhibit a slightly earlier activation by pressure compared with EcMscS. Unitary currents reveal that PaMscS-2 has a smaller conductance, higher anionic preference, stronger inactivation, and slower recovery compared with PaMscS-1. We conclude that PA relies on MscL as the major valve defining a high rate of osmolyte release sufficient to curb osmotic swelling under extreme shocks, but it still requires MscS-type channels with a strong propensity to inactivation to properly terminate massive permeability response.

### **Introduction**

Powerful adaptive mechanisms to environmental changes are characteristic of all commensal or pathogenic microorganisms that propagate between hosts through soil or fresh water. Unlike enteric species such as *Escherichia coli* (EC), dwelling primarily in guts, *Pseudomonas aeruginosa* (PA) is an opportunistic pathogen adaptable to a broader range of habitats, including soil, freshwater [98], medical

equipment [99], the urinary tract [100], tissues and airways of immunocompromised and cystic fibrosis patients [101,102]. Part of its adaptive potential derives from the ability to quickly adjust its turgor pressure under conditions of drastically varied osmolarity. Adaptation of PA to higher osmolarity, as in most bacteria [103], involves accumulation of common compatible osmolytes such as glycine betaine and more specific N-acetylglutaminylglutamine amide [104]. A steady PA growth at high osmolarity alters transcription levels of at least 66 genes coding for a variety of functions including osmoprotectant synthesis enzymes, hydrophilins, type III secretion systems and associated cytotoxins, as well as two-component signaling systems [105]. The organism also survives large osmolarity downshifts; a hypotonic shock from standard LB into distilled water was used in several studies to release periplasmic proteins from PA [106,107]. It was noted that cytoplasmic proteins did not appear in the shock fluid, and cell viability did not suffer as a result of this procedure. Apart from that, the PA response to hypoosmotic shock has not been studied in any detail.

*E. coli* served as the first bacterial model for studies of osmoregulation [108–110] and hypoosmotic responses [48,111]. In 1962 Britten and MacClure [36] reported that during abrupt osmotic downshock bacteria can release ~95% of their total amino acid pool, remaining completely viable. They assumed that the metabolites are released when “the cell passes through a transient state in which the structures (e.g. the cytoplasmic membrane and/or the cell wall) are distended”. When patch-clamp traces of giant *E. coli* spheroplasts [40] and liposome-reconstituted inner membrane proteins [42] were recorded, the notion of stretch-activated channels

acting as possible turgor pressure regulators has replaced this early hypothesis. Identification and cloning of the two most represented inner membrane mechanosensitive (MS) channels, MscL [34] and MscS [35], and preparation of the double (*mscL*-, *mscS*-) knock-out strain has since demonstrated that these two channels fulfill the function of osmolyte release valves rescuing cells from abrupt osmotic downshock [35]. Expression of either MscL or MscS extends the tolerated range of downshocks from 300 mOsm (in the double null mutant) to 900-1000 mOsm [35]. Under strong osmotic down-shocks, fast osmolyte exchange in living cells may take as little as 50-100 ms [53].

The low-threshold MscS channel [35], which exhibits adaptive behavior [46,51], and the high-threshold MscL [112] were recognized as major contributors to the graded tension-driven permeability responses in *E. coli* [94,113,114]. Further efforts identified five additional MscS-related proteins in *E. coli*, which form low-abundance mechanosensitive channels [91,92] capable of alleviating moderate and gradually imposed osmotic downshifts [30]. The studies emphasized the importance of two parameters: channel density in the membrane [94,95] and the rate of osmotic downshift in defining the lytic threshold and survival range for bacteria [30].

The osmotic survival data obtained in MS channel knock-out strains [30,35,115] have indicated that the peptidoglycan layer alone cannot restrain cell swelling to prevent lysis at strong shocks. As the magnitude of osmotic shock increases, water influx must stretch the peptidoglycan, generating tension in the membrane that can activate MS channels, which then start dissipating the osmotic

gradient. This sequence suggests a simple kinetic criterion for the effective channel-mediated rescuing mechanism: the cell will remain mechanically stable in the range of osmotic gradients as long as the efflux of small intracellular osmolytes can outpace the osmotic influx of water, and thus limit cell volume increase and membrane stretching. Before one can propose a quantitative model of this process and predict in what situations the cell will be rescued or ruptured, we need a detailed multi-level phenomenological description of the system, taking into account the whole-cell osmotic behavior as well as molecular components and events in the membrane. A comparative approach that takes into consideration two distantly related gram-negative bacterial species may point to critical parameters.

In the present work we perform initial osmotic viability tests on early logarithmic cultures of *P. aeruginosa* and find that it can tolerate stronger shocks than *E. coli*. We continued with stopped-flow measurements of water and osmolyte exchange in the two strains and found that *P. aeruginosa* has an overall kinetic advantage in both processes in terms of curbing water influx. We devised a procedure for giant spheroplast preparation and performed a patch-clamp characterization of MS channels in the native membrane of *P. aeruginosa*, which reveals a different structure of the channel population compared to *E. coli*. We cloned and characterized two MscS-like and one MscL-like channel species from PA, which are substantially distinct from their EC orthologs. The data provides us with the first experimental ground to relate the whole-cell osmoprotective responses in bacteria with the densities and electrophysiological properties of mechanosensitive channel components in their native membranes contributing to osmotic resistance.

## Materials and Methods

### Strains and media

We chose Frag1, a wild-type *E. coli* strain which was previously used in studies of potassium transport [116] and is a parental strain for a collection of MS channel deletion strains [35,91]. For heterologous expression of PA MS channels we used the MJF641 (aka  $\Delta 7$ ) strain derived from Frag-1 devoid of seven endogenous MS channel genes ( $\Delta mscL$ ,  $mscS$ ,  $mscK$ ,  $ybdG$ ,  $ynaI$ ,  $ybiO$  and  $yjeP$ ) [91]. Both *E. coli* strains were gifts from Dr. Ian Booth (University of Aberdeen, UK). In addition, we used PB104 ( $\Delta mscL$ ) [117] and PB113 ( $\Delta mscS$ ,  $mscK$ ) [43] strains to characterize individual cloned PA mechanosensitive channels in the presence of EC counterparts. The wild-type PA-14 strain of *P. aeruginosa* was provided by Dr. Vincent Lee (UMD).

### Osmotic survival assays.

Only early logarithmic cultures ( $OD_{600} \sim 0.25$ ) were used in all experiments since the cells are larger [118] and more sensitive to osmotic conditions. From standard overnight cultures, cells were transferred to the high-osmotic LB medium (HiLB) adjusted to 1200 mOsm by adding 413 mM (24 g/l) NaCl to a standard LB medium. With a small inoculum (1:700), cells were allowed to go through 5-6 duplications; in HiLB it took 4-5 hrs to reach  $OD_{600}$  of 0.25. This OD marks a true early logarithmic stage for PA an EC because both strains are able to grow to an OD of 2.5-2.7 under these conditions. 100  $\mu$ l culture aliquots were abruptly diluted into 5 ml of media of lower osmolarity. After 15 min incubation at room temperature, shocked bacteria were sequentially diluted 1:25 in the same shock medium twice, and

75  $\mu$ l aliquots were plated in triplicates. Because wild-type bacteria were completely tolerant to low and intermediate shocks, a standard set of shock media included LB (400 mOsm), MLB (250 mOsm), MLB/2 (125 mOsm), MLB/5 (50 mOsm) and deionized water (ddH<sub>2</sub>O, 0 mOsm) Colonies were manually counted next morning. The colony number divided by the number in un-shocked control (diluted into HiLB) in each particular experiment was taken as the survival fraction. Independent shock experiments were repeated at least six times.

#### Stopped-flow experiments.

Cells were grown in either MLB (250 mOsm) or HiLB (1200 mOsm) for the up-shock or down-shock experiments, respectively. Cells harvested at OD<sub>600</sub> of 0.25 were concentrated with a brief centrifugation and brought to OD<sub>600</sub> of 2.2. Dilutions of HiLB with sterile deionized water produced down-shock media of 900 (3/4), 800 (2/3), 720 (3/5), 600 (1/2), 450 (3/8), 300 (1/4) and 150 (1/8) mOsm.

A BioLogic SFM-2000 stopped flow machine equipped with two independent motorized syringes, a 21  $\mu$ l optical mixing chamber, modular spectrophotometer and a computer for protocol programming and data acquisition was used in experiments. The small-angle scattering from the suspension upon rapid (~8 ms) mixing was measured with a PMT tube covered with a special insert masking the straight incident light in the center within the 5° angle (custom engineered at Bio-Logic Science Instruments). The light was collected in the range between 5 and 12 degrees. Because we used non-collimated light entering the chamber from the light guide, we observed a substantial amount of ‘stray’ light captured by the PMT. The fraction of signal

attributable to scattering from cells was extracted by subtracting stray light contribution obtained in mixing controls with pure HiLB supernatant without cells. The mixing ratio in shock experiments was always 1:10, (176  $\mu$ l cell suspension + 1760  $\mu$ l dilution medium) delivered into the optical cell at the total rate of 8.5 ml/s. The scattering kinetics was collected for 4 s, and 5-7 sequential trials were averaged. Changes of scattering reflecting the fast processes of water or solute equilibration typically completed within 0.5-1 s.

In Rayleigh-Gans approximation [119], the intensity of the forward scattered light measured at a given density of cell suspension grows monotonously with the cell volume and refractive index difference between the cell ( $n_{\text{cell}}$ ) and the medium ( $n_{\text{m}}$ ). The refractive index of the cell, in turn, depends on the total concentration of solutes inside. Although the exact theoretical expression for the small-angle scatter is rather complex (see Supplement), two specific cases may yield easily tractable scaling relationships. For up-shocked cells undergoing a moderate osmotic shrinking (water leaves while all osmolytes remain inside), the intensity of scattering can be well approximated by the volume to the power of  $-(2/3)$ , i.e. inverse of the cell surface area [120]. The same dependence takes place for the initial stage of osmotic swelling under hypoosmotic shock, before the osmolyte release has started. However, after the bacteria expand longitudinally [121] and reach their maximum size (the volume can increase by up to 23%) [122], further changes in cell dimensions and shape are relatively small and apparently curbed by both peptidoglycan rigidity and ensuing osmolyte dissipation. When membrane tension reaches activation threshold for the channels and osmolyte release begins, the subsequent changes in the scattering are



mainly due to the changes of cellular refractive index, which reflects the concentration of all solutes inside. At this stage, scattering is roughly proportional to the square of solute mass inside the cell. Under the assumption that the release of osmolytes is an exponential process with characteristic time of  $\tau$ , the time courses of light scattering were fitted with the following equation:

$$I = I_0 + S(m_i + m_p e^{\frac{t_0-t}{\tau}})^2 \quad (1)$$

where  $I_0$  is the constant offset accounting for stray light,  $m_i$  and  $m_p$  are the fractions (masses) of impermeable and permeable osmolytes, respectively,  $S$  is the scaling constant and  $t_0$  designates the start of the fitting interval. Derivation of this equation can be found in the Supplement and experimental details of particular up-shock and down-shock experiments can be found in the text and figure legends.

To determine water permeability rates we performed osmotic up-shock experiments on cells grown in MLB. The kinetics of light scattering increase due to cell shrinkage in a hypertonic medium were recorded at different osmotic gradients and rate constants were determined from mono-exponential fits. The osmotic water permeability coefficient  $P_f$  was calculated according to [123]:

$$P_f = \frac{k}{\left(\frac{S}{V_0}\right)V_w\Delta C} \quad (2)$$

Where  $k$  is the rate constant of scattering signal change ( $s^{-1}$ ) calculated from mono-exponential fit;  $\frac{S}{V_0}$  is the initial surface area to volume ratio;  $V_w$  is the partial molar volume of water (18  $cm^3/mol$ );  $\Delta C$  is the difference of osmolality between inside and outside. The sizes of PA and EC cells in early logarithmic cultures were measured

microscopically under 60× DIC objective as in [124]. Histograms of length and width distributions were generated from manual measurements on 300-400 cells of each type. Surface areas and volumes of cells were calculated in the approximation of a cylindrical shape capped with hemispheres:  $SA=4\pi r^2+2\pi rl$  and  $V=4/3\pi r^3+\pi r^2l$ .

#### Preparation of giant spheroplasts and patch-clamp

The standard procedure of giant spheroplast preparation from *E. coli* [40] begins with growth in the presence of 0.06 mg/ml Cephalexin, which blocks cell septation. Within 1.5-2 hours, the growing but not dividing bacteria form 100-250 μm long filaments. The filaments are transferred into a hypertonic buffer (1 M sucrose) and treated with lysozyme (0.2 mg/ml) in the presence of 5 mM EDTA, which degrades the peptidoglycan layer within 5-10 min. As a result, filaments collapse into spheres 3-7 μm in diameter. The reaction is stopped by excess  $Mg^{2+}$  that terminates the effect of EDTA and activates DNase. Sedimentation through a one-step sucrose gradient separates the spheroplasts from the rest of the reaction mixture.

The procedure of *P. aeruginosa* giant spheroplast preparation was similar, but with two modifications. Instead of Cephalexin, the PA filaments were grown in the presence of 0.2 mg/ml Carbenicillin (1.5-2 hrs). Filaments were collected by low-speed centrifugation, resuspended in 1M sucrose and subjected to the ‘plasting’ reaction in the presence of 10 mM EDTA and 0.6 mg/ml lysozyme for 15-20 min. Spheroplasts were separated from the debris by centrifugation through a one-step sucrose gradient, aliquoted, and stored at -80C.

Borosilicate glass (Drummond 2-000-100) pipets 1-1.3  $\mu\text{m}$  in diameter were used to form tight seals with the inner membrane. All recordings were done in excised inside-out patches in symmetrical 200 mM KCl, 10 mM CaCl<sub>2</sub>, 90 mM MgCl<sub>2</sub> solution buffered by 10 mM HEPES (pH 7.2). Currents were recorded in voltage-clamp mode under pre-programmed mechanical stimuli combined from steps or ramps of negative pressure (suction) delivered from a modified HSPC-1 pressure clamp apparatus (ALA Instruments).

Cloning of MS channel genes from PA.

*E. coli* MscS and MscL protein sequences were used to search the PA14 genome using the BLAST tool in the NCBI database. A single homolog of MscL and six proteins of different length with detectable homology to MscS were found. The alignments identified two MscS homologs of similar length (278-283 amino acids). Using primers complementary to the flanking sequences, the three open reading frames were PCR-amplified and subcloned into the pB10d vector [125] as BglII-HindIII fragments. The identity of inserts to the reference sequences in the PA14 genomic database was confirmed by automated sequencing. PaMscL (PA14\_61050), PaMscS1 (PA14\_57110) and Pa MscS2 (PA14\_65040) were expressed in MJF641 *E. coli* cells, and giant spheroplasts were generated enabling patch-clamp examination of these individual channel species.

## **Results**

### ***P. aeruginosa* versus *E. coli*: osmotic survival and kinetics of osmolyte and water exchange.**

Cells grown in HiLB (1200 mOsm) were diluted into media of different osmolality, incubated for 15 min, additionally diluted in the same final shock medium to an optimal plating density, and plated. This initial high-osmotic condition, while permitting cell growth, allowed for downshifts strong enough to reduce cell survival rates down to 0.5-1%. Fig. 2.1A depicts the results of colony counts which shows that both wild-type PA and EC strains, carrying a full complement of MS channels, are completely resistant to osmotic downshifts of up to 800 mOsm in magnitude (downshift endpoint of 400 mOsm). At shocks higher than 950 mOsm, the viability of both strains starts declining, with a more pronounced loss in EC. PA shows a marked decline only at 1150 mOsm downshift. This indicates that cells pre-adapted to higher osmolarity, i.e. having accumulated high concentrations of osmolytes, become vulnerable to osmotic downshock. As seen from Fig. 2.1A, the range of osmotic shocks tolerated by EC (grown in HiLB) is narrower than that for PA. Apparently, under such conditions the accumulated osmolytes cannot be ejected fast enough and the influx of water leads to a critical surge of turgor pressure that damages the cell. The fact that PA survives drastic shocks better may suggest that the overall osmolyte handling system in PA is more efficient. In the following sections we will address the questions of timing of cell equilibration and the nature of changes of membrane permeability for this organism.

Note that both cultures were largely ‘wiped out’ in distilled water, showing only 0.1-0.4% survival. When shocked into distilled water not from HiLB, but from standard LB (400 mOsm), PA and EC survival rates are  $13 \pm 7\%$  and  $46 \pm 9\%$  ( $n=4$ ), respectively. The magnitude of shock in this instance is relatively small (400 mOsm), and the experiments above showed that bacteria easily tolerate an 800 (1200  $\rightarrow$  400) mOsm downshift (Fig. 2.1A). The cells apparently suffer more from ion depletion in deionized water rather than osmotic rupture, and EC cells are more tolerant to this type of perturbation.

To observe the osmolyte release in real time, we measured the kinetics of forward light scattering from HiLB-adapted EC and PA cells to abrupt dilutions into media of different osmolarity using the stopped-flow technique. Figures 2.1B and C show series of scaled light scattering traces recorded on PA and EC, respectively, obtained at different magnitudes of shock. The set of initial traces is presented in supplemental Fig. S1, but for the ease of comparison, the traces shown in Fig. 2.1B and C are normalized such that the maximal scattering level immediately after mixing ( $t=10$  ms) was equated to unity and the curves represent fractional scattering decrease in the course of swelling and osmolyte release. In EC, the fast kinetics of scattering decrease was usually completed by 0.3 s, with amplitudes ranging from 15% at the mild shock to 55% at strongest shocks, relative to the initial scattering level attributable to the presence of cells (after subtraction of stray light signal). For PA, the fast processes at all shocks completed by 150 ms, with practically no scattering change at mild downshift ( $\sim 2\%$ ) and a  $\sim 35\%$  signal decrease at the strongest shock.

According to Rayleigh-Gans approximation for bacterial turbidity [119], the small-angle scattering grows monotonously with the difference in refractive indexes inside and outside the cell. The refractive index inside is roughly proportional to the non-aqueous content of the cytoplasm and the light scattering signal due to osmolyte loss in hypoosmotic medium is proportional to the square of cellular anhydrous mass and the decrease of scattering reflects the combined effect of all permeable osmolyte loss. In case of severe shocks, the scattering from EC suspension drops by half (Fig. 2.1C), suggesting that cells lose about 30% of their internal non-aqueous components. Assuming that macromolecules stay inside, the cells likely release the major part of their small molecules [36]. From the amplitude of scattering signal (35%, Fig. 2.1B) one may conclude that PA loses about 19% of its internal light-refracting content at most severe shocks, which is less than EC.

From Figs. 2.1B, C and supplemental Figs. S1-S3 one may see that each curve begins with a noisy part representing the turbulent mixing period (~8 ms) followed by a low-slope region reflecting cell swelling. The swelling period shortens as the shock magnitude increases. The nature of this initial period will be further investigated, but currently we presume that during this time the turgor pressure and tension build up until reaching a critical level that activates the mechanosensitive channels which then start dissipating osmolytes. At this moment the scattering curve bends down. During the falling phase, which becomes steeper as the shock magnitude increases, different fractions of the channel population open and release osmolytes at different rates, while the continuing water influx maintains an above-threshold tension in the inner membrane. Finally, when the osmotic gradient is sufficiently dissipated, tension drops

to a sub-threshold level, the channels close and the signal flattens. The general trend is that with the increasing shock magnitude the swelling period shortens and the release phase becomes faster, also generating a larger overall scattering drop due to increased amounts of solutes ejected from cells. Fits of experimental traces to equation 1 (presented in supplemental Figs. S2 and S3) describe the fast falling phase of osmolyte release in both PA and EC reasonably well.

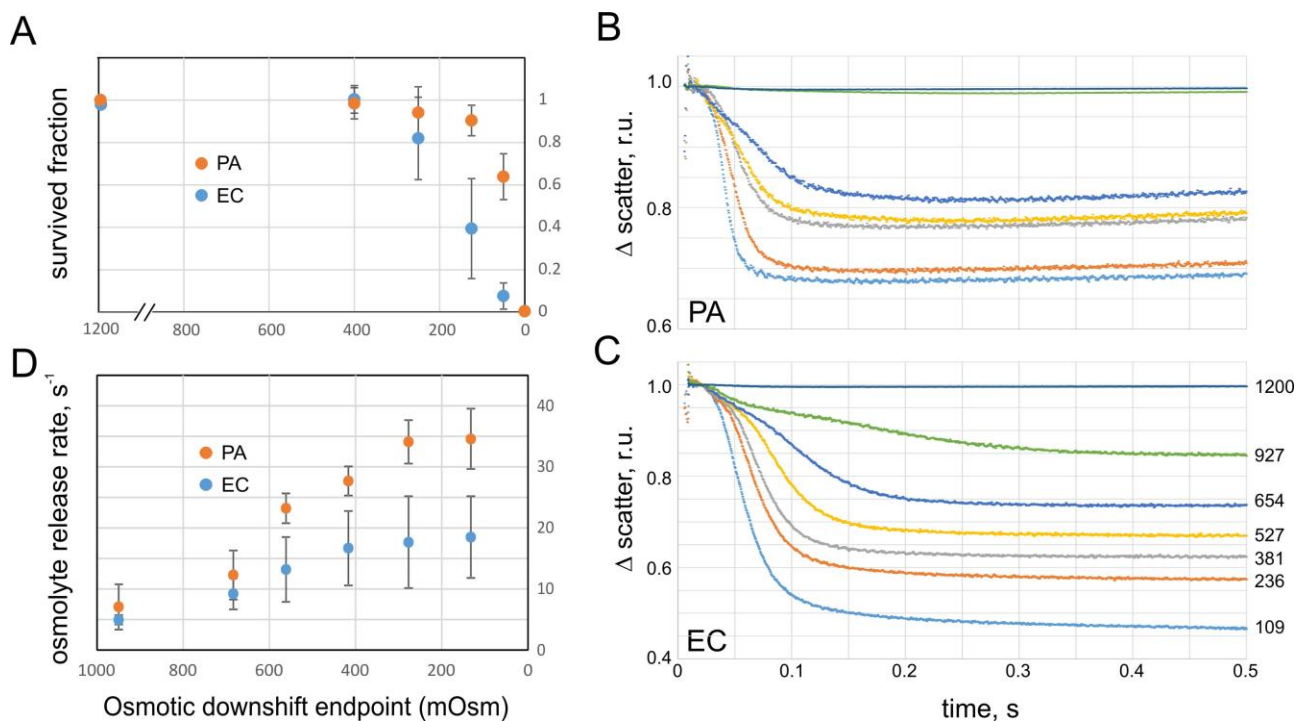


**Figure 2.1. Osmotic survival correlates with osmolyte exchange rates.** (A) Fractions of wild-type *P. aeruginosa* (PA14) and *E. coli* (Frag1) surviving osmotic downshock as assayed by plate counts. The symbols and bars represent mean and standard deviation,  $n=6$ . The x-axis represents the end osmolarity upon a downshift from the initial 1200 mOsm ( $p < 0.01$  and  $p < 8E-6$  for the last two pairs of data points, respectively). Stopped-flow recordings of small-angle light scattering changes upon mixing of suspensions of PA (B) and EC (C) with a 10-fold excess of low-osmolarity media (averages of 5 sequential trials). The numbers by curves denote the osmolarity at the end of downshift from 1200 mOsm (downshift endpoint). The 1200 mOsm medium (HiLB) was standard LB supplemented with 413 mM of NaCl (see Methods). The scattering traces reflect the kinetics of dissipation of osmolytes contributing to the refractive index of the cytoplasm. The fastest exponential components of rates of release are presented in panel D, which has its shock magnitude axis aligned with panel A. The osmolyte release rates are nearly equal at moderate shocks, however at high shocks,

specifically in PA, the rate sharply increases, which correlates with higher survival mOsm ( $p < 0.01$  and  $p < 0.001$  for the last two pairs of data points, respectively). For all experiments, the cultures were taken in early logarithmic phase ( $OD_{600}$  of 0.25). Anthony Schams performed and analyzed the down-shock stopped-flow and the survival experiments.

EC traces (Fig. S3), however, reveal a slower process leading to a slight deviation from the fit toward the end of 0.5 s traces. Fig. 2.1D shows the dependencies of the release rate on the magnitude of osmotic downshift. The x-axis of this graph is aligned with the viability graph on panel A. Up to the shock magnitude of 800 mOsm (end point of 400 mOsm), viabilities of both EC and PA are uncompromised, and the release rates from both types of cells are statistically indistinguishable. At stronger shocks, when the decline of cell viability begins and the EC osmolyte release system seems to have reached its capacity, the release rate in PA keeps increasing and saturates only at strongest shocks, which correlates with the better PA survival. Indeed, the PA release system is able to absorb stronger shocks by working faster. Because the initial swelling rate depends primarily on water permeability through the cell envelope and the osmotic gradient, we performed opposite up-shock experiments measuring cell shrinkage that reflects water efflux rates (Fig. 2.2). From mono-exponential fits of the scattering traces we obtained the rates of cytoplasmic volume change as a function of shock magnitude for PA and EC, respectively (Fig. 2.2A, B, insets). The results indicate that the rate of cytoplasm condensation in EC is a nearly linear function of the shock magnitude. In PA, however, this rate had a hyperlinear dependence on shock magnitude.



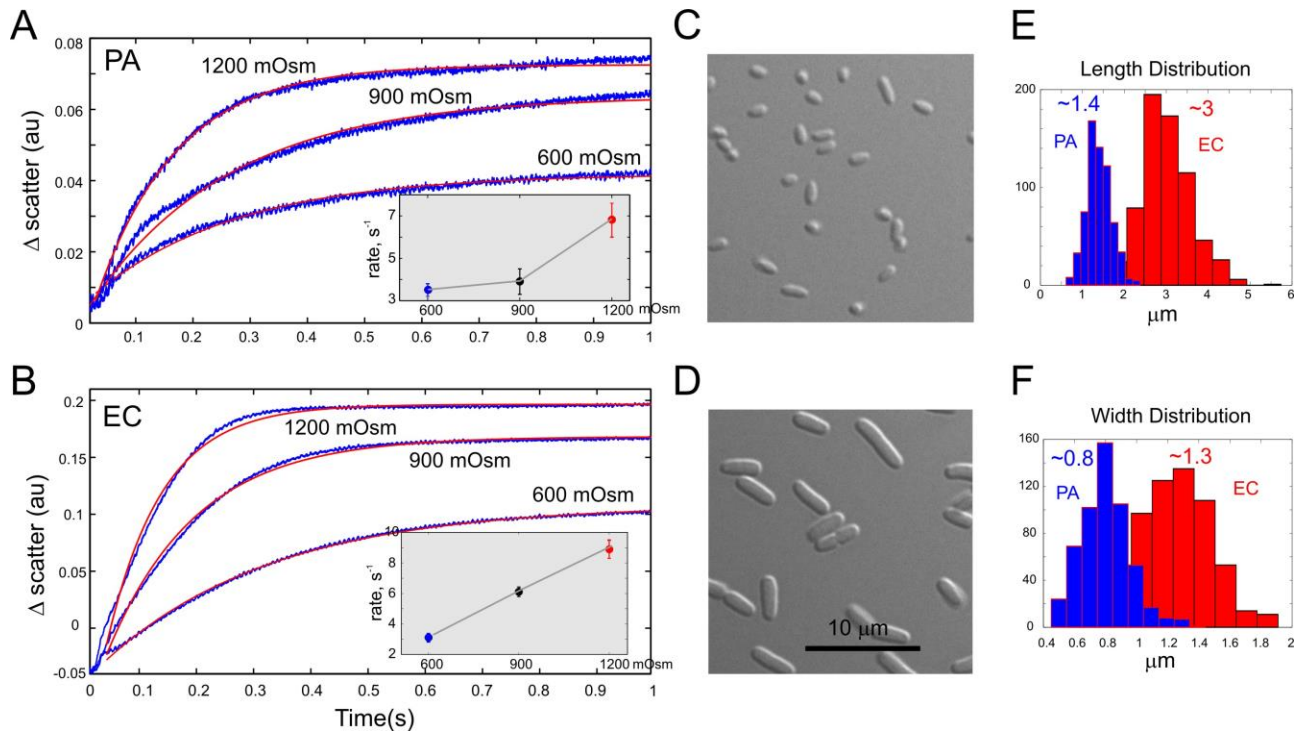


**Figure 2.2. Stopped-flow recordings of small-angle light scattering upon mixing of suspensions of PA (A) or EC (B) grown in MLB (250 mOsm) with 10-fold excess of higher-osmolarity media (indicated by the traces). Experimental traces (blue) are overlaid with monoexponential fits (red). The traces signify shrinkage of bacteria caused by osmotic efflux of water through the cytoplasmic membrane. Increased concentration of intracellular solutes and the accompanying increase of refractive index produce increase in scattering. Both cultures were grown to  $OD_{600}$  of 0.25 and imaged under DIC (C, D). Histograms of length (E) and width (F) distributions were generated from microscopic measurements on 300-400 cells of each type. The average sizes of PA and EC cells were  $1.4 \times 0.8$  and  $3.0 \times 1.3$   $\mu\text{m}$  (length  $\times$  width). The assumption that cells are cylinders with spherical ends produces surface areas of 3.5 and 11.3  $\mu\text{m}^2$ , and cell volumes of 0.57 and 2.94  $\mu\text{m}^3$ , respectively. The surface area-to-volume ratios are 6.18 and 3.85  $\mu\text{m}^{-1}$  for PA and EC, respectively.**

This slower shrinkage can be a consequence of a ‘crowded’ cytoplasm in PA, which at smaller shocks may resist compaction and desolvation. The resting level of the internal turgor pressure in each cell type might also be a contributing factor.

Following [123,126], we estimated the water permeability coefficient ( $P_f$ ) utilizing the parameter of surface area-to-volume (SA:V) ratio for the osmotically active compartment. In the assumption that cells are cylinders with spherical caps at each end, with mean dimensions presented in Fig. 2.2, the corresponding SA:V ratios

are  $3.8 \pm 0.1$  and  $6.2 \pm 0.8 \mu\text{m}^{-1}$  for EC and PA, respectively. For the rate constants of scattering signal of  $3.5 \pm 0.3$  and  $3.2 \pm 0.2 \text{ s}^{-1}$  measured at 600 mOsm shock,  $P_f$  values were  $(2.0 \pm 0.7) \times 10^{-2} \text{ cm/s}$  for PA and  $(3.1 \pm 0.9) \times 10^{-2} \text{ cm/s}$  for EC, with uncertainties estimated using the error propagation rules taking contributions from all parameters. We found that at higher shocks the calculated  $P_f$  values become considerably lower. Larger volume perturbation potentially invokes other factors that may resist compaction such as macromolecular crowding [127]. Because the cells in this case may not behave like ideal osmometers, we favor the  $P_f$  values obtained with the lowest degree of osmotic and mechanical perturbation. From these measurements we conclude that smaller PA cells have a lower water permeability, which in the event of abrupt osmotic swelling buys more time for osmolyte release.

### ***E. coli* and *P. aeruginosa* spheroplast preparation, patch-clamp channel activation in situ**

To obtain a ‘microscopic’ picture of osmotic permeability increase and characterize channel activities in native membranes, giant spheroplasts of both Frag-1 and PA-14 strains were prepared. Frag-1 formed filaments in the presence of standard concentration of cephalixin (0.06 mg/ml), which were then converted into 3-6  $\mu\text{m}$  spheres with lysozyme in the presence of EDTA within 5-10 min. We attempted the same procedure on *P. aeruginosa* only to find that the PA14 strain is completely insensitive to cephalixin. However, following earlier work by Hubert [128] we were able to effectively induce filamentous growth of PA in the presence of 0.2-0.3 mg/ml carbenicillin (Fig. 2.3). PA filaments were sensitive to lysozyme, but the ‘plasting’

reaction required double amounts of lysozyme and EDTA and an extended reaction time (15-20 min) compared to EC.

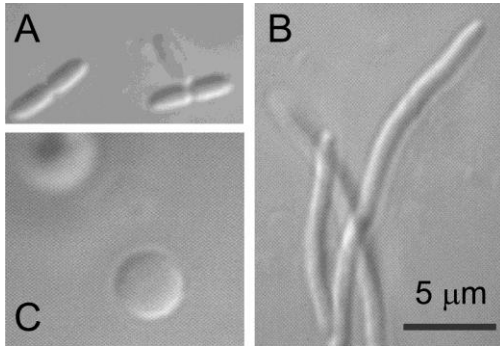


**Figure 2.3. Steps in the giant spheroplast preparation as viewed by DIC microscopy. (A)** Intact *P. aeruginosa* (PA14) cells. **(B)** Filamentous forms induced by carbenicillin and **(C)** giant spheroplasts after lysozyme digestion. The scale bar in Panel B applies to Panel A and C as well.

Formation of giga-ohm seal with borosilicate glass pipettes (tip diameter of 1-1.3 μm) took an average of 5-10 min at constant 15-30 mmHg suction. Patch excision was achieved by gently tapping the micromanipulator (no air exposure). Typical pressure ramp responses recorded in EC and spheroplasts are shown in Fig. 2.4. Pipette pressure was linearly increased within 1 s from 0 mm Hg to saturating pressure (~250 mm Hg), at which all active channels are found in the open state ( $P_o \sim 1$ ). Recordings from native patches reveal that the cytoplasmic membranes of both organisms harbor MS channels at comparable densities. In EC, two distinct waves result from early activating MscS family channels and the late-acting MscL population (Fig. 2.4A). The PA membrane displays much smaller wave attributable to MscS-like channels. Half of the patches do not show a characteristic two-wave response (supplemental Fig. S4). The lack of clear separation between the PaMscS and PaMscL waves suggests that *P. aeruginosa* might have a different structure of channel population: a larger variety of channels with different gating tensions and conductances may give rise to some overlap of their activities in ramp responses.

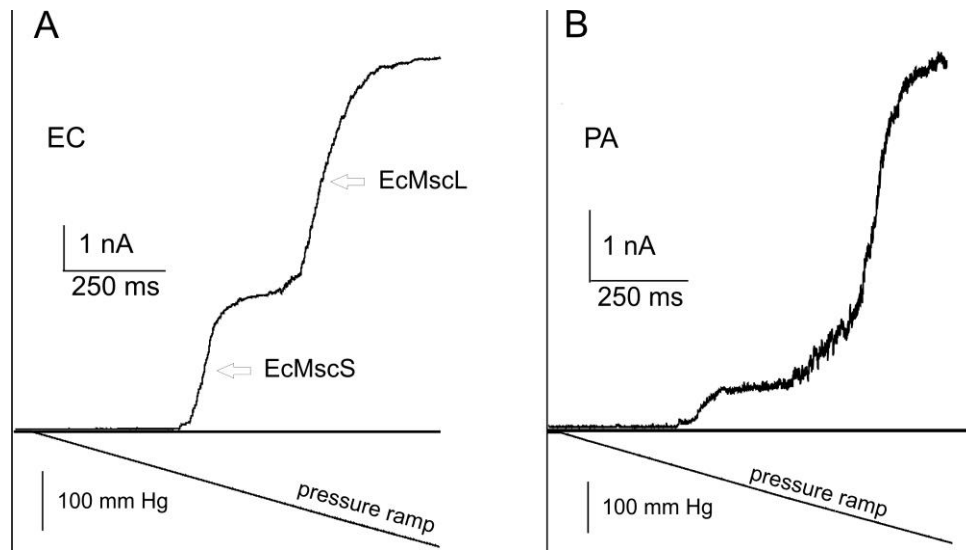


**Figure 2.4. Pressure ramps applied to excised patches of native MS channel populations in EC and PA produce comparable conductance responses.** (A) The characteristic double-wave pattern is observed in EC patches. The channel population in *E. coli* patch contains approximately 60 MscS and 50 MscL channels. (B) PA always shows a smaller proportion of low-threshold MscS-like channels compared to more dominant MscL-like channel population (~80 per patch, see Table 2 and supplemental Fig S4). The symmetric recording buffer contained 200 KCl, 90 mM MgCl<sub>2</sub>, 10 mM CaCl<sub>2</sub> and 10 mM Hepes (pH 7.2).

Ramp responses recorded from multiple patches provided us with single-channel conductances and sufficient statistics of channel numbers per patch (Fig. S4, Table 2.1). On assumption that the tension midpoint activating high-threshold MscL channels is the same and equal to 12 mN/m, we calculated the radius of patch curvature in each experiment. Again, assuming that under the tension of 12 mN/m the patch is a hemisphere, we estimated patch area and channel densities. From the numbers it is evident that PA has its MscL at a higher density and apparently relies more on this type of channel.

**Table 2.1.** Numbers and densities of channels in native inside-out patches from ramp traces recorded from PE (PA14) and EC (Frag1) giant spheroplasts. A  $\pm 15\%$  uncertainty in the absolute values of midpoint tensions for EC and PA MscL may result in a  $\sim 30\%$  error in patch area and a similar error in channel density estimation.

Cell type	# MscS per patch	# MscL per patch	Midpoint ratio $p_{MscS}/p_{MscL}$	MscL midpoint (mmHg)	Patch radius, $\mu\text{m}$	Patch area, $\mu\text{m}^2$	MscS/ $\mu\text{m}^2$	MscL/ $\mu\text{m}^2$	n
Frag1	62 $\pm$ 6 (1 nS)	47 $\pm$ 3 (3 nS)	0.58 $\pm$ 0.02	156 $\pm$ 4	1.3 $\pm$ 0.1	11 $\pm$ 1	6 $\pm$ 1	4.4 $\pm$ 0.3	12
PA14	13 $\pm$ 4 (0.97 nS)	78 $\pm$ 10 (2.1 nS)	0.54 $\pm$ 0.02	162 $\pm$ 13	1.4 $\pm$ 0.2	13 $\pm$ 3	1.2 $\pm$ 0.4	7 $\pm$ 1	8

In the next experiments we tested how repeatable are population currents depending on pre-conditioning tension. The purpose of these trials was to determine the fraction of population that may adapt or inactivate. We adjusted the amplitude of stimuli to probe either the entire population (low- and high-threshold) or only the low-threshold population. The data presented in Fig. 2.5 reveal that specifically the low-threshold populations in both organisms are prone to tension-dependent inactivation. A pulse-step-pulse protocol was used in two different modes to visualize inactivation. In the ‘saturating’ mode (Fig. 2.5A, C), we used the first pulse at saturating amplitude to reveal the entire active population of channels in the patch. The test pulse was followed with a lower-amplitude conditioning step (usually near half-saturating pressure), during which part of the population could redistribute between the open, closed and inactivated states. The same saturating test pulse applied at the end reveals the fraction of non-inactivated channels available for opening. As seen from Fig. 2.5A, the entire active PA channel population may lose up to 30% of the current after being subjected to a 6-s sub-saturating conditioning step (indicated by black and red

arrows). The entire EC population, when subjected to sub-saturating steps loses less activity (Fig. 2.5C). However, when we scaled down the amplitudes of mechanical stimuli to probe only the low-threshold fraction of channels, we see a larger fractional reduction of the current at the end, indicative of a massive channel outflow into the inactivated state. The experiment illustrates that similar to EC and *Vibrio cholerae* [96] the low-threshold PA population is prone to strong tension-dependent inactivation (Fig. 2.5B). As was suggested before [49], the physiological purpose of channel ‘disengagement’ at moderate prolonged stimuli is to avoid flickering between open and closed states and prevent dissipation of metabolites at non-threatening tensions.

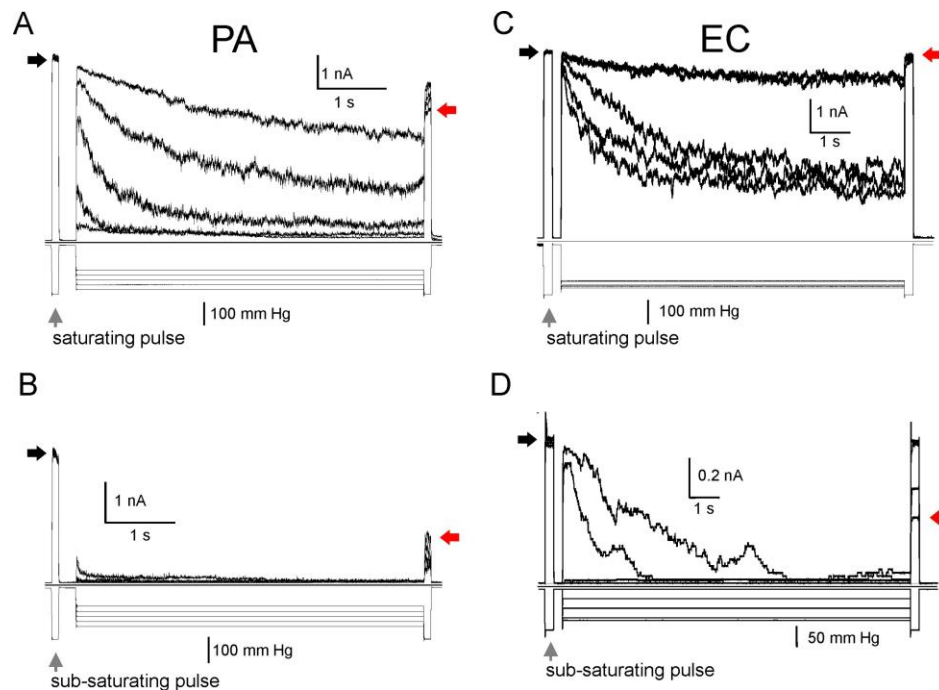


**Figure 2.5. The low- and high-threshold sub-populations of native channels in *E. coli* (A, B) and *P. aeruginosa* (C, D) exhibit distinctive adaptive behaviors.** Exposure of excised patches to prolonged moderate tension produces massive inactivation of the native low-threshold channel population. Step-pulse-step protocol visualizes the degree of tension-

dependent inactivation. The first 0.1 s pressure pulse invokes approximately 50% of total patch conductance, engaging the low-threshold population. The following 10 s step of variable amplitude conditions the low-threshold population, and the last pulse equal in amplitude to the first reveals the much smaller population that remains active after the conditioning step (**B, D**). When the same protocol utilizes saturating pulses (engaging the entire channel population) and a broader range of conditioning steps, a larger fraction of the population remains active (**A, C**). The experiment shows that the low-threshold population in *P. aeruginosa* is especially prone to inactivation. Red arrows indicate current levels produced by the remaining channel population at the end compared to the amplitude of response to the initial pulse (black arrows).

### **Genomic databases predict one MscL and two MscS-like channels in *P.***

#### ***aeruginosa***

Searching the PA14 gene and protein databases with *E. coli* MscL and MscS sequences revealed one MscL-like protein PA14\_61050 (PaMscL) with 64% amino acid identity to EcMscL and two MscS-like proteins, PA14\_57110 (PaMscS-1) and PA14\_65040 (PaMscS-2) with 36% and 29% identity to EcMscS, respectively. Four additional proteins belonging to the MscS family, but with lower overall homology were found (see supplemental Table S1).

Based on the amino acid sequence alignments and homology models, (PaMscL is predicted to have a more hydrophobic gate than *E. coli* MscL (V23→I substitution) (10), a possibly lower conductance, a different pattern of charges in the N-terminal and periplasmic domains, and increased flexibility in the TM2 helix (A95→G). An additional two prolines in the TM2-S3 linker suggest that there must be a lower probability of helix formation in this generally disordered segment [114].

Alignments of MscS homologs and homology models reveal a highly conserved organization and preservation of inter-domain contacts. There are several substitutions in critical domains, which may change the conductance, activation

thresholds, as well as propensity to inactivation. For instance, the double glycine motifs in the ‘hinge 1’ locus of both PaMsc-1 and PaMscS-2 (corresponds to single G121 in EcMscS) predict that these channels may have a less stable open state and potentially be more prone to inactivation, or may exhibit a slow recovery (see below).

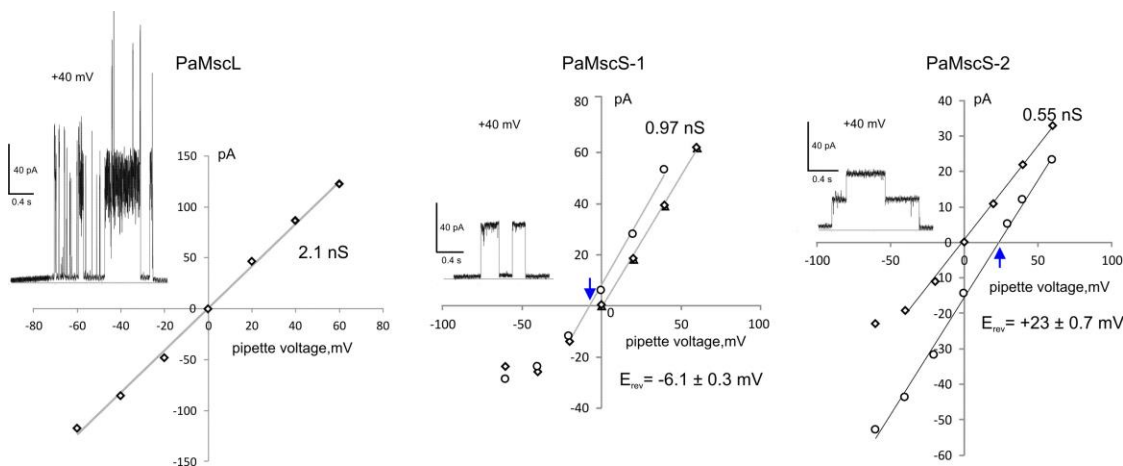


**Figure 2.6. Current-to-voltage relationships for unitary currents measured for PaMscL, PaMscS-1 and PaMscS-2.** The examples of single-channel currents are shown as insets in each panel. Based on the Goldman equation, the  $E_{rev}$  shift for PaMscS-1 in response to 1:5 (pipette/bath) gradient of KCl (relative to symmetric conditions) of -6.1 mV predicts the permeability ratio  $P_{Cl}/P_K$  of 1.5. For PaMscS-2, the  $E_{rev}$  shift of +23 mV (5:1 pipette/bath gradient) predicts  $P_{Cl}/P_K$  of 4.4. Reversal potentials are indicated by blue arrows. The three MS channels were expressed in *E. coli* MJF 641 cells and recorded under symmetric and asymmetric ionic conditions. In the experiment with PaMscS-2 the gradient was inverted (5:1) because for yet unknown reasons no channel activity was observed in the opposite configuration.

### Properties of single channels from *P. aeruginosa*: conductances and ionic selectivity.

Open reading frames coding for PaMscL, PaMscS-1 and PaMscS-2 were PCR-amplified and cloned into the pB10d expression vector. Each of the three proteins were expressed in MJF641 *E. coli* spheroplasts. I-V curves of the cloned PA channels were obtained under both symmetric and asymmetric ionic conditions to determine single channel conductance and selectivity, respectively (Figure 2.6). The



slope of I-V curve under symmetric conditions (200 mM KCl, bath/pipette) revealed PaMscL has a conductance of 2.1 nS, which was 30% less than EcMscL. Under asymmetric conditions (100:500 mM KCl) no shift of I-V curve was observed indicating that PaMscL is nonselective (data not shown). PaMscS-1 has a conductance of ~1 nS, which is similar to its single *E. coli* ortholog, EcMscS. On the other hand, PaMscS-2 has a relatively low conductance of 0.55 nS. In an asymmetric solution containing 5:1 gradient of KCl, the reversal potentials of both PaMscS channels shifted toward the equilibrium potential for Cl<sup>-</sup>, indicating that PaMscS-1 and PaMscS-2 favor anions over cations with  $P_{Cl}/P_K \sim 1.5$  and 4.4 respectively.

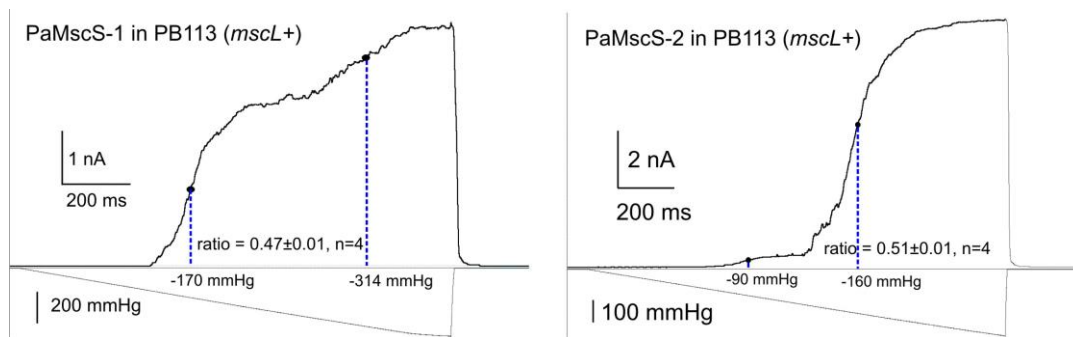


**Figure 2.7. Midpoint determination of *P. aeruginosa* MscS-like channels using MscL as an intrinsic tension gauge.** The homologues PaMscS1 and PaMscS2 were expressed in PB113 *E. coli* cells carrying native MscL. Each of these channels generates a ‘wave’ of current with its own midpoint. The  $p_{MscS}/p_{MscL}$  midpoint ratios for both MscS homologues (~0.5) are slightly lower than that of *E. coli* MscS (~0.6), indicating that these channels open at lower tension. PaMscS-2 is expressed at much lower level despite full induction.

### **Determination of tension sensitivities for *P. aeruginosa* MscS-like channels and their spatial and energetic parameters for activation.**

Without the ability to visualize small spheroplast patches, we used EcMscL present in the PB113 *E. coli* strain to gauge tension midpoints for heterologously

expressed PaMscS-1 and 2. Having a well characterized MS channel as an internal standard in the same patch helps to convert the pressure into tension scale. At a constant patch curvature, ratios of midpoint tensions and pressures ( $\gamma_{0.5}/\Delta P_{0.5}$ ) should stay constant for any channel. Subjected to pressure ramps, PaMscS channels activate first, forming the first wave of current, which is followed by a second wave of MscL (Fig. 2.7) known to half-activate at 12 mN/m. Based on  $p_{\text{MscS}}/p_{\text{MscL}}$  ratios of 0.47 and 0.51, the tension midpoints for PaMscS-1 and PaMscS-2 in this particular setting were determined to be 5.6 and 6.1 mN/m. The activating tension for PaMsc-1, therefore, is slightly lower than that for *E. coli* MscS previously estimated between 6.5 and 7.8 mN/m [46,129]. Likewise, the midpoint of PaMscL was gauged against EcMscS in PB103 *mscL*<sup>-</sup> strain carrying a native copy of MscS. The  $p_{\text{EcMscS}}/p_{\text{PaMscL}}$  ratio in this experiment was  $0.54 \pm 0.01$  (n=3), which is exactly the ratio measured in WT EC spheroplasts (traces not shown). Thus, PaMscL has the same tension midpoint as EcMscL, i.e. around 12 mN/m [130,131].

Having midpoint tensions determined for each channel, the pressure scale on the activation curves was converted to tension. The open probability of the channel can be then fitted to the two-state Boltzmann function  $P_o = 1 / (1 + \exp((\Delta E - \gamma \Delta A) / kT))$  to extract the free energy difference between open-closed state ( $\Delta E$ ) in the absence of tension, and the in-plane expansion of the channel ( $\Delta A$ ) associated with opening (Fig. S5). The estimated spatial and energetic parameters for PaMscS-1 and 2 based on multiple independent patches were very similar. The free energy difference and the in-plane expansion of the closed to open state transition were determined to be  $17.1 \pm 0.5$  kT,  $11.0 \pm 0.5$  nm<sup>2</sup> for PaMscS-1 (n=16) and  $15 \pm 2$  kT,  $10.0 \pm 1$  nm<sup>2</sup> for

PaMscS-2 (n=4), which are comparable with the gating parameters earlier reported for EC MscS [51,53]. See Table 2 for summary.

### **PaMscS-1 and 2 channels exhibit inactivation and slow recovery.**

In Fig. 2.5, we presented traces recorded in native patches that illustrate partial inactivation of the low-threshold PA channel population. This low-threshold population must include PaMscS-1 and 2, which were individually tested for inactivation in MJF641 spheroplasts (Fig. 2.8A, B). As previously, the amount of inactivation for Pa MS channels was probed by a pulse-step-pulse protocol [46,49,51]. After a 10 s conditioning step (at  $p_{0.5}$ ), PaMscS-1 displayed  $30\pm 5\%$  inactivation whereas PaMscS-2 showed  $60\pm 3\%$  inactivation, which is about twice what was observed in *E. coli* MscS [132]. In the recovery protocol, after the population was partially inactivated, the conditioning pressure was dropped to zero and the recovery process was monitored with a train of short test pulses over time (Fig. 2.8C, D). The characteristic times ( $\tau$ ) of recovery were  $30\pm 6$  s for PaMscS-1 and  $200\pm 60$  s for PaMscS-2 (0.5 and 3.4 min, respectively). The time required for full recovery after complete inactivation of PaMscS-1 was around 5 min, whereas full recovery of PaMscS-2 took over 10 min.

### **Flexible hinge-like elements in TM3 are responsible for inactivation in PaMscSs**

The alignment of PaMscS-1 and 2 sequences to their *E. coli* ortholog (Fig. S6) suggests that both channels have all elements that were associated with the inactivation process in EcMscS. Homology models indicate the same locations of the

key inactivation elements. These are two flexible hinges at G121, which in EcMscS is responsible for the closing transition, and at G113, which is responsible for inactivation. Interestingly, the G121 hinge is made super-flexible in both PA orthologs by duplicating glycines in that location. We have

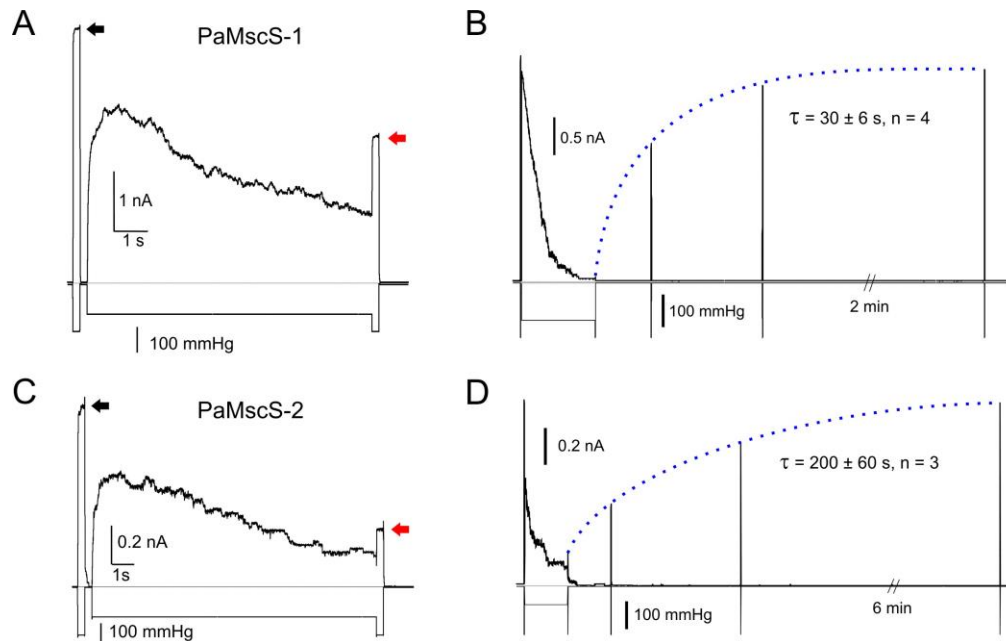


**Figure 2.8. The inactivation and recovery of PaMscS1 and PaMscS2.** Pulse-step-pulse protocols above show that both MscS-like homologues from *P. aeruginosa* inactivate. The degree of inactivation is determined as the ratio of current at the end (red arrow) to the initial test pulse response of full population (black arrow). PaMscS2 displays approximately 60% inactivation, which is more than PaMscS1 and about twice what is seen in its *E. coli* counterpart. The recovery from inactivation for each channel is depicted on the right; PaMscS2 recovers much more slowly than PaMscS1, indicating a more stable inactivated state.

attempted to mutagenize these glycines in both PA channels and found that only PaMscS-1 mutants are expressed at a detectable level. We have tested inactivation in PaMscS-1. The imposition of stronger helicity by the G113A mutation did not interfere with adaptive closure during a 10 s conditioning pulse (to  $p_{0.5}$ ), but reduced

inactivation from 30 to 6±2% (Fig. 2.9A). A replacement of G121 with alanine removed normal adaptation during the sustained moderate stimulus and dramatically slowed down the normal closure of PaMscS-1 (Fig. 2.9B) as was previously observed with EcMscS [49]. At the same time, the G121A mutation did not affect the inactivation in PaMscS-1A (Fig. 2.9C).

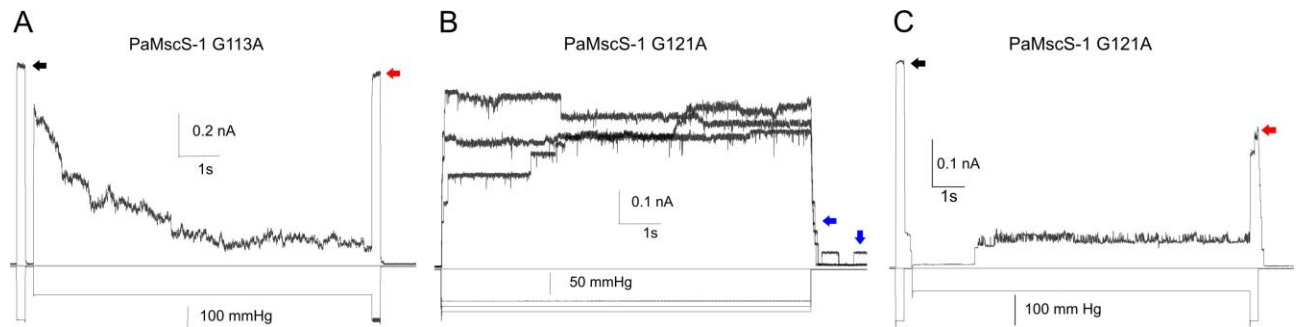


**Figure 2.9. Functional analysis of PaMsc-1 mutants using step protocols shows conservation of elements involved in inactivation between *P. aeruginosa* and *E. coli*.** (A) Pulse-step-pulse experiment shows complete absence of inactivation in G113A mutant, the effect identical to the one previously observed in *E. coli*. (B) The G121A alanine substitution removes adaptation, substantially slows down closing and shows ‘lingering’ activity (blue arrows) indicating that ‘hinge 1’ mediates the process of closing. (C) The G121 substitution does not prevent inactivation. The black and red arrows indicate the initial and end responses to saturating pulses showing the degree of inactivation.

**Table 2.2.** The summary of experimentally determined parameters for the two PaMscS channels in comparison to *E. coli* MscS. The degree of inactivation was measured at saturating pressure after a 10 s conditioning pressure step of amplitude around  $p_{0.5}$ .

Channel	$\Delta E$ (kT)	$\Delta A$ (nm <sup>2</sup> )	$P_{0.5MscS}/P_{0.5MscL}$	Conductance (nS)	Selectivity $P_{Cl}/P_K$	Inactivation (%)	Recovery time, s
<i>E. coli</i> MscS	~20-28 (Akitake et al., 2005)	~12-14 (Akitake et al., 2005; Boer et al., 2011)	$0.58 \pm 0.02$ (n=12)	~ 1-1.1 (Sukharev, 2002)	~1.5 (Sukharev, 2002)	$36 \pm 5$ (n=15)	1.5-3 (Akitake et al., 2005)
Pa MscS-1	$17.1 \pm 0.5$ (n=16)	$11.0 \pm 0.5$ (n=16)	$0.47 \pm 0.01$ (n=4)	$0.96 \pm 0.02$ (n=3)	~1.5 (n=3)	$36 \pm 5$ (n=10)	$30 \pm 6$ (n=4)
Pa MscS-2	$15 \pm 2$ (n=3)	$10 \pm 1$ (n=3)	$0.51 \pm 0.01$ (n=4)	$0.55 \pm 0.02$ (n=3)	~ 4.4 (n=3)	$64 \pm 3$ (n=7)	$200 \pm 70$ (n=3)

## The relative ability of *P. aeruginosa* channels to rescue *E. coli* MJF641 from osmotic down shock.

The electrophysiological characterization of the *P. aeruginosa* channels revealed broad variations in terms of conductivity, inactivation and time needed for full recovery from the inactivated state. This prompted us to investigate the functional requirements that a MS channel should have in order to be a good emergency valve. We heterologously expressed PaMscL, PaMscS-1 and 2 in the channel-free MJF641 strain and monitored their individual contribution to osmotic survival. As long as the osmotic down shock is less than 1000 mOsm both PaMscL and PaMscS-1 were able to rescue the unprotected strain (Figure 2.10). Notably, PaMscS-2 was unable to save MJF641 cells from osmotic down shock regardless of its magnitude.

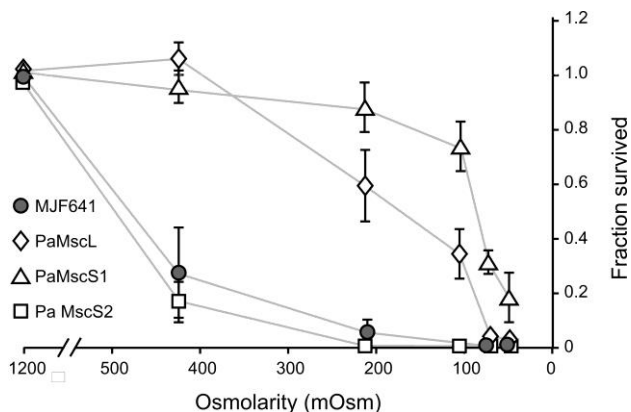


**Figure 2.10. Relative ability of *P. aeruginosa* MS channels to rescue *E. coli* MJF641 from osmotic down shock.** At moderate osmotic down shocks, PaMscL and PaMscS-1 were good at rescuing the MJF641. Surprisingly, PaMscS-2 did not serve as a good emergency valve and the cells displayed poor survival statistically indistinguishable from channel-free MJF641. The plate counts are shown as means with standard deviations, n=8. Christina Mayhew and Deanna Rubin performed and analyzed the survival experiments

## Discussion

In this paper we present the first multi-faceted phenomenological study of the emergency osmolyte release system in wild-type *Pseudomonas aeruginosa* in comparison with *Escherichia coli*. The data reveal the overall kinetics of cell equilibration with the hypoosmotic environment and some information on the

molecular components mediating fast permeability response such as predominant channel types, their densities, conductances, propensities to inactivation and rates of recovery. At the same time, the work outlines a number of unknowns which will be needed for a quantitative model of the mechanosensitive channel-mediated rescuing mechanism.

A better osmotic survival of PA compared to EC under severe down-shocks correlates with a faster osmolyte release process recorded with a stopped-flow technique. The scattering traces (Fig. 2.1) reveal the initial swelling period followed by a falling phase reflecting the process of osmolyte release. The swelling period shortens and the rates of release monotonously grow with the magnitude of downshock in both cultures. Because PA cells are considerably smaller (Fig. 2.2) and have a higher surface area-to-volume ratio, both swelling and release processes in PA are expected to be faster. Indeed they are, but not dramatically. One of the reasons is likely to be lower water permeability of the PA envelope estimated from the up-shock experiments (Fig. 2.2). PA has a phospholipid composition somewhat different from EC [133], which may explain the difference; both species contain aquaporin and glyceroporin genes, but the contributions of these facilitators to the swelling speed are unknown. In any event, lower permeability reduces the influx of water allowing more time for osmolyte release.

The osmotic rescuing mechanism implies that the overall permeability of the tension-activated release system is sufficient to counteract the water influx driven by an abrupt osmotic downshift. As tension builds up, the MscS and MscL channels open gradually and, if water keeps coming in, more channels open and start

dissipating the concentration and pressure gradients faster, thus acting in a negative feedback manner. At high shocks, when all channels are engaged (release rate approaches saturation, Fig. 2.1D), water influx may overwhelm the ‘sieving’ capacity of the channels, and a pressure surge above the limit of the envelope’s mechanical stability would damage the cell. As suggested by traces in Figs. 2.1B and C, the slope and duration of nearly exponential scattering decrease reflect the fraction of channels that are open. Not only does the rate of release increase with the magnitude of shock, but the fraction of released osmolytes also increases, as seen from the total amplitude of the scattering signal and its level at the end. In PA, the release rate steadily increases especially at the highest shocks (Fig. 2.1C). In EC, in contrast, we observe a lower slope of the release rate in that region (a sign of some leveling), suggesting that the total permeability of channel population has reached its capacity, which correlates with the progressive loss of viability (Fig. 2.1A).

To dissect the osmolyte release system in finer detail we devised a procedure for PA giant spheroplast preparation and patch-clamp recording *in situ*. The traces recorded with linear pressure ramps reveal more gradual conductance increase in PA (Figs. 2.4 and S4), with a much smaller fraction of low-threshold MscS-like component compared to EC. Table 2.1 indicates that the relative contributions of MscS and MscL populations are different in EC and PA. While EC uses MscS and MscL in comparable densities, PA relies primarily on its own MscL, which is one third less conductive. The smaller size of PA cells should also be factored into the rescuing mechanism. It has been noted previously that surface-to-volume ratio does play a role in metabolic activity and environmental survival of bacteria [134]. With a



larger S:V ratio, smaller cells may undergo faster swelling, leaving less time for osmolyte ejection and thus making them more vulnerable. On the other hand, by the same token smaller volume can be cleared from permeable substances faster. The smaller cells, due to higher curvature, also have a ‘Laplacian’ advantage of sustaining lower membrane tension at a given pressure gradient. The scaling of swelling and release rates with area and volume still need to be measured and compared with theoretical predictions.

The analysis of PA-14 genome identified one MscL-like and two MscS-like proteins. Four more putative proteins from the MscS family, homologous to *E. coli* MscK, YbdG, YbiO and YjeP were identified, but no obvious homolog of YnaI was found (see Table S1). We cloned PaMscL and the two closest MscS homologs designated as PaMscS-1 and -2. As predicted, PaMscL had a lower unitary conductance (2.1 nS) compared to EcMscL (3.1 nS), possibly due to bulkier sidechains lining its hydrophobic gate and smaller helical tilt. PaMscS-1 was very close to its EC ortholog (36 % identity) in terms of conductance, selectivity and inactivation, however it exhibited longer recovery. PaMscS-2 was characterized with half-conductance of its EC ortholog, considerably stronger anionic selectivity, strong propensity to inactivation and very long (5-6 min) recovery. In EC spheroplasts, PaMscS-2 was functionally expressed at lower level and in osmotic experiments was unable to rescue MJF641 cells.

According to thermodynamic analysis of activation curves (Fig. S5), PaMscS-1 and -2 expand by  $\sim 12 \text{ nm}^2$  in the course of opening transition (Table 2.1). Both channels have a more flexible TM3 helix due to a regular glycine hinge in position

113 and a double-glycine hinge in position 121 (see alignment in Fig. S6). As illustrated in Fig. 2.9, replacing these glycines by alanines in PaMscS-1 removed either adaptation (G121A) or inactivation (G113A), precisely the effects previously observed in EcMscS [49]. The MscS inactivation mechanism therefore is conserved between EC and PA. The mechanism likely proceeds through buckling of the TM3 helix at G121, leading to adaptive closure and then, if tension still persists, subsequent kinking at G113, resulting in complete inactivation [49]. This stronger propensity to inactivation in the low-threshold MscS-like channels in PA does not seem to be an accident. The PA cells are characterized with smaller volume and larger surface-to-volume ratio. If the channels were non-inactivating, moderate near-threshold tensions would prompt these channels to flicker between closed and open states, washing away vital osmolytes. The inactivation mechanism, which disengages the channels at persisting moderate tension, minimizes futile dissipation of vital gradients [53]. We must note that the high-threshold PaMscL did not inactivate when subjected to pulse-step-pulse stimulation protocol (data not shown).

What do we need to know to be able to come up with a quantitative model that would produce the time course of tension in the inner membrane as a function of osmotic shock and predict whether the shocked cell will be rescued or damaged? There are many parameters that are still unknown. The geometric changes of the peptidoglycan layer pre-stretched by constitutive turgor pressure during osmotic cell swelling have not been described yet. Although it is known that many compatible osmolytes and other small molecules leave the cell in the course of osmotic permeability response [103], yet the permeabilities of MscS and MscL to specific

osmolytes have not been reported. It is not clear whether the densities of channels assayed by patch-clamp in giant spheroplasts precisely reflect the densities in unperturbed actively growing cells [95]. Nevertheless, the presented results have moved us one step closer to a better mechanistic understanding of physiological permeability response to osmotic downshock and have given some explanation to higher osmotic stability of environmentally highly adaptable *P. aeruginosa* as compared to enteric *E. coli*.

Acknowledgement. The work was supported by NIH R21AI105655 and GM107652 grants to SS. UC is a U.S. Department of Education GAANN ‘Mathematics in Biology’ Scholar. The authors thank Dr. DJ Black (Bio-Logic Science Instr.) for a custom setup for forward scattering detection, as well as Stephanie Sansbury, Madolyn Britt and Dr. Madhabi Majumdar, for technical assistance and critical reading of the manuscript. The authors have no additional financial interests.

## **Chapter 3: Spatiotemporal relationships defining the adaptive gating of the bacterial mechanosensitive channel MscS**

Uğur Çetiner<sup>1,2,3</sup>, Andriy Anishkin<sup>3</sup> and Sergei Sukharev<sup>1,2,3</sup>

<sup>1</sup>Institute for Physical Science and Technology, <sup>2</sup>Maryland Biophysics Program,

<sup>3</sup>Department of Biology, University of Maryland, College Park, MD 20742

### **Abstract**

Adaptive desensitization and inactivation are common properties of most ion channels and receptors. The mechanosensitive channel of small conductance MscS, which serves as a low-threshold osmolyte release valve in most bacteria, inactivates not from the open, but from the resting state under moderate tensions. This mechanism enables the channel to respond differently to slow tension ramps versus abruptly applied stimuli. In this work, we present a reconstruction of the energy landscape for MscS transitions based on patch current kinetics recorded under special pressure protocols. The data are analyzed with a three- state continuous time Markov model, where the tension-dependent transition rates are governed by Arrhenius-type relations. The analysis provides assignments to the intrinsic opening, closing, inactivation, and recovery rates as well as their tension dependencies. These parameters, which define the spatial (areal) distances between the energy wells and the positions of barriers, describe the tension-dependent distribution of the channel

population between the three states and predict the experimentally observed dynamic pulse and ramp responses. Our solution also provides an analytic expression for the area of the inactivated state in terms of two experimentally accessible parameters: the tension at which inactivation probability is maximized,  $\gamma^*$ , and the midpoint tension for activation,  $\gamma_{0.5}$ . The analysis initially performed on *Escherichia coli* MscS shows its applicability to the recently characterized MscS homolog from *Pseudomonas aeruginosa*. Inactivation appears to be a common property of low-threshold MscS channels, which mediate proper termination of the osmotic permeability response and contribute to the environmental fitness of bacteria.

### **Introduction**

Mechanosensitive (MS) ion channels are found in all domains of life. While in animals they fulfill multiple sensory functions [135–139], in prokaryotes [111], protozoans [140] and plants [141,142] they participate in tension-triggered redistribution of osmolytes to balance osmotic forces in different compartments. In enteric bacteria, which are transmitted between hosts through fresh water and thus are frequently subjected to drastic shifts of external osmolarity, the osmolyte release system is particularly robust. In order to survive an abrupt 750 mOsm downshift causing massive water influx, *E. coli* cells eject most of their small osmolytes (up to 20% of cell's dry weight) within ~50 ms [29]. Smaller bacteria, such as *Pseudomonas aeruginosa*, do it even faster [29]. This massive but fully reversible osmotic permeability response is mediated primarily by two MS channels: the low-threshold 1 nS MscS and the high-threshold 3 nS MscL residing in the inner

membrane [35,42,143]. The five *E. coli* paralogs of MscS encoded by *kefA*, *ybdG*, *ybiO*, *yjeP* and *ynaI* genes are also mechanosensitive channels which are expressed at low-copy levels [91,92]. These minor contributors to the release system noticeably increase osmotic survival only on *mscS*-, *mscL*- background and under slow enough osmotic downshifts [30].

Deletion of both MscS and MscL made bacteria osmotically fragile, whereas re-expression of either of the channels rescued most of the capacity to withstand a 700-900 mOsm sudden downshift [35]. This result led to the assumption that the two channels may be somewhat redundant [34,93,94]. However, the weak ionic selectivity of MscS and the complete lack of ionic selectivity of MscL, as well as differences in conductances and especially in activating midpoint tensions (6 - 8 mN/m for MscS and 12-14 mN/m for MscL) [46], suggest that the channels may not be redundant but rather specialized; their sequential opening may furnish graded responses to a range of osmotic shocks [144,145]. MscS, which gates at non-lytic tensions, may fulfill an “everyday” turgor relief for mild osmotic downshifts, whereas MscL, which opens at near-lytic tensions, should act as a true “emergency” valve. MscL exhibits no inactivation [46]. MscS, in contrast, shows deep desensitization and complete inactivation wherein it enters a non-conductive state that is unable to open by tension [49,51]. Here we specify that desensitization (adaptation) refers to reversible current decline when channels gradually return to the closed state under sustained stimulation. Desensitized channels can be re-activated by a stronger stimulus. Desensitization is most pronounced in excised patches where it is caused in part by tension redistribution between the lipid monolayers. Inactivation of MscS is a

separate process which, like opening is driven by tension and begins from the closed state, but results in a distinct non-conductive and tension-insensitive conformation. The fraction of inactivated channels can be distinguished by applying saturating stimuli which reveal the remaining closed-desensitized channels. Inactivated channels cannot be reopened by increased tension, but they relatively quickly (~2 s) return back to the closed state when tension is released.

While MscS and MscL open sequentially with intracellular pressure increase, at the end of the permeability response the channels are also expected to close sequentially, in reverse order. When tension in the cytoplasmic membrane drops to the threshold for MscL, the large channel closes, but MscS remains open and continues the release until it reduces the tension well below the MscL threshold. When tension approaches the MscS threshold, the channel closes and then inactivates, completely resealing the membrane. The tension threshold is the empirically determined tension that activates the first channel in a population within a given experimental timeframe, below which the probability of finding a channel in the open state is negligible. MscS inactivation appears to exclude spurious flickering of channels at “safe” near-threshold tensions, thus minimizing metabolic losses and assisting in recovery. Inactivation of the channel with the lowest threshold at the end of this sequence appears a final step in the termination of osmotic permeability response.

There have been a number of experimental studies of MscS gating and inactivation that used special pressure protocols to isolate fractions of channels in different non-conductive states [46,51,132,146,147]. It has been shown that both

opening and inactivation are driven by tension from the same closed state, and each of these transitions is accompanied with its own characteristic channel protein expansion in the plane of the membrane [51,53]. The previous experiments were sufficient to suggest a 3-state model for MscS, however, they gave only partial quantitative information, and the kinetic scheme for the entire functional cycle of MscS has never been computed comprehensively.

In this paper, we perform experimental patch-clamp analysis of the MscS kinetics using pressure protocols designed to reveal the rates for the kinetically intertwined closing and inactivation transitions. We then model the MscS kinetic as a finite state continuous-time Markov chain and obtain analytical expressions for the steady state solution. Following the extraction of intrinsic rates and their tension dependencies, we performed time-dependent kinetic simulations using QuB software which reproduced experimental traces obtained with ramp protocols. The model quantitatively explains the ability of MscS to reduce its response to slowly applied stimuli previously described as the “dashpot” behavior [51]. We also show that we can estimate the inactivated state area from a small set of easily accessible experimental parameters. Thus, it is possible to minimize the experimental effort needed to obtain the inactivated state area for sparsely characterized MscS homologs. The parameters extracted using our formalism from the experimental dataset indicate spatial relationships between the energy wells and separating barriers and allow us to reconstruct the energy landscape for the tension-dependent MscS transitions.



## The Model

Previous analysis has shown that the opening and inactivation transitions in MscS both originate from the closed (C) state, thus, the outcome of their competition, i.e. population fractions in the open (O) and inactivated (I) state, is determined by transition rates and their tension dependences (Fig. 3.1). In WT MscS studied in excised patches, the transition from the closed into the inactivated state occurs under moderate tensions, specifically in the range that activates (opens) only a fraction of the population and requires tens of seconds to manifest the inactivation [51,132]. During a quick application of strong stimuli, the channels are distributed primarily between the open and the closed states. In contrast, through a slow or prolonged application of moderate stimuli that keeps the majority of channels closed, the population gradually redistributes into the non-conductive and tension-insensitive inactivated state. This suggests that under certain experimental conditions the two transitions can be described in two separable time scales.

Since both the  $C \rightarrow O$  and  $C \rightarrow I$  rates increase with tension transmitted laterally through the lipid bilayer, each of the transitions is expected to be accompanied by a protein area increase in the plane of the membrane. The scale of area increase from the closed well to the transition barrier defines the slope of the kinetic rate vs. tension, whereas the area increase between the wells would define how the equilibrium partitioning between the wells changes with tension [130,147]. The process with the steepest rate dependence (in this case - the opening) is expected to dominate at high tensions.

The mathematical model consists of a discrete-state continuous time Markov chain where the transition rates are described by the Arrhenius relation and the dynamics satisfy the detailed balance condition. For instance, the transition rates for the closed  $\leftrightarrow$  open transition obey the following relation:  $\frac{k_{OC}}{k_{CO}} = e^{-\beta (E_{Closed} - E_{Open})} e^{-\beta \gamma \Delta A}$ . Thus, in the presence of membrane tension, not only do the states with larger areas become more favorable but also the detailed balance condition guarantees that once the tension is held fixed the system relaxes to a unique equilibrium distribution where the states are populated according to Boltzmann weight [69]. The three-state model does not preclude the existence of some short-lived sub-conducting or hidden Markov states. Its applicability will be tested in experiments described below. For convenience of relating tension with the energetic bias toward lateral expansion, the membrane tension here is mostly presented in units of  $k_B T / \text{nm}^2$ , which equals to 4.114 mN/m at room temperature (298K).

### **Experimental electrophysiological recordings and data treatment**

The WT *E. coli* MscS was the primary object for patch-clamp recording. Additionally, the *P. aeruginosa* MscS-1 channel, the recently cloned close homolog of *E. coli* MscS [29], was used for comparison. Both MscS homologs were expressed from the pB10d vector under the PlacUV5 inducible promoter [125] in the MJF641 strain devoid of seven endogenous MS channel genes ( $\Delta mscL$ , *mscS*, *mscK*, *ybdG*, *ynaI*, *ybiO* and *yjeP*) [91]. Giant *E. coli* spheroplasts heterologously expressing the channels were generated with a standard method as described previously [40,51]. Borosilicate glass (Drummond 2-000-100) pipets 1-1.3  $\mu\text{m}$  in diameter were used to

form tight seals with the inner membrane. The MS channel activities were recorded via inside-out excised patch clamp method after expressing them in MJF641. The pipette solution had 200 mM KCl, 50 mM MgCl<sub>2</sub>, 5 mM CaCl<sub>2</sub>, 5 mM HEPES, pH of 7.4. The bath solution differed only in the addition of 400 mM Sucrose. Traces were recorded using the Clampex 10.3 software (MDS Analytical Technologies). Mechanical stimuli were delivered using a modified high-speed pressure clamp apparatus (HSPC-1; ALA Scientific Instruments). Current data were analyzed after the series resistance (R<sub>s</sub>) correction of the traces by the equation,  $G_p = I / (V - IR_s)$ , where G<sub>p</sub> is the patch conductance and V and I are the transmembrane voltage and current, respectively. R<sub>s</sub> is the intrinsic resistance of the patch free pipette (1.2-2 MΩ). The pressure (P) was converted to tension (γ) using the following relation:  $\gamma = (P/P_{0.5})\gamma_{0.5}$  assuming the radius of curvature of the patch does not change in the range of pressures where the channels were active and the constant of proportionality between tension and pressure was taken to be  $\gamma_{0.5}/P_{0.5}$  [130]. The midpoint tension  $\gamma_{0.5}$  of MscS was taken to be 7.85 mN/m [46] and the midpoint tension of PaMscS-1 activation in *E. coli* spheroplasts was determined to be 5.6 mN/m using *E. coli* MscL as an intrinsic tension gauge [29]. P<sub>0.5</sub> values that correspond to pressure at which half of the population is in the open state were determined using 1-s triangular ramp protocols.

### **Estimation of the in-plane area for crystallographic structures and molecular models.**

Crystallographic structures of *E. coli* MscS with PDB IDs 2OAU and 2VV5 were chosen as representatives of non-conductive and conductive states, respectively.

For comparison, we have also considered our published models of MscS in the putative resting, open, and inactivated conformations [50,148]. Since in some conformations MscS features deep crevices between TM1-TM2 helices comparable to a lipid molecule in size, the accessible area becomes sensitive to variation in orientation of the protein side chains, which might differ in crystal structures and in real membranes. To avoid potentially artefactual fluctuations in area estimates due to variability of the side chain orientation, we performed our area estimates based on the positions of the backbone only under the simplifying assumption that the thickness of the side chain shell around the backbone is uniformly 5 Å. This thickness was calculated from our analysis of all-atom solvent-accessible surface of all included MscS structures. The atomic radii of the backbone were set to 5 Å, and the solvent-accessible area of the “smoothed” backbone structures was estimated using a spherical probe of 2 Å radius (approximate VDW radius of an aliphatic carbon in CHARMM36m force field [149]). The calculations of the lateral area profile along the channel axis and visualization of the structures were performed using custom-written Tcl scripts in VMD [150].

## **Results**

In this section, we first describe the kinetic scheme and obtain some analytical solutions for the steady state MscS behavior from the three-state model. Next, we present the main experimental observations followed by the thermodynamic and

kinetic treatment of the system. Following this, we summarize the kinetic and spatial parameters extracted from the data and then finally simulate the responses and compare them with experimental traces to confirm the quality of the model and compare spatial estimates with information available from crystallographic structures and structural models.

**The three-state continuous time Markov chain model.** Fig. 3.1 presents the kinetic scheme of the MscS functional cycle. The unperturbed channel resides in its native environment in the compact closed (resting) state. From that state, the channel undergoes two separate tension-driven transitions into the open ( $C \rightarrow O$ ) or inactivated ( $C \rightarrow I$ ) states. Note that the O and I states are not interconnected, meaning that open channels do not inactivate [132], (See Supplementary Fig S2). The energy wells for the connected states are assumed to be separated by single rate-limiting barriers and the transition rates between the states are governed by the Arrhenius-type relation:  $k_{XY} = k_{XY}^0 \exp(\beta\gamma\Delta A_{Xb})$  where  $k_{XY}^0$  is the intrinsic rate (frequency) of the system's attempts to overcome the barrier between states X and Y in the absence of tension [151]. The exponential term includes  $\Delta A_{Xb}$ , the expansion area from the bottom of the well of the particular state, X, to the top of the barrier that separates the states X and Y,  $\gamma$ , is the applied tension, and  $\beta=1/k_B T$  where  $k_B$  is the Boltzmann constant and T is the temperature. Thus, tension favors states with larger area.

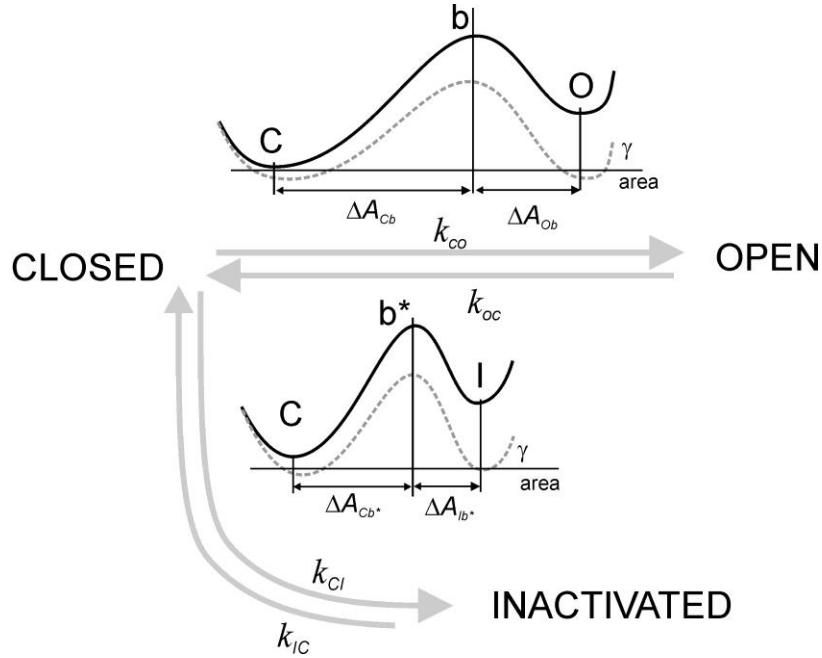


**Figure 3.1. The discrete conformational state space of allowed transitions indicated by the experiments.** The free energy difference between the states decreases linearly with the work done by the tension,  $\gamma\Delta A$ , favoring the states with larger in-plane area (A) of the transmembrane domain (TMD). The transition rates between the states are governed by an Arrhenius type of relation displaying exponential dependence on the membrane tension. The barriers that separate the open and inactivated states from the closed state are denoted by b and b\*, respectively.

In this kinetic framework, when the tension is kept constant, the master equation can be written as follows:

$$\frac{dC}{dt} = C(-k_{CO} - k_{CI}) + Ok_{OC} + Ik_{IC}$$

$$\frac{dO}{dt} = Ck_{CO} - Ok_{OC}$$

$$\frac{dI}{dt} = Ck_{CI} - Ik_{IC} \quad [1]$$

Or in a more compact form:

$$\frac{d\vec{p}}{dt} = R\vec{p} \rightarrow \vec{p}(t) = e^{Rt}\vec{p}(0) \quad [2]$$

where  $\vec{p}$  is the probability vector and R is the transition rate matrix specified as:

$$\vec{p} = \begin{pmatrix} C \\ O \\ I \end{pmatrix} \text{ and } R = \begin{pmatrix} -k_{CO} - k_{CI} & k_{OC} & k_{IC} \\ k_{CO} & -k_{OC} & 0 \\ k_{CI} & 0 & -k_{IC} \end{pmatrix} \quad [3]$$

The equilibrium distribution of the chain of conformational states can be obtained in several ways. Perhaps the simplest is to set  $\frac{d\vec{p}}{dt} = \mathbf{0}$  as a stationary solution and solve a system of linear equations. Another way is to use the exponential form for the probability vector [152,153], which can be written as:

$\vec{p}(t) = c_1 e^{\lambda_1 t} u_1 + c_2 e^{\lambda_2 t} u_2 + c_3 e^{\lambda_3 t} u_3$ , where  $\lambda_1, \lambda_2, \lambda_3$  are the distinct eigenvalues of  $R$  and  $u_1, u_2, u_3$  are the corresponding right eigenvectors. The Perron–Frobenius theorem then guarantees that there is going to be a unique invariant distribution,  $\boldsymbol{\pi}$ , that can be expressed as:  $\lim_{t \rightarrow \infty} e^{Rt} \vec{p}(0)$ . A detailed discussion on the Perron–Frobenius theorem for primitive matrices, convergence and uniqueness for a finite state, and irreducible Markov chains is included in the supplementary information [154].

The equilibrium distribution of the inactivated state probability is given by the following equation:

$$\pi_I = \frac{1}{1 + \frac{k_{IC}}{k_{CI}} + \frac{k_{IC} k_{CO}}{k_{CI} k_{OC}}} \quad [4]$$

By plugging in the relations for the transition rates, we obtain:

$$\pi_I = \frac{1}{1 + \frac{k_{IC}^0}{k_{CI}^0} e^{-\beta\gamma A_{inactivated}} + \frac{k_{IC}^0}{k_{CI}^0} e^{-\beta\gamma A_{inactivated}} \frac{k_{CO}^0}{k_{OC}^0} e^{\beta\gamma A_{open}}} \quad [5]$$

Here  $A_{Inactivated} = \Delta A_{Ib^*} + \Delta A_{Cb^*}$  and  $A_{Open} = \Delta A_{Cb} + \Delta A_{Ob}$  represent the total in-plane area expansion associated with inactivation and opening, respectively, assuming there is a single barrier separating the states. Since low-tension values favor the closed state and high-tension values lock the system in the open state with no transition to the inactivated state, we assume there is an optimum intermediate tension that simultaneously allows for a sufficient fraction of channels to be left in the closed state and yet also provides enough driving force to maximize the probability of inactivation. In the following analysis, we determine the tension  $\gamma^*$  that gives the maximum for inactivated state probability by solving the system under the  $\frac{d\pi_I}{d\gamma} = 0$  condition. As detailed in the supplement, the exact expression for the tension at which the probability of inactivation reaches its maximum is given by:

$$\gamma^* = \gamma_{0.5} + \beta^{-1} A_{Open}^{-1} \ln \frac{A_{Inactivated}}{A_{Open} - A_{Inactivated}} \quad [6]$$

Here  $\gamma_{0.5}$  is the tension at which the probability of finding a channel in the open state is 0.5. This expression, therefore, relates the tension that results in the highest degree of inactivation with the half-activating tension. This expression can be rewritten in terms of the inactivated state area,  $A_{Inactivated}$ , which reflects the in-plane expansion of the channel protein associated with the inactivation transition,

$$A_{Inactivated} = A_{Open} \left( \frac{e^{\beta A_{Open}(\gamma^* - \gamma_{0.5})}}{1 + e^{\beta A_{Open}(\gamma^* - \gamma_{0.5})}} \right) \quad [7]$$

As was reported previously,  $A_{Inactivated}$  is of prime mechanistic interest because it may reflect the de-coupling of the peripheral helices from the gate [45,49]. However, it is not an easily accessible parameter [132]. Having this relationship we



now see that  $A_{Open}$ ,  $\gamma^*$ ,  $\gamma_{0.5}$  are easier to obtain, thus the area of the inactivated state can be found using the expression [7] without a need for more experimental parameters.

**The experimental time scales for  $C \leftrightarrow O$  and  $C \leftrightarrow I$  transitions.** As shown on the kinetic scheme (Fig. 3.1), the transitions between C and O and C and I states are governed by different barriers and therefore the equilibration upon stimulus application may take different times. We adopted the previous strategy of recording the transition with either ramps or prolonged steps while controlling the active fraction of the population with short saturating test pressure pulses, before, after, and in some cases during extended stimulation. Fig. 3.2 shows MscS population responses under stimuli applied in two different time scales. Panel A shows a response to a pulse-ramp-pulse sequence, where two 0.2 s saturating test pulses flank a 2-s symmetric ramp (1-s ascending and 1-s descending limbs). The bell-shaped ramp response is visibly asymmetric showing slight hysteresis at this ramp rate. The test pulse responses before and after the ramp are identical within 2% showing that during this (~3 s) protocol there is no outflow of channels into the inactivated state ( $n=5$ ). Panel B shows responses to 1 s steps of different amplitudes with identical test pulses before and after. The trajectories illustrate the MscS closing rates at different tensions, and again, the comparison of test pulse responses shows no inactivation in this time scale. More prolonged steps of 90 and 120 s of tension (shown in panel C) lead to substantial inactivation. Furthermore, the comparison of time courses shows that the equilibrium distribution of the population between C, O and I states is

reached within about 90 s, after which the occupancies become time-independent under these conditions (compare with 120 s step).

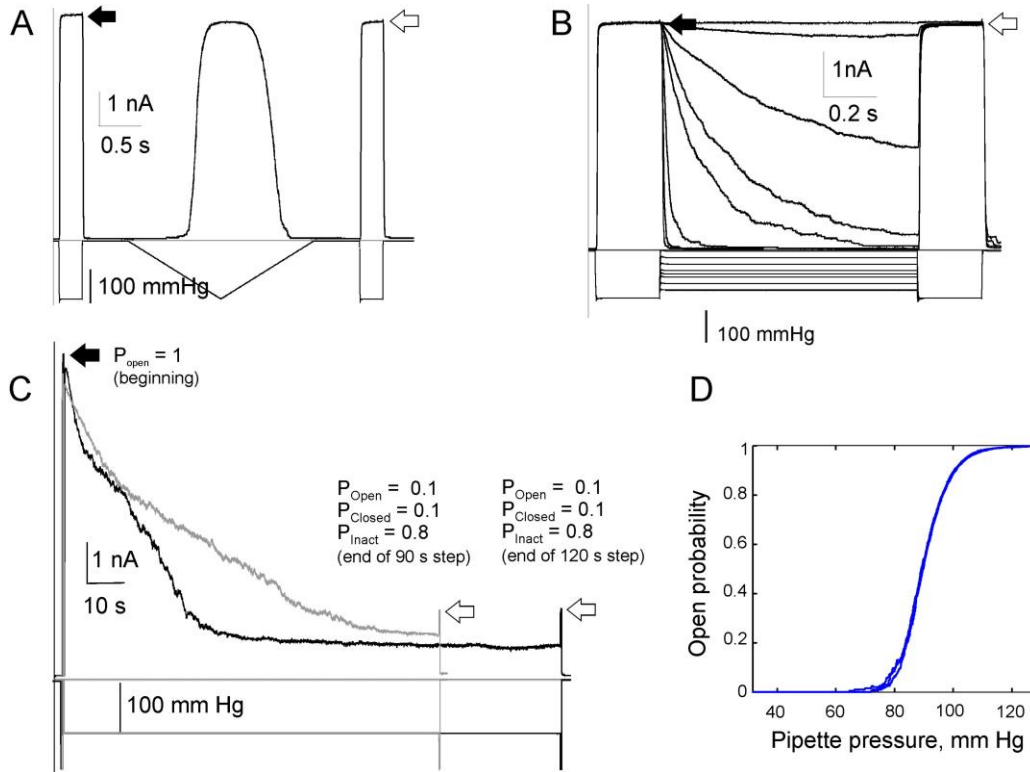


**Figure 3.2. Exploration of time scales characteristic for the separate  $C \leftrightarrow O$  and  $C \leftrightarrow I$  transitions in MscS populations.** The black and white arrows indicate maximal amplitudes of population current (i.e. the number of non-inactivated channels) before and after the ramp or step stimulation, respectively. The difference between the current amplitudes reflects the degree of inactivation for each protocol. **(A)** Current responses to a short pulse-ramp-pulse stimulus. **(B)** Responses to a series of short (1s) pulse-step-pulse stimuli. Application of quick ramp or pulse protocols does not induce any inactivation thus MscS can be well modeled as a two state (closed - open) system. **(C)** Superimposed 90s and 120 s pulse-step-pulse experiments showing that a 90 s step is sufficient for reaching equilibrium between the C, O and I states, meaning that the occupation probabilities for each state,  $P_{Open}$ ,  $P_{Closed}$ ,  $P_{Inactivated}$  stay constant after 90 s. **(D)** A demonstration of patch stability for a single representative experiment. Control ramp experiments before, in between, and after 90 or 120s experiments illustrating a good superimposition of three activation curves and intactness of the patch excluding slippage inside the pipette.

Based on traces presented in Fig. 3.2, we picked 120s as the time required for the chain to reach equilibrium. It should be noted that when subjected prolonged steps of tension, patches often become unstable and either rupture or undergo slippage inside the glass pipette, which changes the patch geometry. This may introduce errors in probability measurements. To avoid these errors, we employed 1s triangular ramps and recorded the dose response curves throughout the experiment (Fig. 3.2D) and checked whether the open probability stays within the limits of stochasticity of the experiment and does not drift as a result of changes in membrane curvature.

**Characterization of Closed $\leftrightarrow$ Open transitions.** As illustrated in Fig. S1, Fig. 3.2A and B, inactivation is a relatively slow process. The amount of inactivation becomes noticeable in a specific range of tensions applied for periods longer than 5-10 seconds, whereas application of quick ramp or pulse protocols (Fig. 3.2A, B) causes no inactivation (n=5) but is sufficient to activate the channel. With the clear separation of time scales for the two competing transitions originating from the closed state, the system subjected to 1-2 s stimuli can be approximated by a two-state model [132,147,155]. The closed  $\leftrightarrow$  open branch was probed by a relatively quick 1-s triangular ramp protocol where the tension in the membrane was increased linearly from zero to saturating tension driving all channels to the open state. The response to the symmetric 1-s ramp is shown in Fig. 3.3A, with the ascending (increase of tension, channel opening) and descending branches (decrease of tension, channel closure) and a plateau in the middle reflecting response saturation at high tensions. When tension increases linearly as a fast ramp, the rate of accumulation of open channels can be presented in the form:

$$\frac{dO}{dt} = (1 - O)k_{CO} \text{ [8]}$$

And on the descending leg of dose response curve can be written as:

$$\frac{dO}{dt} = -Ok_{OC} \text{ [9]}$$

Here we use a simplifying assumption that the rate of closing ( $k_{OC}$ ) on the ascending limb and the rate of opening ( $k_{CO}$ ) on the descending limb are small. To verify this assumption, in Fig. 3.3A we provided a typical ramp response of a small channel population where each individual transition is clearly seen. Panel B shows the histogram of the number of closure events compared to the number of openings on the ascending leg of the trace as the tension was quickly increased in a linear fashion. The closing events during tension increase can be considered rare events thus verifying the negligibility of  $k_{OC}$ . Similar reasoning applies to  $k_{CO}$  on the descending leg of the dose response. Obviously, only during the quick ramp protocols (<1 s), the channels make primarily one-way transitions either from the closed to open or from the open to closed state.

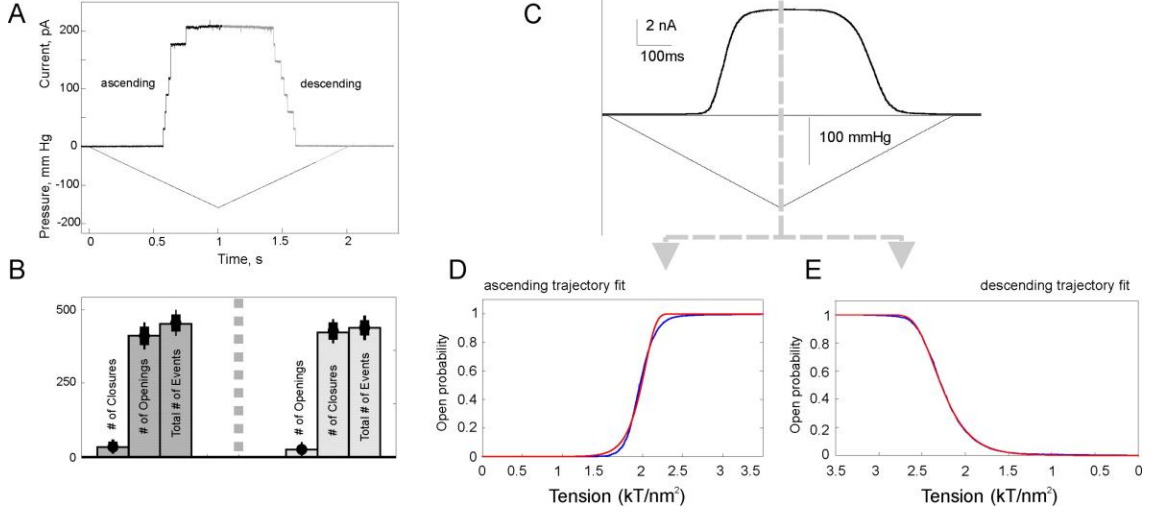


**Figure 3.3. MscS responses to triangular pressure ramps.** (A) A ramp response of a small MscS population (7 channels) where individual opening and closing events are seen. (B) Statistics of opening and closing events observed over 20 sequential ramp experiments on several small-population patches. The observed probabilities of closing events during the opening phase and opening events during the closure phase are very low ( $n=3$ ). For this reason, these transitions can be described with a unidirectional kinetics (Eqns. 8 and 9). (C) A response of large ( $\sim 200$  channel) population to a symmetric 1-s triangular ramp. Each leg on the ramp response, ascending (D) and descending (E) represents a separate experimental dose-response curve (blue), which could be fit (red curves) separately. The probabilities of the open and closed states can be described by the equations [10, 11] assuming that  $k_{OC}$  and  $k_{CO}$  are negligible on ascending and descending limbs of the fast ramp protocol respectively [156]. The gating parameters extracted from the fits are listed in Table 1 ( $n=5$ ).

Fig. 3.3C shows a typical 1-s ramp response of a larger ( $\sim 200$ ) population of channels which now looks like a smooth curve. To fit the ascending and descending segments of the trace presented in panels D and E we used the solution to the equation [8], which can be written as [156]:

$$O(\gamma) = 1 - e^{-\frac{k_{CO}^0}{\beta r \Delta A_{Cb}} (e^{\beta \gamma \Delta A_{Cb}} - 1)} \quad [10]$$

And the closed state probability on the descending leg is given by:

$$C(\gamma) = 1 - e^{-\frac{k_{OC}^0}{\beta r \Delta A_{Ob}} (e^{-\beta \gamma \max \Delta A_{Ob}} - e^{-\beta \gamma \Delta A_{Ob}})} \quad [11]$$

Curves fitting Eqn [10] and Eqn [11] to the ascending and descending legs of the experimental dose-response curve (Fig. 3.3D, E red lines) produced parameters for the closed $\leftrightarrow$ open transition now listed in Table 3.1.

As a second way of getting the gating parameters for the open  $\rightarrow$  closed transition, we employed the previously described pulse-step experimental protocol [146,155] where the tension is first delivered as a short saturating pulse to pre-condition the entire channel population to the open state and then is changed to various sub-saturating levels as illustrated in Fig. 3.4A. The kinetics of closure is monitored as a function of tension and time. The experiment directly (Fig. 3.4A) reveals the closing rate,  $k_{OC}$ . Once the logarithm of the rate obtained from the mono-exponential fits of the initial segments of the decaying current traces is plotted against membrane tension, its slope provides information about the  $\Delta A$  between the open well and the rate-limiting barrier, and the y intercept gives the logarithm of the intrinsic closing rate in the absence of tension. This rate might reflect the attempt rate (pre-exponential frequency factor) associated with the transition, as well as the height of the energy barrier. The transition state area (barrier position) and the attempt frequency in the absence of the tension that were captured from the semi-log plot in Fig. 3.4B (n=9) were in good agreement with the values extracted from the fit of Eqn [11] to the descending leg of dose response curve as explained in Table 3.1.

We should note that the eqn [10] does not describe the ascending leg as precisely as eqn [9] describes the descending leg. Even though the vast majority of channels do not close back on the ascending leg (31 downward events out of 469), even a small  $k_{OC}$ , obviously more pronounced at low tensions, may still introduce an

error in the fitting of the dose-response curve sharply rising with tension (eqn [10]).

The measurement of the Open  $\rightarrow$  Closed transition rate  $k_{OC}$  on the descending leg is in part duplicated by the pulse-step experiments (Fig. 3.4) directly visualizing the

closing kinetics. Ideally it would be desirable to apply the second method and

measure directly the kinetics of the Closed  $\rightarrow$  Open transition in step experiments.

Unfortunately, with the pressure step increase, the opening rate of MscS soon

becomes too fast to be resolved with the pressure clamp apparatus whose rising time

for a 100-mmHg step is around 10-15 ms.

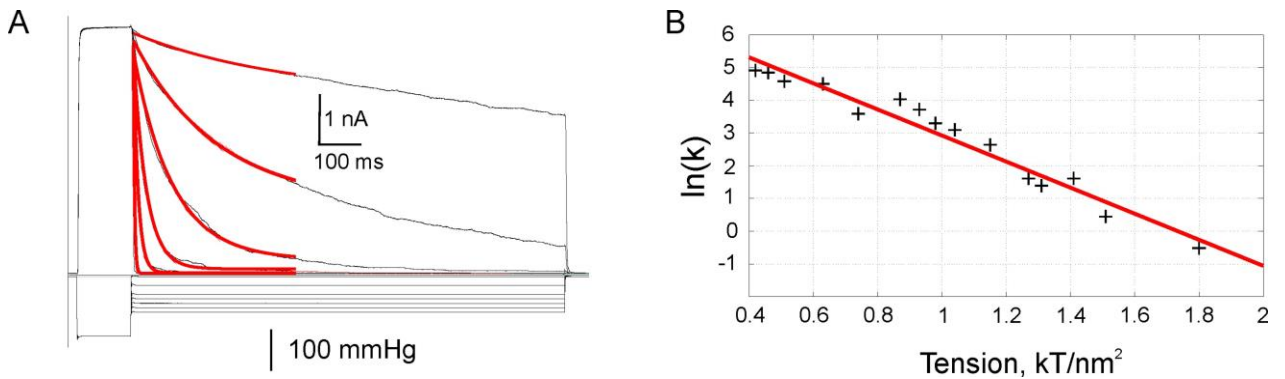


**Figure 3.4. Probing the Open  $\rightarrow$  Closed transition by the pulse-step protocol.** (A) The kinetics of the channels pre-conditioned in the open state by the saturating pulse relaxing to the closed state (black line) was monitored as a function of tension for 2s and fitted by the mono exponential function (red line) to extract the rates. (B) The semi-logarithmic plot of the closing rate as a function of tension. The slope gives an estimate of the areal distance from the bottom of the open-state well to the rate-limiting barrier. The y-intercept suggests the intrinsic closing rate in the absence of tension. The area expansion from the open state to the barrier,  $\Delta A_{Ob}$ , and transition rate in the absence of tension,  $k_{OC}^0$ , were estimated to be  $5.4 nm^2$  and  $9800 (s^{-1})$  respectively (n=9).

**Closed  $\leftrightarrow$  Inactivated Transitions.** The gating parameters of the inactivation

(C  $\rightarrow$  I) and the reverse (I  $\rightarrow$  C) transitions were recaptured by utilizing multi-step

pressure protocols previously described in [132,146]. The initial short saturating

pulse preconditions all the channels in the open state and measures the total number

of active channels in the membrane. The tension is then switched to a sub-saturating level for 60 s allowing the system to transition between the states and to relax toward to the equilibrium distribution determined by tension (Fig. 3.5A). As the channels pass from the open state through the closed state to the inactivated state ( $O \rightarrow C \rightarrow I$ ), their distribution was periodically monitored by short saturating pulses interspersed evenly from the beginning to the end enabling us to see the remaining active population. The fraction of the population in each state is deduced using the normalization condition,  $P_{Open} + P_{Closed} + P_{Inactivated} = 1$ . The log of  $k_{CI}$ , which was obtained by fitting the analytic solutions for the model ( $O \xrightarrow{k_{OC}} C \xrightarrow{k_{CI}} I$ ) to the experimental traces, was plotted as a function of tension (Fig. 3.5B). This gives the area from the closed state well to the barrier that separates it from the inactivated state and the logarithm of the intrinsic transition rate in the absence of tension (Table 3.1, n=5). We note that the analytical solution obtained in [132] expresses the channel population as a function of time that converges to the steady state solution in the long-time limit. Therefore, the system does not have to reach the ultimate equilibrium as we extract the rate constants from the time-dependent changes in the occupancies of the closed, open, and inactivated states, tracked using the kinetic scheme in Fig. 3.5A. The total duration of protocol (60s) was sufficiently long to monitor the inactivation process as a function of time with interspersed saturating pressure pulses.

The recovery transition ( $I \rightarrow C$ ) was studied by the protocol previously reported by [51,132]. The channel population is first probed by a short test pulse and then kept at  $\gamma^*$  to maximize inactivation until almost all channels are driven into the



inactivated state. After conditioning the channels in the inactivated state at  $\gamma^*$ , tension was decreased to zero or to an intermediate level between 0 and  $\gamma^*$ , and the rate of MscS transition to the closed state was monitored by applying an extended train of short saturating pulses (Fig. 3.5C). Since the inactivated state cannot open in response to tension, only the channels in the closed state can be activated by tension. Thus, by employing saturating pulses, the recovery transition can be monitored over time. The recovery rate from inactivation slowed down with an increase in the membrane tension as indicated by the red, blue, green and black arrows in Fig 3.5C, where red arrows show the fastest recovery in the absence of membrane tension. The log of the rates obtained from single exponential fits to data (not shown) was plotted as a function of tension as reported in [132] (Fig 3.5D). The complete set of transition parameters obtained from the slopes and the y intercepts is listed in Table 3.1 (n=5).

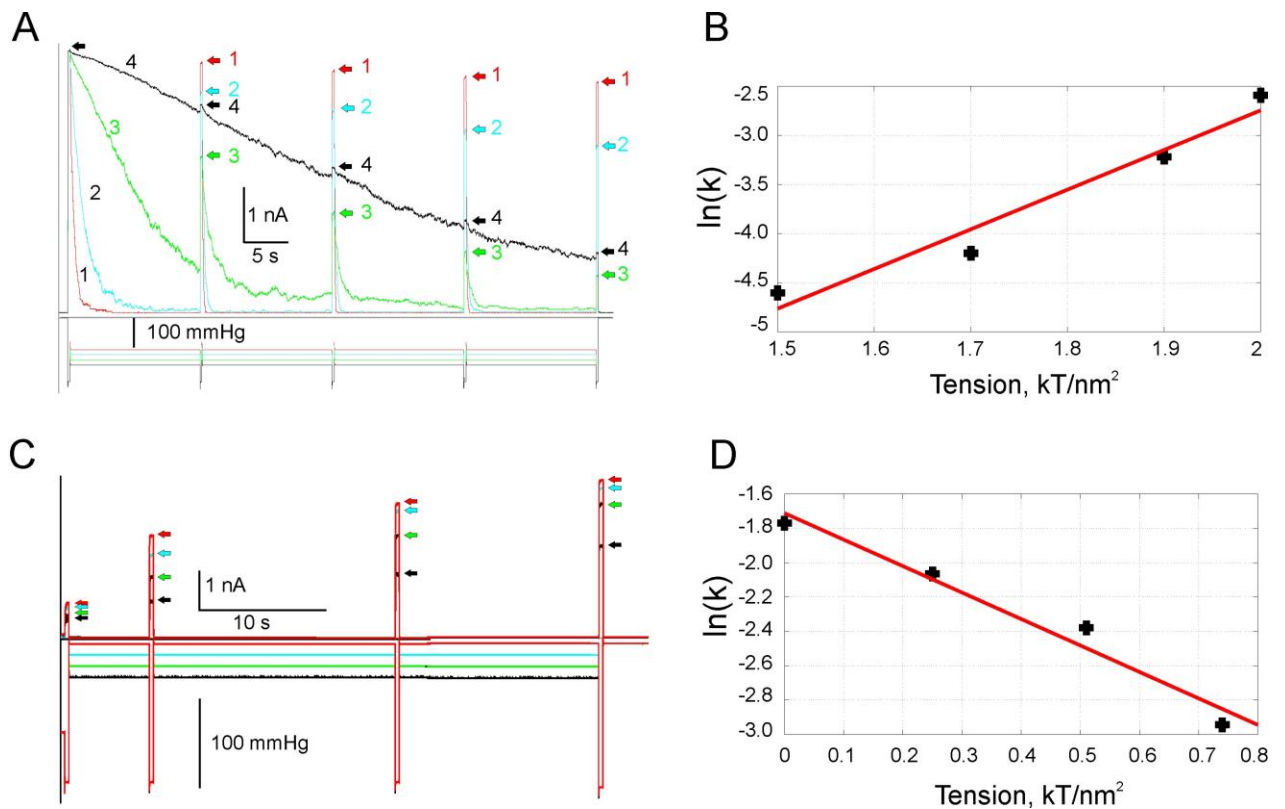


**Figure 3.5. Probing the Closed ↔ Inactivated transition.** (A) The channels were kept at sub-saturating tensions for 60s, allowing enough time for inactivation to manifest. The number of channels populated in different states was checked by interspersed saturating pressure pulses that demonstrate the distribution of the channels between the states based on the fact that only the channels in the closed state could be activated with tension and the number of the channels in the membrane was constant. With this protocol, as shown in [132], channels' transitions can be described by the following scheme:  $(O \xrightarrow{k_{OC}} C \xrightarrow{k_{CI}} I)$  from which rate of the inactivation,  $k_{CI}$ , was obtained by fitting analytic solutions to experimental data. (C) MscS recovery from inactivation is retarded by the membrane tension. Channels were driven to inactivation by a 60-s saturating tension and the extent of recovery from inactivated state was tested by four saturating test pulses applied at different time points for various tension values. The recovery traces were fitted with mono-exponential functions (not shown). (B and D) The semi-log plots of the rates obtained by single exponential fit to data revealed the area expansion and transition rate in the absence of tension associated with the relevant transition. All parameters are listed in Table 3.1 with experimental uncertainties.

**Table 3.1.** The energy profiles for MscS transitions were tested experimentally and compared with values from literature. For the  $O \rightarrow C$  transition, the area expansion from the open state to the barrier,  $\Delta A_{Ob}$ , and transition rate in the absence of tension,  $k_{OC}^0$ , were estimated to be  $5.4 \text{ nm}^2$  and  $9800 \text{ (s}^{-1}\text{)}$  respectively based on the semi logarithmic plot of the rates as a function of tension as show in Fig. 3.4B ( $n=9$ ). These values are in a good agreement with the results obtained by applying the fitting eqn [11] to the descending leg of dose response curve

(n=5). In the second column, the  $\Delta A$  values represent the magnitude of areal distances between the bottoms of the corresponding state wells to the rate-limiting barriers denoted as  $b$  and  $b^*$ , respectively.

Transition (X $\rightarrow$ Y)	$ \Delta A_{X \rightarrow b, b^*} $ (nm <sup>2</sup> )	Literature value (nm <sup>2</sup> )	$k_{XY}^0$ (s <sup>-1</sup> )	Literature value (s <sup>-1</sup> )
C $\rightarrow$ O	6 $\pm$ 1 (n=5)	$\sim 11$ <sup>147</sup>	4e-6 (n=5)	7e - 6 <sup>147</sup>
O $\rightarrow$ C	5 $\pm$ 1 (n=5)	3.8 <sup>155</sup> , 4.3 <sup>53</sup> , $\sim 4.8$ <sup>147</sup>	1e+4 (n=5)	2700 <sup>147</sup> 2430 <sup>200</sup>
C $\rightarrow$ I	5 $\pm$ 1 (n=5)	4.6 <sup>132</sup>	2e-5 (n=5)	None
I $\rightarrow$ C	1.2 $\pm$ 0.5 (n=3)	2.6 <sup>132</sup>	0.18 (n=3)	None

### Opening and Inactivation of MscS in steady-state and kinetic regimes

**validate the model.** Having the kinetic and spatial parameters for the two reversible transitions at hand, we proceeded to test them in experiments under either prolonged ‘‘static’’ mechanical perturbations allowing the system to reach equilibrium under a constant tension, or in a dynamic regime under tension ramps applied with different speeds. The first set was designed to compare our analytic results obtained from the steady state solution of the model with the experiments where patches were exposed to 120 s conditioning steps required for the chain to reach equilibrium as shown in Fig. 3.2C. In Fig. 3.6, we present the experimental fraction of inactivated channels at the end of a 120 s step shown as black circles with error bars. The data were obtained from 8 independent stable patches from 3 different spheroplast preparations. The red

curve was computed by plugging the parameters listed in Table 3.1 into eqn [4] predicting the steady state inactivation, and the blue curve, which was obtained under 1 s ramp protocol, represents the open probability of the channel on which  $\gamma_{0.5}$  is marked with a blue circle. Eqn [4] well reproduces the experimentally observed fraction of MscS inactivation as a function of conditioning tension magnitude.

As previously mentioned, MscS inactivation takes place in a specific range of tensions, and the value of  $\gamma^*$  which produces the maximum inactivation is predicted by eqn [6] carrying information about the in-plane area of the inactivated state relative to the area of the open state on the reaction coordinate. The  $\gamma^*$  for MscS was calculated to be  $2.0 \pm 0.1 \text{ k}_B\text{T}/\text{nm}^2$  by evaluating eqn [6] with the parameters listed in Table 3.1 and marked with a red circle on Fig. 3.6, showing a good agreement with the experimental data.

This framework encapsulated in eqn. [7] can be used to determine the inactivated state expansion area for yet unexplored MscS homologs that also show tension-dependent inactivation, but were not subjected to test protocols depicted in Fig. 3.5. In order to illustrate the utility of eqn [7], we calculated the inactivated state expansion area of a newly characterized MscS homolog from *Pseudomonas aeruginosa*, PaMscS-1, which also inactivates with tension [29]. Fig. 3.7 shows the activation curve for PaMscS-1 obtained with a 1 s ramp protocol. This  $P_{\text{Open}}$  versus tension curve (blue line) indicates the midpoint position  $\gamma_{0.5}$  for the channel. Independently but on the same patch, the tension that maximizes the inactivated fraction,  $\gamma^*$ , was determined using 10 s pulse-step-pulse protocol. By plugging in the

experimental values for the two parameters into eqn [7], the inactivated state expansion area of PaMscS-1,  $A_{Inactivated}$ , can be estimated as  $5 \pm 1 \text{ nm}^2$ . This value is comparable with  $6 \pm 1 \text{ nm}^2$  for EcMscS. Note that even though a closed-form expression for  $\gamma^*$  is available for the steady state solution, it is the same tension that maximizes the inactivation at any intermediate time (See Supplementary Fig. S3). Despite the fact that *E. coli* MscS and *P. aeruginosa* MscS-1 share only 36 % identity, the close inactivation area parameters may suggest a similarity in their inactivation mechanisms, which presumably proceed through the uncoupling of the lipid-facing helices from the gate [45,49]. We hypothesize that MscS inactivation plays an important general role in bacterial osmoregulation which will be explained in the Discussion.

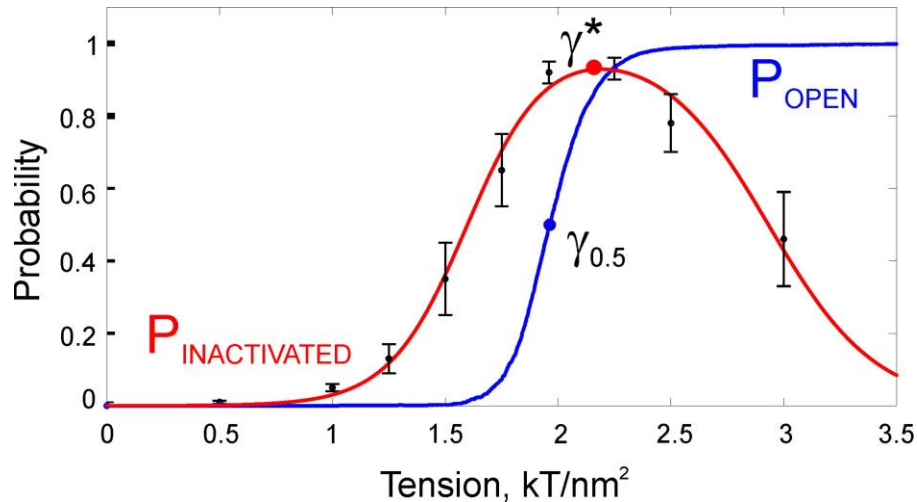


**Figure 3.6. Comparison of experimental steady state MscS inactivation with 3-state model.** The black data points with the error bars represent steady state MscS inactivation in the course of a 120 s conditioning step as in Fig. 2C, averaged over 8 independent patches. The red curve represents the steady solution of the model eqn [4] evaluated with the parameters listed in Table 3.1, which passes through the experimental points (black). The red circle is the tension at which the steady-state inactivation is maximized,  $\gamma^*$ , predicted by the model, eqn [6], after plugging in the corresponding values in Table 1. The blue curve is the open probability for the fast activation of channels under 1s ramp protocol on which the midpoint,  $\gamma_{0.5}$ , is marked as blue circle. Note that under short (1 s) stimulation, MscS

channels are mainly distributed between the closed and open state, thus the blue curve essentially represents the open probability for the two-state (C-O) system.

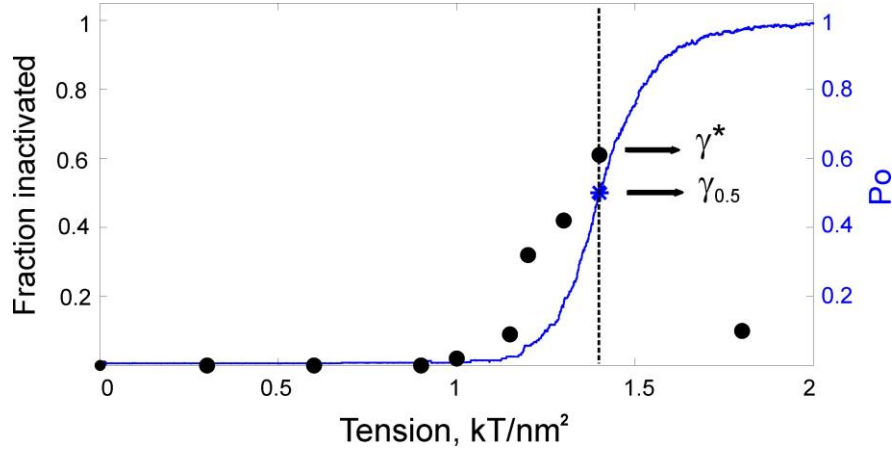


**Figure 3.7. The spatial scale for inactivation in *Pseudomonas aeruginosa* PaMscS-1.** Eqn [7] can be used to determine the inactivated state area of other MscS homologs without employing complicated experimental protocols described in Fig. 3.5. The midpoint tension (blue circle),  $\gamma_{0.5}$  and the tension that leads to maximum inactivation,  $\gamma^*$ , were determined experimentally by application of fast 1 s ramp and 10 s pulse-step-pulse protocols, respectively. Given that the open area of PaMscS-1 is  $11 \pm 0.5 \text{ nm}^2$  [29], eqn [7] predicts the inactivated state area of PaMscS-1 to be  $5 \pm 1 \text{ nm}^2$ .

Due to the topology of the transition diagram (Fig. 3.1), it is also now possible to assign unique energies to the states by choosing a reference state. For example, if we assign the energy of the closed state to be zero, we can uniquely determine the energy of the open and the closed state by using the relation [153]:

$$E_{Open} = E_{Closed} + \beta^{-1} \ln \frac{k_{OC}}{k_{CO}} = 0 + \beta^{-1} \ln \frac{1e + 4}{4e - 6} = 22 \pm 1 \text{ kT}$$

$$E_{Inactivated} = E_{Closed} + \beta^{-1} \ln \frac{k_{IC}}{k_{CI}} = 0 + \beta^{-1} \ln \frac{0.18}{2e - 5} = 9 \pm 1 \text{ kT}$$

These relationships assign the energies for the bottoms of the open and inactivated state wells on the energy landscape.

To test the correctness of the kinetic constants and their tension dependences obtained in the above experiments, we simulated MscS ramp responses with the coefficients listed in Table 3.1. In parallel, we employed the same time-dependent ramp protocols where the membrane tension was linearly raised from zero to its final value of  $3 k_B T/nm^2$  in 1, 5, 10, 30 and 60 s, thus changing the rate from fast to slow. As shown previously, MscS channels prefer to fully respond to abrupt stimuli but tend to ignore the slowly applied ones; this behavior was called the “dashpot” mechanism. Not surprisingly, as the tension increases from zero to the saturating level, it passes through a specific region, which roughly corresponds to  $\gamma_{0.5}$ , where the likelihood of switching from the closed to the inactivated state is the highest. At slower rates of stimulus application, channels spend more time in this specific range of tensions and a larger fraction of channels is predicted to end up in the inactivated state. Fig. 3.8A shows experimental traces (blue) that reflect the fraction of active channels in the patch. All traces were normalized to the amplitude of the fastest ramp response that exhibits the maximal number of active channels. As seen from the bottom part of the graph, tension was raised to its final value of  $3 k_B T/nm^2$  with different rates. Indeed, with the slower rates only about half of the population remains active. The simulation of a 30000-channel Markov chain using the QuBexpress software under the same conditions is shown by the red curves (Fig. 3.8A, B) which reasonably reproduces the kinetic inactivation mechanism of MscS.

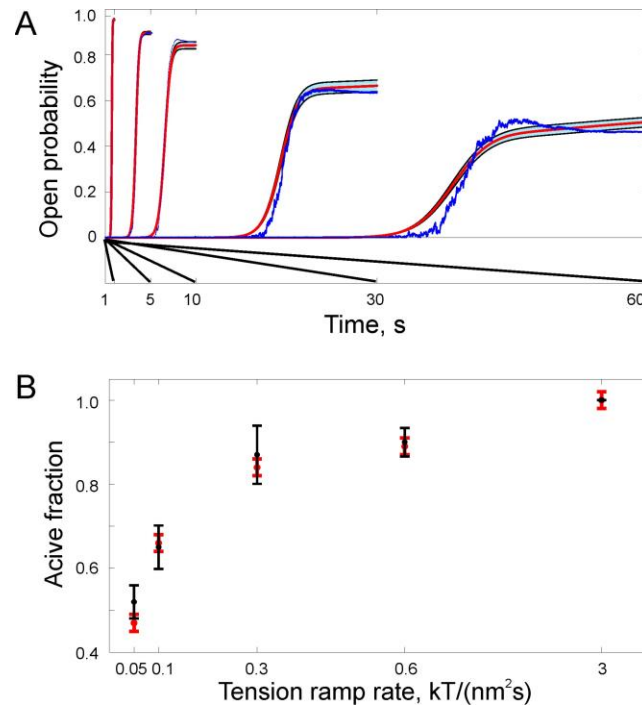


**Figure 3.8. The rate dependency of MscS inactivation.** (A) The plot of the fraction of the open channels normalized to 1s ramp (fastest). The tension in the membrane was linearly raised to its final value with different rates. At slower rates, channels spent more time in the tension region where inactivation can be achieved. Thus, the slower the application of stimulus, the more likely the channels are to end up in the inactivated state, which can be seen as the decrease in the membrane current. The red curves were the average traces of 30000-channel MscS population simulated by the QUBexpress software with the parameters listed in Table 3.1 and are in good agreement with the blue traces that correspond to a single realization of the experimental MscS data. Shaded areas between the black curves represent the standard deviation envelope – the variability in simulations’ output due to variability in the kinetic constants (as listed in Table 3.1) (B) Relative number of the active channel population with different tension application rates obtained from three independent experiments (black) was successfully described by the model (red).

### Discussion

In this study of the tension-driven opening and inactivation transitions in the low-threshold bacterial mechanosensitive channel MscS, we took the most basic approach and derived major relationships analytically. Eqn 3 essentially represents the classical Q-matrix for the transition rates previously used by Colquhoun [59,60], Sachs [61] and others. With some simplifying assumptions we were able to find



closed forms for the main experimentally measured relationships and fit the activation and closing curves directly. The fitting of the dose-response curves measured with ramps (Fig. 3.3) and pulse-step protocols (Fig. 3.4), inactivation and recovery rates as a function of tension (Fig. 3.5) as well steady-state fraction of inactivated channels as a function of conditioning tension (Fig. 3.6) provided consistent reliable estimates for the rates, spatial expansion parameters and positions for rate-limiting barriers for both the opening and inactivation transitions (Table 3.1). This analytical exercise revealed important relationships between the protein area increase associated with inactivation, activation midpoint and the tension of maximal inactivation (Eqn. 3.7), which would not be evident from purely numerical fitting with existing software. In the end, we resorted to the advanced kinetic modeling and fitting software QuB to fit the dynamic activation traces obtained with ramps of different speed (Fig. 3.8) and confirmed that the extracted kinetic and spatial parameters are realistic.

Note that the general formalism developed here can be applied to other ion channels whose transition rates depend on some other physical parameters such as voltage or ligand concentration. For example, the transition rates between the states might be in the form of  $k_0 \exp(k_1 * Voltage)$ , meaning that the probability per unit time to make a jump in the state space is modulated by the voltage across the membrane. As long as the system is irreducible, memoryless and has a finite number of states, the main results derived in this paper hold for other types of channels in different organisms. Even though we used QuB express software just to simulate our model based on the parameters listed in Table-3.1, QuB express can do a lot more. Since the inactivated state is tension-insensitive and non-conductive, for our three-

state system, we were able to monitor  $P_{Open}$ ,  $P_{Closed}$ ,  $P_{Inactivated}$  as function of time but for systems which have hidden Markov states or some other sub-conducting states, the patch-clamp experiments do not provide the full information on the evolution of the probabilities thus the system is hard to tackle analytically. QuB software can be useful for such cases by utilizing likelihood optimization methods to extract the underlying model from the data [157].

The determined spatiotemporal parameters of MscS transitions (Table 3.1) based on the inferred states predict that the energy landscape for MscS functional cycle must have at least 3 wells for the closed (C), open (O) and inactivated (I) states (Fig. 3.9). At zero tension, the opening path predicts a barrier that is located about 55% toward the O well, which is located at a distance of  $11 \text{ nm}^2$  and elevated by about  $22 \text{ k}_B\text{T}$  relative to the C well. The inactivation profile predicts a smaller distance of about  $6.5 \text{ nm}^2$  between the C and I wells, the energy difference of  $9 \text{ k}_B\text{T}$  and the rate-limiting barrier located very close to the I well (~80 % of the way). Application of “midpoint” tension  $\gamma_{0.5}=7.85 \text{ mN/m}$  that tilts the landscape (Fig. 3.9B) and that puts the bottoms of C and O wells at the same level also drags the I well below the C well prompting inactivation.

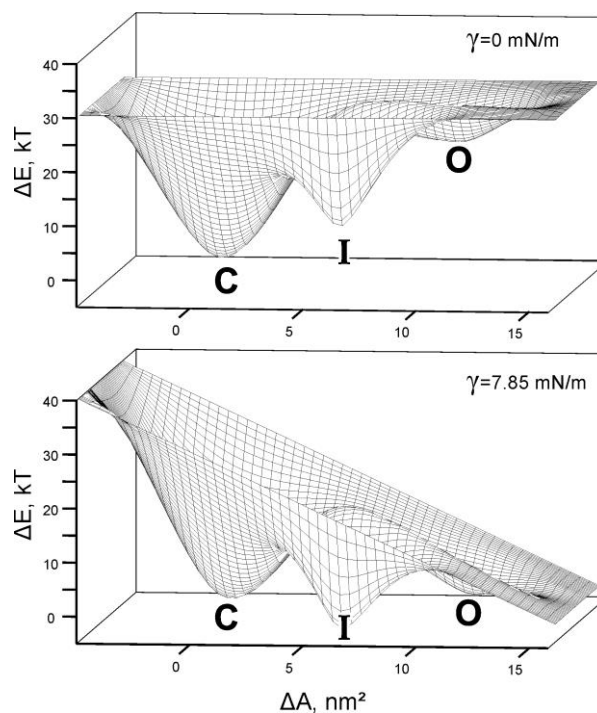


**Figure 3.9. The reconstructed energy landscape predicted for MscS in a relaxed membrane ( $\gamma = 0$ ) and under tension  $\gamma_{0.5} = 7.85$  mN/m, at which open and closed states are equally populated.** In the latter case the I state has a lower energy than both the C and O states, thus making the inactivated state preferable. The passage to the I state becomes accessible from the C state, whereas a ridge separating the O and I states prevents inactivation from the open state. Application of stronger tension skews the landscape more and drives the closed population to the open state. Importantly, inactivated channels at high tensions remain ‘locked’ in the inactivated state.

The obtained protein expansion parameters may provide some insight into the structural aspect of MscS gating and suggest the character of helical arrangement in each of the states and motions during the transitions. The existing crystal structures and structural models of MscS gating have been overviewed in [48] and our analysis of area changes associated with specific transitions in different models is presented in the Supplement.

Although the release system in *E. coli* is comprised of MscL, MscS and five MscS-related channel species [35,91,92], the low-threshold MscS and the high-threshold MscL were shown to mediate the bulk of osmolyte exchange and either one is sufficient to rescue the majority of bacterial population from osmotic lysis [35]. Despite the earlier assumption that MscS and MscL perform essentially the same function [93–95], there is more data that each of the channels has evolved to perform its own specific role. The gating parameters of MscS defined by its energy landscape reported here can be interpreted in the context of its *in-vivo* function.

Subjected to strong (500-1000 mOsm) osmotic downshifts, bacterial cells swell and generate super-threshold tensions in their cytoplasmic membranes within 20-30 ms, and then a release phase with a characteristic time of 30-100 ms begins [29,53]. Based on the parameters presented in Table 3.1, when tensions exceed  $3 k_B T/nm^2$  (or 12 mN/m), MscS is predicted to open within 10 ms. This rate is too fast to be resolved in a typical patch-clamp experiment, but it is certain that MscS population will robustly open at sublytic tensions within the swelling time. The opening speed is important because in order to curb swelling the population must be able to release excessive osmolytes faster than the rate of water influx.

Regarding the closing rate, it is estimated to be fast ( $\sim 10,000 s^{-1}$ ) at zero tension. But it is important to keep in mind that as the osmolytes are dissipating, membrane tension decreases until the channels close. Therefore, channel activity cannot adjust membrane tension below its own activation threshold. For MscS, the threshold tension is near 5 mN/m ( $\sim 1.3 k_B T/nm^2$ ) and at this tension the closing rate is predicted to be  $\sim 3 s^{-1}$  (Fig. 3.4B), i.e., the channels will be closing *in vivo* with

characteristic time of 0.3 s or slower. This kinetic impediment will provide sufficient time for osmolyte and water exchange between the small cell and the environment in the absence of high intracellular pressure, thus reducing tension to a sub-threshold level.

As illustrated in Figs. 3.5, the rates of inactivation and recovery are generally slow compared to the rates of activation and closure, apparently due to a sufficiently high barrier separating the C and I states, smaller expansion ( $\Delta A$ ) during the inactivation, and location of the rate-limiting barrier close to the inactivated state. In terms of activation and inactivation, MscS in our experiments essentially functions in two separate time scales. The smaller area change associated with the inactivation process dictates a much shallower tension dependence. But what is special about this transition is that with the given parameters inactivation only takes place at moderate tensions just above the activation threshold ( $\sim 1.3 \text{ k}_B\text{T} / \text{nm}^2$ ) and is significantly boosted at around the activation midpoint ( $\sim 2.0 \text{ k}_B\text{T} / \text{nm}^2$ ) where the exchange rate between the open and closed state of the channel is maximized (Fig. 3.6). It has been analytically shown that the relationship between activation midpoint,  $\gamma_{0.5}$  and the tension  $\gamma^*$  at which the steady-state degree of inactivation is the highest depends on the areas of open and inactivated states. This allows estimation of inactivation area without the complex experimental protocols and analysis exemplified in Fig. 3.5, but rather from a set of more easily accessible parameters (Fig. 3.6 and 3.7). The reconstructed energy landscape well predicts “smart” behavior of fully responding to abrupt stimuli (emergency situations) but ignoring tension stimuli which are applied slowly (non-emergency situations).

Tension-dependent inactivation of low-threshold MscS channels is common for the three gram-negative bacterial species studied by patch-clamp: *E. coli* [46,51], *V. cholerae* [96], and *P. aeruginosa* [29]. It is interesting to note that even though both *P. aeruginosa* and *E. coli* have MscS and MscL type channels, *P. aeruginosa* mainly relies on MscL family channels to counter osmotic down-shocks. Compared to *E. coli*, *P. aeruginosa* has a cell envelope that is somewhat less permeable to water, which slows down swelling and provides more time for osmolyte extrusion in the event of osmotic shock. The smaller cell size and higher density of MscL apparently makes *P. aeruginosa* more resistant to abrupt osmotic down-shocks than *E. coli* (Çetiner et al., 2017). The fact that *P. aeruginosa* still has a certain amount of MscS capable of inactivation suggests a special role that inactivation plays in osmotic permeability response.

The specific role of the low-threshold inactivating MscS in the osmotic response and functional cooperation with the non-inactivating (two-state) high-threshold MscL channel may be envisioned in the following way. At low-magnitude shock, the low-threshold MscS may completely fulfill the pressure/volume adjustment without engaging MscL. At higher shocks, MscL will activate and take the major part in the fast osmolyte release, but when tension drops down to MscL threshold ( $\sim 9$  mN/m) it will close and the tension adjustment will be stalled at that level. Under these conditions, the non-inactivating MscL will still be able to flicker to the open state, which will be disruptive for vital gradients and cell energetics. MscS appears to be a critical asset in this situation. Fully open at 9 mN/m ( $\sim 2.3$  k<sub>B</sub>T/nm<sup>2</sup>), MscS will continue the dissipation process to take membrane tension considerably

below MscL threshold. At its own activation midpoint of 7.8 mN/m ( $\sim 2k_B T/nm^2$ ) or below MscS will inactivate and this would be a proper leak-free termination of the osmotic permeability response. This picture should be augmented by the findings that the rate of inactivation (but not the preferable tension range) sharply increases in the presence of cytoplasmic crowders. The increased macromolecular excluded volume is an indicator of the cytoplasm “over-draining” and the signal for faster MscS inactivation that prevents small osmolyte and water extrusion.

We conclude that the existence of a non-conductive, tension-insensitive (inactivated) state and the location of the inactivated state well on the energy landscape relative to other states are not coincidental but rather the result of a billion-year evolution to provide a more efficient and “economic” response to osmotic challenges, thus contributing to the osmotic fitness of bacteria in the ever-changing environment.

## **ACKNOWLEDGMENTS**

We would like to thank the reviewers for their detailed comments and suggestions for the manuscript. The work was supported by NIH R21AI105655 and RO1 GM107652 grants to SS. UC was supported by the U.S. Department of Education GAANN “Mathematics in Biology” Scholarship. UC is also indebted to Drs. Oren Raz (Weizmann Institute of Science) and Yiğit Subaşı (Los Alamos National Laboratory) for their stimulating discussions. The authors thank Ms. Stephanie Sansbury for cloning MscS into a tightly-regulated pBAD expression system and Madolyn Britt for editorial comments.

## **Chapter 4: Recovery of equilibrium free energy from non-equilibrium thermodynamics with mechanosensitive ion channels in *E. coli***

Uğur Çetiner<sup>1,2,3</sup>, Oren Raz<sup>4,6</sup>, Sergei Sukharev<sup>1,2,3</sup> and Christopher Jarzynski<sup>1,2,4,5</sup>

<sup>1</sup>Institute for Physical Science and Technology, <sup>2</sup>Maryland Biophysics Program, <sup>3</sup>Department of Biology, <sup>4</sup>Department of Chemistry and Biochemistry, <sup>5</sup>Department of Physics, University of Maryland, College Park, MD 20742, <sup>6</sup>Department of Physics of Complex Systems, Weizmann Institute of Science, Rehovot 7610001, Israel.

### **Abstract**

Bacterial mechanosensitive channels are major players in cells' ability to cope with hypo-osmotic stress. Excess turgor pressure is reduced as the channels, triggered by membrane tension, open and release osmolytes. However, in vitro measurements of the free energy difference between the open and closed states of ion channels are challenging due to hysteresis effects and inactivation. Exploiting recent developments in statistical physics, we present a general formalism to extract the free energy difference between the closed and open states of mechanosensitive ion channels from non-equilibrium work distributions associated with the channels' gating. We show that the work distributions obtained from the gating of MscS channels in *E. coli* membrane satisfy the strong symmetry relations predicted by the fluctuation theorems and recover the equilibrium free energy difference between the closed and open states



of the channel within 1 k<sub>B</sub>T of its best estimate obtained from an independent experiment.

### **Introduction**

The biological membrane is the fingerprint of living systems. The separation of cellular contents from the rest of the environment was the essential step for life to emerge at the expense of an osmotic stress [158–160], thus organisms must carefully manage the amount of internal water and osmolytes in response to variations in osmotic pressure as they change their environment in order to meet basic needs such as food and escaping from predators.

The process of converting mechanical stresses on the cell membrane into electrochemical signals is believed to be one of the oldest physiological responses of living systems to the osmotic challenges, dating back to 3.8 year billion years ago, and is well characterized in bacteria [10,28,111,161,162]. When bacteria are exposed to hypo-osmotic stress, e.g. during a rain storm, the turgor pressure builds to dangerous levels in a few milliseconds due to high membrane water permeability [28,29,53]. One of the main mechanisms to evade mechanical rupture due to extreme internal turgor pressure is the activation of mechanosensitive ion channels (MS) in the membrane. These reduce excess turgor by releasing internal osmolytes and water (Fig. 4.1A). In bacteria, the bulk release of ions and other osmolytes is mainly mediated by two families of mechanosensitive channels: MscS and MscL. The 3-nS MscL family channels gate at near lytic tension and therefore serve as a “last back up” mechanism against extreme osmotic down shocks by forming large non-selective pathways in the membrane [34,130,163]. The MscS

channels, on the other hand, have a conductance of 1 nS, require less tension to open and come with great diversity in structure and functionality [35,48,129,164,165].

Recent findings have suggested that in order to survive under extreme hypo-osmotic conditions, the rate of turgor release via mechanosensitive ion channels should keep up with the rate of turgor generation caused by the water influx [29,30,166]. According to this mechanistic picture, the osmotic water permeability of the cell envelope and the magnitude of the shock determine the rate of water influx whereas parameters such as channel density, conductance, and the free energy difference between the closed and open conformations ( $\Delta F$ ) govern the rate of osmolyte release.

In order to develop a quantitative understanding of survival and fitness in microbial world under extreme osmotic stress, it is crucial to obtain accurate information on all the relevant parameters of the MS channels. The free energy difference  $\Delta F$ , an indispensable part of the electrophysiological characterization of the channels, is of particular interest to experimentalists.

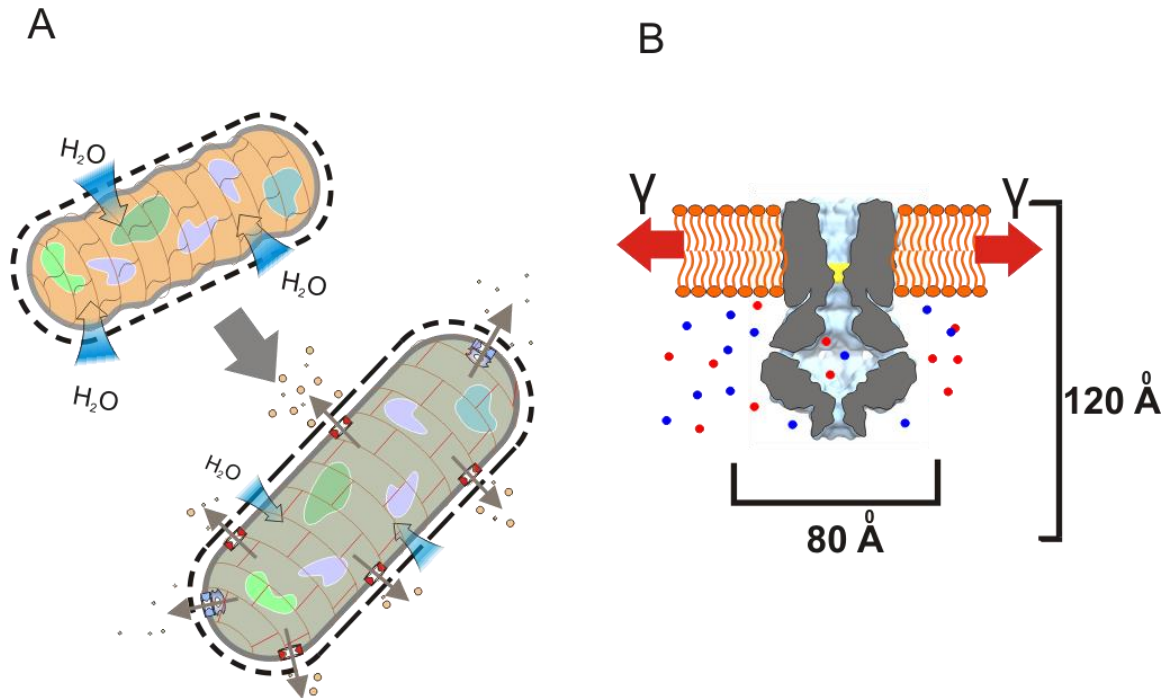


**Figure 4.1. (A) Bacterial response to osmotic downshock.** Water influx is accompanied by elastic deformation of the cell wall and stretching the cytoplasmic (inner) membrane. Mechanosensitive channels open and release small osmolytes together with water. When tension and volume return to normal, channels close. **(B)** Cartoon of MscS channel in the closed conformation. As tension increases, the free energy difference between the open and closed state decreases thus in the presence of membrane tension, the open state becomes energetically more favorable.

The most common way to measure  $\Delta F$  is to ramp the membrane tension linearly in time until all the channels are open, while measuring the conductivity between the two sides of the membrane. These traces of conductivity vs. tension – the dose response curve – correspond (when properly normalized) to the probability of finding the channel in “open” or “closed” states. This probability is fitted to a two-state Boltzmann distribution function, and the free energy difference is extracted from the distribution [46,130,155,163,167]. A crucial assumption in this method is that the distribution of states is accurately described by the Boltzmann distribution. Whereas this is a perfectly valid assumption for a system in thermal equilibrium, it might not hold for systems out of equilibrium. Indeed, if the protocol is delivered in a time

symmetric manner such that the membrane tension is increased and decreased with the same rate as in a triangular ramp protocol, the current follows different paths on the ascending and descending legs of the dose response curve and displays a clear hysteresis loop – the fingerprint of non-equilibrium processes. The choice of equilibrium-based formalism to extract the free energy difference for a non-equilibrium process may contribute to the variability in  $\Delta F$  in the literature, ranging from  $5 k_B T$  to  $28 k_B T$  for the same MscS channel [46,47,168].

In many cases, by delivering the stimulus slowly it is possible to obtain the free energy difference from the “reversible” work,  $W_{rev} \cong \Delta F$ . However, there are channels such as *E. coli* MscS and PaMscS-1 that undergo inactivation and become non-conductive and insensitive to tension as they are pulled slowly. This phenomenon, which is called “the Dashpot Mechanism”, prevents data acquisition at a slow enough rate to assume thermal equilibrium [29,51].

In this article, we present alternative and more reliable ways to obtain the free energy difference between the open and closed state of MscS by making use of recent developments in statistical physics. In 1997, Jarzynski showed that it is possible to obtain the free energy difference between two equilibrium states (A, B) from the non-equilibrium distribution of the work performed on the system during a thermodynamic process connecting A to B [85]:

$$\langle e^{-\beta W} \rangle_{A \rightarrow B} = e^{-\beta \Delta F} \quad [1]$$

Here the angular brackets represent the ensemble average taken over many realizations of the same switching protocol starting from an equilibrium state (A) in contact with a heat reservoir at temperature  $T$ .  $\beta$  is defined as  $1/k_B T$  where  $k_B$  is the Boltzmann constant. In 1999, Crooks proved that the work distributions associated with the thermodynamic process of switching the system from A to B and with the corresponding time-reversed protocol of switching the system from B to A (where the system starts in the corresponding equilibrium state, A or B) satisfy the following symmetry relation [86]:

$$\frac{P_{A \rightarrow B}(W)}{P_{B \rightarrow A}(-W)} = e^{\beta(W - \Delta F)} \quad [2]$$

These fluctuation theorems are robust regardless of how microscopic dynamics are modeled [84,169–174], and they have been experimentally verified in various systems [74,175–181].

Using these theoretical results, we present a general framework that enables one to extract the free energy difference between the open and closed state of ion channels in the patch clamp experiments from the non-equilibrium generalized work distributions associated with the gating of mechanosensitive ion channels. Having several channels in the membrane provides the advantage of obtaining many data points in a single realization of the experimental protocol. Thus, the statistics from which the work distributions can be extracted enables fast convergence for eqns [1] & [2] [182,183]. Moreover, a recent study, which modeled MscS gating as a

discrete state continuous-time Markov chain [184], enabled us to validate these fluctuation theorems using mechanosensitive ion channels in a patch clamp setup.

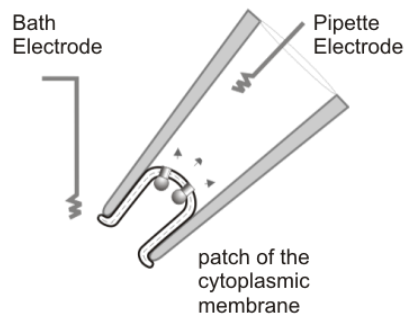
### Experimental and Theoretical Setup

The patch clamp technique was developed by Erwin Neher and Bert Sakmann in the late 70s and early 80s [37–39]. It enables researchers to characterize the electrophysiological properties of ion channels by clamping a piece of a membrane as a giga-ohm seal in a polished glass micropipette (Fig. 4.2A). The high resistance of the seal provides an electrical isolation across the membrane. However, conducting pathways can be generated by activation of mechanosensitive ion channels in response to applied tension. This activation can be monitored with pico-amp precision. Observations of discrete currents passing through individual channels made patch-clamp essentially the very first single-molecule technique.

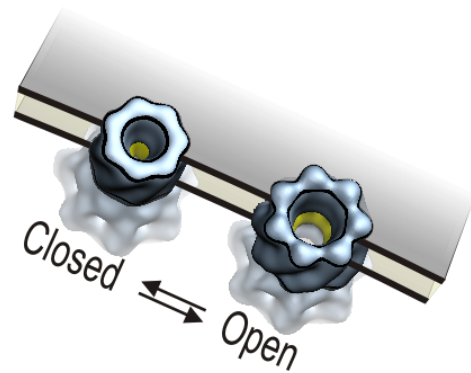
In our experiments, the system of interest is the collections of mechanosensitive ion channels naturally embedded in the *E. coli*'s membrane. The micropipette with the clamped membrane is immersed into the bath solution at room temperature, which serves as a thermal reservoir. The “work parameter” (see definition below) is the membrane tension,  $\gamma$  and the conjugate variable to work parameter is the lateral protein area expansion,  $A$  (Fig. 4.2B). The application of suction changes the pressure between the two sides of the membrane hence varies its tension, which allows us to perform work on the system and lower the free energy difference between the open and closed state. Thus, in the presence of external tension on the membrane, states with larger area become favorable [130,147].

A typical experimental protocol starts with a membrane without any tension in which all ion channels are in the closed state and the conductance is negligible. Then, a linear increase in the membrane tension to a value of about  $3 k_B T/nm^2$  in 1s is applied. This tension is kept constant for another second to let the system relax to an equilibrium state corresponding to the final value of the work parameter. Once the system has reached its equilibrium distribution, the tension is decreased back to  $0 k_B T/nm^2$  at the same rate.

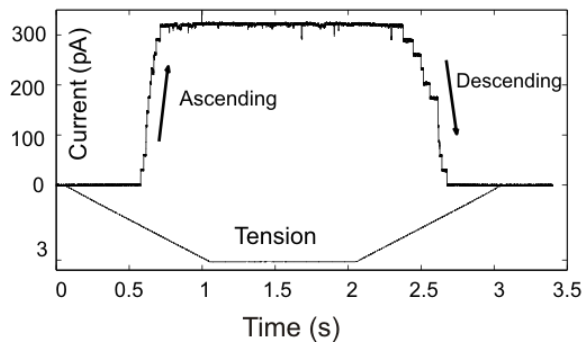
**A** Channel recording *in vitro*



**B**



**C**



**D**

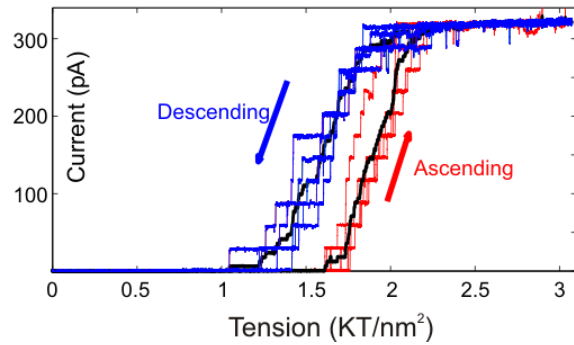


**Figure 4.2. (A) Patch-clamp applied to giant bacterial spheroplasts has been the most informative way of obtaining functional characteristics of bacterial mechanosensitive channels (Martinac et al. 1987).** A micron-size glass pipette holds a cup-shaped patch separating the inside of the pipette from the bath. Application of suction to the pipette stretches the curved patch membrane according to the law of Laplace and generated tension activates the channels. The two electrodes inside and outside the pipette measure the current reflecting the opening and closing transitions in individual channels. **(B)** A blow-up of a fragment of the patch membrane showing two channels, one in the closed and one in the open state. The open channel has a larger cross-sectional area in the plane of the membrane. As membrane tension increases, the free energy difference between the open and closed state decreases thus in the presence of membrane tension, the open state becomes energetically more favorable. **(C)** An example of typical trace containing 11 MscS channels and the tension stimulus shown below. On ascending leg, membrane tension was increased linearly,  $\gamma = rt$  at a rate  $r = 3 k_B T/nm^2 s^{-1}$  until all the channels in the membrane opened, manifested as the saturation of the current. After 1s of equilibration at  $3 k_B T/nm^2$  the tension was decreased back to  $0 k_B T/nm^2$  at the same constant rate,  $r$ . The descending leg depicts the closure events of the channels. **(D)** Five representative traces from the same patch were plotted as function of tension in order to emphasize that the single channel events are stochastic and the system displays hysteresis as demonstrated by the averaged traces (black curves).

Fig. 4.2C displays a characteristic response of the current to the tension protocols described above: each step of current increase (decrease) represents a single channel opening (closing) event. In the specific example of Fig. 4.2C there are 11 mechanosensitive channels which are open at the final tension equilibrium state. Note that the longer the membrane is exposed to high tension values such as  $3 k_B T/nm^2$ , the greater the chance that it ruptures. Therefore, 1s holding period is a safe time scale not only to reach the equilibrium (assuming that the system's relaxation time at  $3 k_B T/nm^2$  is a few milliseconds) but also to obtain a few realizations before the seal is lost (see SI Fig. S1). Fig. 4.2D shows five representative current traces of the same protocol, applied on the same membrane. We emphasize that: (i) Even though the same protocol is employed, the channel gating is fluctuating. We will show that these fluctuations satisfy strong symmetry relations. (ii) As indicated by the trajectories average currents (the black curves Fig. 4.2D), the system displays clear hysteresis,



which is the hallmark of non-equilibrium processes. Therefore, assuming that the distribution of open and close states follows the Boltzmann distribution at all times is not a valid assumption, and non-equilibrium fluctuation theorems would be more suitable to extract the free energy difference between the open and the closed state of the channel.

We model MscS as a two-state system (“open” and “closed”), and introduce a state variable,  $\sigma$ , which is 0 for a closed channel and 1 for an open one. Let  $\varepsilon_{closed}$  and  $\varepsilon_{open}$  denote the energies of the closed and open states. In the presence of tension  $\gamma$ , the energy of the system can be written as [11,185,186]:

$$H(\sigma, \gamma) = H_0(\sigma) - \gamma A(\sigma) \quad [4]$$

where the term  $H_0(\sigma) = (1 - \sigma) \varepsilon_{closed} + \sigma \varepsilon_{open}$  represent the energy of the system due to the state of the ion channel alone, and the additional term  $\gamma A(\sigma) = \gamma \sigma \Delta A$  represents the energy difference between open and close channels in the presence of tension, where  $\Delta A$  is the area difference between the closed and open state of the channel.

For a single realization of the experimental protocol of duration  $\tau$ , the work is defined as the energy difference associated with the changes in the external tension:

$$W \equiv \int_0^\tau \dot{\gamma} \frac{\partial H}{\partial \gamma} dt = -\Delta A \int_0^\tau \dot{\gamma} \sigma dt \quad [5]$$

This work takes on different values in different realizations, namely it fluctuates from one realization to another. We should note that eqn. [5] is the work definition used in the context of non-equilibrium thermodynamics and it differs from the classical textbook definition of mechanical work. (See [187,188] for a detailed discussion). Writing eqn. [5] in discrete time steps is convenient for our purpose, since the experimental acquisition yields digitized data in discrete steps, whose size depends on the sampling frequency. Considering that the tension ( $\gamma$ ) is increased linearly from zero to its final value  $\gamma_{Final}$  in  $M$  small enough time steps, a dynamical path for a single channel might be described by the following sequences:

$$\begin{aligned} \{\gamma_k; 0 \leq k \leq M\} &\rightarrow \{\gamma_0, \gamma_1, \dots, \gamma_k \dots \gamma_{Final}\} \\ \{\sigma_k; 0 \leq k \leq M\} &\rightarrow \{0, 0, 0 \dots 1, 1, 1, 1, 1\} \end{aligned}$$

The work performed on the system, eqn. [5], can be rewritten in discrete time for a single realization as [189]:

$$W = -\Delta A \sum_{k=0}^{M-1} (\gamma_{k+1} - \gamma_k) \sigma_{k+1} \quad [6]$$

A typical realization, for a cyclic protocol, is depicted in Fig. 4.3 where the red curve represents the opening event and the blue curve is the closing event. For the sake of simplicity, let us assume  $\Delta A = 1 \text{ nm}^2$ . In this case, for the ramp increase in the tension, eqn. [5] implies that the work done is minus the area under the  $\sigma$  vs  $\gamma$  curve. Specifically, the work performed in order to open the channel,  $W_{C \rightarrow O}$ , is equal to minus the area under the red curve, which is denoted by  $-W_O$ , and the work performed during the closure  $W_{O \rightarrow C}$  equals to the area under the blue curve,  $X + W_O$ ,

where  $X$  is the area bounded by the two curves (See Fig. 4.3). Therefore, the total dissipation during the thermodynamic cycle is  $W_{Diss} = W_{C \rightarrow O} + W_{O \rightarrow C} = X > 0$ . In other words, the average work done in order to open the channel is greater than the average work performed as the channel closes. However, in some rare realizations the thermal noise might act on the channel ‘‘constructively’’ and the channel might gate at lower work values than the free energy difference,  $W < \Delta F$ , violating the second of thermodynamics transiently.

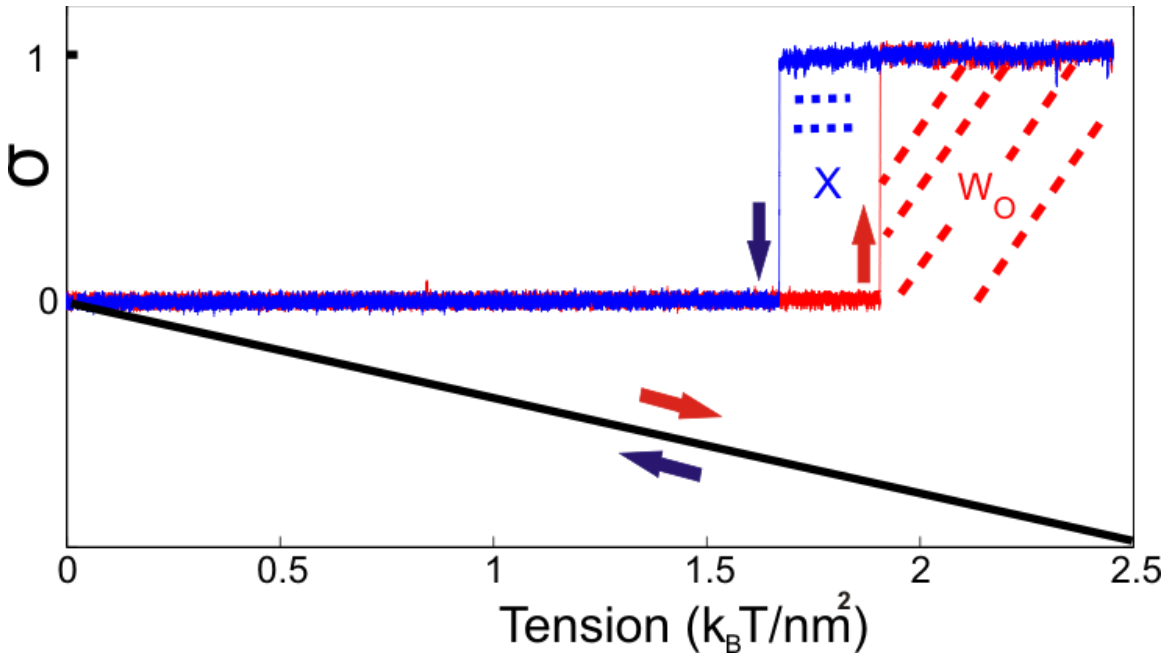


**Figure 4.3. The gating (red) and closure (blue) of a single channel in response to linear increase and decrease of the membrane tension with the same rate.** For the sake of illustration, assume  $\Delta A = 1 \text{ nm}^2$ . In this case  $W = -\Delta A \sum_{k=0}^{M-1} (\gamma_{k+1} - \gamma_k) \sigma_{k+1}$  gives the work performed during the gating,  $W_{C \rightarrow O}$ , as minus the area under the red curve ( $-W_O$ ) and the work performed during the closure  $W_{O \rightarrow C}$ , as the area under the blue curve ( $W_C + X$ ). The total dissipation for this cyclic process is  $W_{Diss} = W_{C \rightarrow O} + W_{O \rightarrow C} = X > 0$  which holds on average for small systems. For some rare realizations, it is possible to receive more work than what is put in giving  $W_{Diss} < 0$ . Imagine a realization where the colors and the direction of the arrows are swapped and the red curve now represents the closure and blue curve depicts the gating, in this case:

$$W_{Diss} = W_{C \rightarrow O} + W_{O \rightarrow C} = -X < 0$$

## **Results**

An edge detection program was used to identify single channel events in all the traces (see SI Fig. S2). The corresponding work distributions associated with the channel's opening at a given tension protocol,  $P_{C \rightarrow O}(W)$ , and the closing work distribution at the time reversed protocol,  $P_{O \rightarrow C}(-W)$ , were obtained from two independent experiments, and are depicted in Fig 4.4. The work values were binned into 13 equally spaced intervals. Note that according to [eqn. \[2\]](#), at the work value  $W_0$  for which  $P_{C \rightarrow O}(W_0) = P_{O \rightarrow C}(-W_0)$ , it holds that  $W_0 = \Delta F$ . In other words, the work distributions of the forward and backward protocols cross at  $W = \Delta F$ . This observation, although quite convenient, does not provide an optimal method to extract  $\Delta F$  since it only uses local behavior of the work distributions around the crossing point, whose exact location depends on the choice of the bin size. Instead, the plot of  $\log(P_{C \rightarrow O}(W)/P_{O \rightarrow C}(-W))$  as a function of  $W/k_B T$  provides a better estimate as it relies on the whole distribution. The points on the semi-log plot follow a straight line with slope 1 and intercept the work axis at  $\Delta F$ . Based on the plotted measurements, the free energy difference is estimated to be  $-15.3 k_B T$  from the crossing point in Fig 4.4 while the straight line, in supplementary Fig. S3A intercept work axis at  $-14.7 k_B T$  with the slope of 0.98.

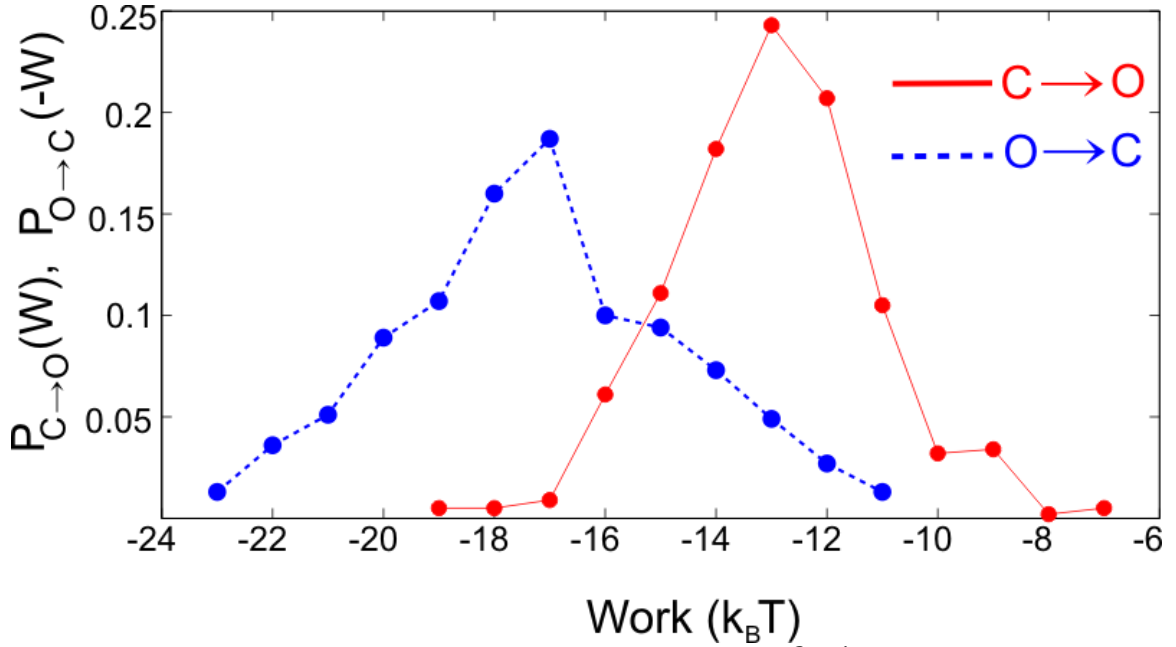


**Figure 4.4 Histograms of the work distributions at  $3 k_B T / nm^2 s^{-1}$ .**  $N=440$  for the opening ( $C \rightarrow O$ ) and  $N=449$  for the closing ( $O \rightarrow C$ ). The protocol was carried time symmetrically. The work distributions cross at  $-15.3 k_B T$ . The individual work values were obtained from the following definition:  $W = -\Delta A \sum_{k=0}^{M-1} (\gamma_{k+1} - \gamma_k) \sigma_{k+1}$ .

It should be noted that even though the plot of log ratio of the work distributions as a function of work exploits the full distributions and offers an improvement, the overall probabilities still depend on the binning size. Moreover, this method is only useful on the condition that there is a significant overlap between the work distributions, therefore for highly dissipative processes, the overlap would be quite poor and alternative statistical techniques such as Bennett's acceptance ratio method (see Supplementary Information, Fig. S3B) can be used to recover  $\Delta F$  [87,190,191].

Jarzynski equality (eqn. [1]) for the closed  $\rightarrow$  open transition,  $\langle e^{-\beta W} \rangle_{C \rightarrow O} = e^{-\beta \Delta F}$ , and for the open  $\rightarrow$  closed transition,  $\langle e^{-\beta W} \rangle_{O \rightarrow C} = e^{\beta \Delta F}$ , provide another estimation for  $\Delta F$ . These give  $-14.9 \pm 0.4 k_B T$  and  $14.1 \pm 0.4 k_B T$ , respectively. Thus, the average,  $-14.5 \pm 0.3 k_B T$  is the  $\Delta F$  predicted by Jarzynski equality. The overlapping

distribution method [190,192] is also in good agreement with other estimators and reports  $\Delta F$  to be  $-14.7 k_B T$  (See Supplementary Information, Fig. S4). Finally, the Linear Response Theorem (LR) recovers the free energy from the average work done during the opening or from the average work received during the closing and the corresponding standard deviations of the work distributions as follows [193]:

$$\Delta F_{LR} = \langle W \rangle_{C \rightarrow O} - \frac{\beta \sigma_{C \rightarrow O}^2}{2} \text{ or } \Delta F_{LR} = -\langle W \rangle_{O \rightarrow C} + \frac{\beta \sigma_{O \rightarrow C}^2}{2} \quad [7]$$

which results in  $\Delta F_{LR} = -14.7 \pm 0.2 k_B T$  and  $-13.8 \pm 0.3 k_B T$ , respectively. The summary of the results produced by different estimators is listed in Table 4.1 with standard deviations in units of  $k_B T$ . Uncertainties were obtained using the bootstrap method [194].

$\langle W \rangle_{C \rightarrow O}$	$\sigma_{C \rightarrow O}$	$\langle W \rangle_{O \rightarrow C}$	$\sigma_{O \rightarrow C}$	$\langle W_{Diss} \rangle$	$\Delta F$ Linear Response	$\Delta F$ Jarzynski	$\Delta F$ Crooks	$\Delta F$ Bennett	$\Delta F$ Crossing	$\Delta F$ Overlapping
-13.0	1.82	17.2	2.60	4.2 $\pm 0.2$	-14.2 $\pm 0.2$	-14.5 $\pm 0.3$	-14.7 $\pm 0.2$	-15.0 $\pm 0.5$	-15.3 $\pm 0.6$	-14.7 $\pm 0.2$

**Table 4.1. Summary of Results.**  $\langle W_{Diss} \rangle = \langle W \rangle_{C \rightarrow O} + \langle W \rangle_{O \rightarrow C}$ , is the average dissipation during the cyclic process (C→O→C). The linear response prediction and Jarzynski estimations are the averages of the free energy differences obtained for the opening and closing current trajectories.  $\Delta F$  from the intersection of the work distributions was predicted to be  $-15.3 k_B T$ . A better estimate is achieved by using the semi-logarithmic plot of Crooks' Fluctuation Theorem which gives  $\Delta F = -14.7 k_B T$  (See SI Fig. S3A). Overlapping distribution method is in line with other estimators and predicts  $\Delta F = -14.7 k_B T$ . The Bennett's acceptance ratio method, which is our best guess for the free energy, reveals it to be  $-15.0 k_B T$ . (See the Supplementary Information, Fig. S3B)

It is important to note that the free energy estimations in Table 4.1 refer to equilibrium free energy differences between two equilibrium states associated with

the initial and final value of the work parameter (system + driving force) [176]. For a typical experimental protocol in this paper,  $\Delta F \equiv F(\gamma_\tau = 3 k_B T/\text{nm}^2) - F(\gamma_0 = 0 k_B T/\text{nm}^2)$ , whereas  $\Delta F_0$  represents the free energy difference between the closed and open state of the channel in the absence of any tension. Therefore, even though  $\Delta F$  depends on the end points of the work parameter,  $\Delta F_0$  should be independent of the protocol and can be recovered by adding the corresponding boundary term to  $\Delta F$ :

$$\Delta F_0 = \Delta F + \gamma \Delta A|_0^\tau$$

$$\Delta F_0 = -15.0 + 3 \times 12 = 21 k_B T$$

Here the final value of the tension is  $\gamma(\tau) = 3 k_B T/\text{nm}^2$  and  $\Delta A$ , the membrane displayed area of activation ( $C \rightarrow O$ ), was taken to be  $12 \text{ nm}^2$  based on the molecular dynamics simulations of crystallographic structures of the closed and open states [195]. We used the molecular dynamics simulation estimate as our best guess for  $\Delta A$ , which is consistent with previous experimental studies [46,53,155,195]. With totally different techniques,  $\Delta F_0$  was also determined to be  $22 \pm 1 k_B T$  for MscS [195].

### **Discussion**

We extracted the free energy difference between the closed and open state of a mechanosensitive ion channel (MscS) in *E. coli*'s membrane from non-equilibrium work measurements performed in the patch clamp setup where the work parameter is the membrane tension,  $\gamma$ , and corresponding conjugate variable is the protein's lateral

area expansion,  $\Delta A$ . Various estimators are all in good agreement with each other and recover the free energy within  $k_B T$  of its best estimate obtained from an independent experiment. We considered the Bennett's acceptance ratio method as our best estimate for the free energy since it uses both of the work distributions associated with  $C \rightarrow O$  and  $O \rightarrow C$  transitions and it does not rely on binned histograms between the distributions. The general framework presented in this paper is not limited to MscS but is valid for all mechanosensitive ion channels that can be modeled as two-state systems. This condition can usually be met by a fast delivery of the membrane tension at the expense of irreversibility and dissipation, which does not pose a problem since non-equilibrium fluctuation theorems can still recover the free energy for the processes where  $W_{Diss} \leq 100 k_B T$  [74].

It has been long known that MscS - under prolonged stimulus of sub-saturating tensions - inactivates wherein it becomes non-conductive and insensitive to tension. Inactivation is a relatively slow process and takes place only under moderate tension values and requires tens of seconds to manifest [51,132]. Inactivation prevents data acquisition at slow enough rates to assume thermal equilibrium, thus, it is not feasible to estimate the free energy difference from the "reversible" work,  $W_{rev} \cong \Delta F$  for the channels that undergo inactivation. On the other end of spectrum, for the millisecond-range, machine-limited pulse protocols, the channels seem to display a faster gating scheme than what is observed under typical 1s ramp protocols [155]. We argue that this faster gating under machine-limited pulse protocols is an experimental artifact in the excised patch configurations as it is absent in the whole cell mode [46]. Revealed by high-resolution video microscopy, the



radius of curvature of the patches saturates and becomes constant in the range of suction where the channels are active [130]. Therefore, the law of Laplace establishes a linear relation between the tension in the membrane and the pressure across it and it has been experimentally verified both in whole cell and excised patch configurations under ramp stimuli [46,130,131]. However, for the machine-limited pulse protocols, the patch curvature might not reach saturation fast enough giving rise to a higher absolute tension in the membrane. For the reasons mentioned above, the time and tension scale of stimulus need to be carefully chosen such that the channel can be well described as a two-state system and the absolute tension in the membrane follows the law of Laplace. In order to address these concerns, we have made a Markov chain simulation of the two-state model with the parameters provided in the SI. Using the experimental protocol as stimulus, the work distributions obtained from the two-state model simulation gave a very close  $\Delta F_0$  ( $21.7 k_B T$ ) to the experimentally obtained  $\Delta F_0$  ( $21 k_B T$ ) validating that we have worked in the two-state regime (see Supplementary Fig. S5).

It is also worth mentioning that even though the work parameter (the membrane tension) changes as a function of time according to a predefined protocol, in principle it should not respond to the state of the system, namely it should not fluctuate and should be identical in each realization of the protocol. This criterion can only be satisfied in simulation or theory. This problem is not unique to our setup. It appears as well in single molecule pulling experiments [196–198], where the work parameter is the molecular extension of the system or the force calibrated from the displacement of the bead in a trap. Neither of these parameters is exactly the same for

each repetition of the experiment due to different response of the pulled molecule, thus, the assumption that these parameters are controlled is an approximation [199]. By the same token, the work parameter in the patch clamp experiment is not immune to fluctuations. Therefore, in any experimental setup, extra care should be taken to ensure that the work parameter is properly chosen such that the fluctuations are negligible. In Supplementary Fig. S6, we compared the work distributions and free energy difference obtained from two separate membranes having different number of MscS channels. A good reproducibility has been observed among different membranes under the same protocol. Moreover, we tried a different protocol where the membrane tension was increased to  $3.6 k_B T/nm^2$  in 250 milliseconds giving a different  $\Delta F$ . As a control experiment, regardless of the final value of the work parameter or the rate,  $\Delta F_0$  should always be retrieved from  $\Delta F_0 = \Delta F + \gamma \Delta A|_0^\tau$  since the boundary term compensates for the difference in  $\Delta F$  (see Supplementary Fig. S7 and Table-2). It is also important to note that the framework developed in this paper can still recover  $\Delta F_0$  for the channels where  $\Delta A$  is not known in advance. If we repeat the measurements for different values of  $\gamma_\tau$ , the change in  $\Delta F$  with respect to  $\gamma_\tau$  reveals  $\Delta A$ , which can then be used to retrieve  $\Delta F_0$  as shown above or in SI.

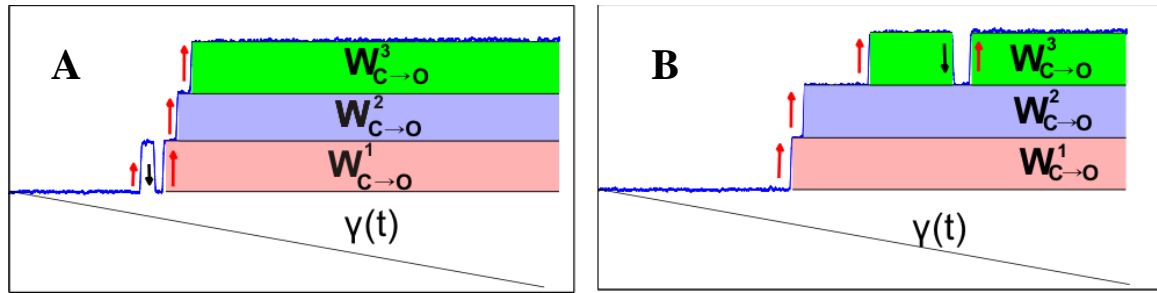


**Figure 4.5. An inevitable complication due to indistinguishability of single channel events in the patch clamp experiments.** Gating of 3 MscS channels in response to linear increase in the membrane tension is depicted. For the sake of simplicity, assume that  $\Delta A = 1 \text{ nm}^2$ , therefore the shaded areas represent the work done during the gating. The transient opening (A) and closing (B) events denoted by the red and black arrows lead to an error that is proportional to the area between the arrows. More specifically, the work done for the one of the channels in (A) is underestimated whereas in B, overestimated by an amount corresponding the area between the red and black arrow. This error still lies within experimental uncertainty and can be neglected compared to typical work values obtained from the shaded areas.

It is an experimental advantage to have as many channels as possible, since each single channel event yields an independent work value for every realization of the experimental protocol. Yet, many channels come with two inevitable complications inherent in all patch clamp experiments. (i) To use the proposed method single channel events must be resolved. This becomes increasingly difficult when there are many channels in the same patch. Therefore, we expressed MscS in a tightly regulated PBAD expression system in order to control channel expression (ii) If a channel changes its state more than once, the path it follows,  $\{\sigma_k; 0 \leq k \leq M\}$ , cannot be determined precisely for the rest of the protocol, since the single channel events are indistinguishable in the patch clamp setup. Fig. 4.5A demonstrates an example of the second complication where the work associated with the transient gating of a channel in the beginning of the experiment might belong to any of these

three channels. Similarly, in Fig. 4.5B, one of the channels at the end of the protocol briefly changes its state from open to closed as shown by black and red arrows. If such events, although not very common, happen in the beginning or at the end of the protocol, the error introduced will not be significant as the area between the red and black arrows is negligible compared with the typical area that gives the work values. Despite this unavoidable complication, the patch clamp technique is still quite advantageous and offers fast convergence as enough statistics for the work distributions can be collected efficiently.

## **Material and Methods**

### **Preparation of giant spheroplasts and patch clamp**

The giant spheroplasts of *E. coli* were prepared following the protocol described in [40]. 3 ml of the colony-derived culture was transferred into 27 ml of LB containing 0.06 mg/ml cephalixin, which selectively blocks septation. After 1.5-2 hours of shaking in the presence of cephalixin, 100-250  $\mu\text{m}$  long filaments formed. Toward the end of the filamentous growth stage, induction with 0.001 % L-Arabinose was done for 10-20 mins which gave 1-15 channels per patch. The filaments were transferred into a hypertonic buffer containing 1 M sucrose and subjected to digestion by lysozyme (0.2 mg/ml) in the presence of 5 mM EDTA. As a result, filaments collapsed into spheres of 3-7  $\mu\text{m}$  in diameter in 7-10 mins. The reaction was terminated by adding 20 mM  $\text{Mg}^{2+}$ . Spheroplasts were separated from the rest of the

reaction mixture by sedimentation through a one-step sucrose gradient.

Borosilicate glass (Drummond 2-000-100) pipets 1-1.3  $\mu\text{m}$  in diameter were used to form tight seals with the inner membrane. The MS channel activities were recorded via inside-out excised patch clamp method after expressing them in MJF641. The pipette solution had 200 mM KCl, 50 mM  $\text{MgCl}_2$ , 5 mM  $\text{CaCl}_2$ , 5 mM HEPES. The bath solution differed only in the addition of 400 mM Sucrose. Both pipette and bath solution had the pH of 7.4. Traces were recorded using Clampex 10.3 software (MDS Analytical Technologies). Mechanical stimuli were delivered using a high-speed pressure clamp apparatus (HSPC-1; ALA Scientific Instruments).

### **Tension Calibration**

The pressure (P) was converted to the tension ( $\gamma$ ) using the following relation:  $\gamma = (P/P_{0.5})\gamma_{0.5}$  assuming the radius of curvature of the patch does not change in the range of pressures where the channels were active ( $P > 40$  mmHg) and the constant of proportionality between tension and pressure is  $\gamma_{0.5}/P_{0.5}$  [46,130,131]. The midpoint tension,  $\gamma_{0.5}$  of MscS was taken to be 7.85 mN/m [46].  $P_{0.5}$  represents the pressure value at which half of the population is in the open state and was determined from the averages of 5-10 traces obtained by using 1-s triangular ramp protocols at the beginning of each experiment.

### **Acknowledgments...**

UC was supported by the U.S. Department of Education GAANN “Mathematics in Biology” Fellowship. OR is supported by a research grant from Mr. and Mrs. Dan Kane and the Abramson Family Center for Young Scientists. The work was

supported by NIH R21AI105655 and GM107652 grants to SS. CJ acknowledges financial support from the National Science Foundation (USA), under grant DMR-1506969. UC thanks Ms. Stephanie Sansbury for cloning MscS into tightly-regulated pBAD for expression system and Dr. Andriy Anishkin for the illustrations in Fig. 1 & 2. UC is also indebted to Dr. Yiğit Subaşı for the stimulating discussions.

## **Chapter 5: General conclusions and future directions**

### *Conclusion 1*

Cellular dynamics such as division and growth of cells are closely connected to changes in cellular volume, pressure and shape. Therefore all living organisms carefully regulate their internal ionic concentration and water content in response to environmental changes. Especially, most opportunistic pathogens that are transmitted through soil and fresh water show exceptional adaptability to drastic osmolarity changes. This robust osmoregulation system requires biological machines like MS channels that can immediately respond to osmotic shocks and reduce excess turgor before it reaches a dangerous level for the cell. Even though there exists a vast amount of literature on the gating mechanism of individual bacterial MS channels (more than 500 papers published on MscS and MscL to date), there are almost no data on in vivo rate of swelling, the kinetics of osmolyte release, the molecules that escape through specific channels, when and how the transient permeability ceases, and finally, how these parameters are linked to cell viability. Our current analysis of microbial survival under extreme osmotic stress strongly suggests two key aspects: (i) the channels must release osmolytes fast enough to outpace the osmotic water influx and limit cell swelling; (ii) the osmolyte efflux should also be terminated by inactivation of the low-threshold channels to facilitate the recovery phase. By utilizing a variety of experimental techniques and computations, in Chapter 2, we presented a comprehensive biophysical explanation of how microbes deal with extreme osmotic forces, what cellular parameters are crucial for survival, and what

determines environmental fitness for typical opportunistic pathogens such as *Pseudomonas aeruginosa*.

### Conclusion 2

The massive permeability response in *E.coli* is mainly mediated by two MS channels: MscS and MscL. Even though each channel can single-handedly rescue cells from abrupt osmotic down-shocks, cells rely on both channels to counter osmotic challenges. We hypothesized that each channel is specialized to fulfill a certain task in osmoregulation: MscS, which gates at non-lytic tensions, fulfills an “everyday” turgor relief for mild osmotic downshocks, whereas MscL, which opens at near-lytic tensions, acts as a true “emergency” valve by forming a large, non-selective pore in the membrane. The tension-induced inactivation mechanism of MscS, when considered together with its close cooperation with MscL, can be seen as a tandem effort to economize the loss of cellular contents under non-emergency conditions. In particular, for abrupt osmotic down shocks, both channels actively dissipate solutes and water until the tension is reduced to MscL’s activation threshold or below. At this stage, MscS channels are still fully open ( $P_{\text{open}} \sim 1$ ) and continue to reduce the tension well below their own activation midpoint before finally completely inactivating. Therefore, by fine-tuning the tension – first reducing it well below MscL’s activation threshold to prevent MscL’s opening and then completely inactivating– MscS channels minimize the unnecessary flickering of both channels into the open state. It has been also analytically verified that MscS inactivation is maximized at around the midpoint tension. Not surprisingly, this is the tension at which MscS spends equal time in the closed and open state displaying maximum flickering. For this reason, we



argued that the existence of a non-conductive, tension-insensitive (inactivated) state and the location of the inactivated state well on the energy landscape relative to other states are not coincidental but rather the result of a billion-year evolution to provide a more efficient and “economic” response to osmotic challenges. Thus MscS plays a major role in the osmotic adjustments and environmental stability of most bacteria.

#### Effects of compatible osmolytes and crowders on gating of MscS family channels

This part of the document contains data that are still in a phase of preparation for publication, yet merit to be presented and discussed. Along with the previous publication by Rowe et al. [200], these data strengthen the conclusion that MscS, with its crowding- and osmolyte-sensing cytoplasmic domain is a critical common component of the osmoadaptation machinery allowing for proper termination of the massive osmotic permeability response.

While MS channels are activated by tension in the cytoplasmic membrane, it is not clear whether only the tension release alone terminates the permeability response or if other parameters are involved. As previously shown, *E.coli* MscS (EcMscS) displays tension-driven inactivation when it is subject to moderate (non-saturating) tensions, however, the MscS paralog MscK, as well as, some other homologs such as MscCG from *Corinebacterium glutamicum* and MscSP from *Silicibacter pomeroyi* do not inactivate with tension even though they share a high degree of structural similarity. A number of studies have suggested that the hollow cytoplasmic cage domain, which is characteristic of the MscS superfamily, might serve as an intramolecular (special) osmotically active compartment [200,201]. Since

different states exclude different volumes to cage-inaccessible solutes, the rates of closure and inactivation can be altered in the presence of molecular crowding.

Recently, we started comparing the effects of different osmolytes on EcMscS and found the inverse correlation between their ability to drive the channel into inactivation and permeability through the cytoplasmic portals assessed in MD simulations.

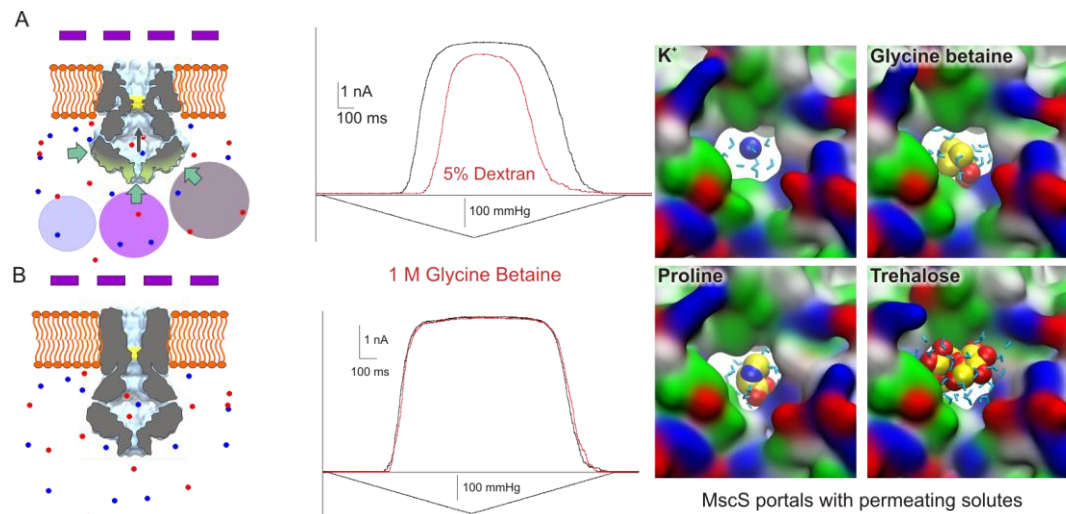


**Figure 5.1. Size dependent effect of crowding agents on the gating properties of the EcMscS channels.** (A) Cartoon showing that for big molecules that cannot penetrate through the cytoplasmic cage region of the channel the difference between the chemical potentials of water molecules inside and outside of the cage creates an osmotic pressure acting on the cytoplasmic domain of the channel. Since the closed  $\rightarrow$  open transition is also accompanied by the expansion of the cytoplasmic cage domain, this expansion, in the presence of cage inaccessible big molecule, comes with an extra work term in order to open the channel. This extra work term favors the closed state as it excludes less volume to crowding agent and results in a right shift in the open probability of the channels. (B) For ions and relative small solutes that are free to pass through the cage portals and equilibrate, there is no net osmotic pressure action on the cage thus the transition rates stay the same. (C) MD simulations demonstrate that small molecules such as ions, Glycine Betaine and Proline can pass through the EcMscS portals whereas trehalose is expected to partially permeate through the cage. Therefore, the cage region would be inaccessible to the molecules that are bigger than trehalose.

The origin of the non-specific interaction between crowding agents and EcMscS, which favors the closed and inactivated states of the channel, arises from the expansion of the cytoplasmic cage domain of EcMscS upon gating [202]. In the presence of large macromolecules that cannot penetrate through MscS's cage, the difference between the chemical potential of water molecules inside and outside of the cytoplasmic cage gives rise to a net osmotic pressure,  $\Pi_{\text{osm}}$  acting on the cage domain [203,204]. Since the open conformation of EcMscS channel excludes more volume ( $\Delta V$ ) to cage-inaccessible solutes than the closed conformation, there is an extra energy penalty term,  $\Pi_{\text{osm}}\Delta V$  that needs to be paid to open the channel in the presence of molecular crowding [205,206]. This extra energy term results from the work done against the osmotic pressure ( $\Pi_{\text{osm}}$ ) exerted by the macromolecules as the channels cage expands upon gating. As demonstrated in Fig.5.1.A, when cage-inaccessible (large) dextran molecules were introduced in the cytoplasmic side of the channels, the channels required more tension to gate and the open probability shifted toward higher pipette pressures. Moreover, the rate of closure was accelerated meaning that more channels were found in the closed state at any given constant tension. On the other hand, for relatively small molecules such as ions and Glycine Betaine that can freely diffuse through the cage and equilibrate, the chemical potential of water is the same both inside and outside of the cage and the expansion of the cage domain during the gating does not cost extra energy. Therefore, the open probability stayed the same in the presence cage-penetrable molecules (Fig. 5.1.B). In accordance with the molecular dynamic simulations that probed the permeability of various crowding agents into the cytoplasmic cage of MscS channels (Fig. 5.1.C), we

found that for the molecules that can freely diffuse through the cage, there is no significant change in the transition rates for the channel gating. However, in the presence of non-penetrating molecules, since the closed and inactivated states exclude less volume than the open state, molecular crowding favors these states. It is possible to estimate the extra energy term by monitoring changes in the transition rates in the presence of crowding agents [205]. The free energy difference between the open and closed state in the presence of molecular crowding can be written as follows [206,207]:

$$\Delta G(\gamma, \Pi_{osm}) = \Delta G(0,0) - \gamma\Delta A + \Pi_{osm}\Delta V \quad [1]$$

Where  $\Delta G(0,0) = \epsilon_{open} - \epsilon_{closed}$ , is the free energy difference between the open and closed state in the absence of both membrane tension ( $\gamma = 0$ ) and macromolecular crowding ( $\Pi_{osm}=0$ ). Since the osmotic pressure term increases the free energy difference, more tension needs to be applied in order to open the channels in the presence of molecular crowding. Assuming that the states are populated according to Boltzmann distribution at equilibrium [207,208], the open probability under osmotic stress becomes:

$$P_{open} = \frac{1}{1 + e^{\beta(\Delta G(0,0) - \gamma\Delta A + \Pi_{osm}\Delta V)}} \quad [2]$$

Therefore, the extra work term,  $\Pi_{osm}\Delta V$ , results in a right shift in the open probability curve. It is important to note that for small molecules that are free to penetrate through the cage and thus equilibrate ( $\Pi_{osm} = 0$ ) and for the channels that do not have any cytoplasmic cage domain (MscL family channels) or whose cage does not change volume upon transitions ( $\Delta V = 0$ ), there is no extra energy penalty

term and crowding should not affect the open probability unless there is a specific interaction between the crowding agent and protein.

We studied the effects of permeable and impermeable osmolytes on MscS homologs from gram-negative and gram-positive species and found similar correlations. Here, we only provide results for VcMscS-1 which is the closest MscS orthologue in the *Vibrio cholerae* genome (287 amino acid long, 48% overall identity with an 84% conserved TM3- $\beta$  domain region). However, we emphasize that macromolecular crowding induces similar effect on other MscS family channels. The manuscript is in preparation.

It is also important to note that even though MscS family channels from *Vibrio cholerae* can be inactivated by the tension in the native *Vibrio* membranes [96], when heterologously expressed in channel-free *E.coli* spheroplasts, *Vibrio* channels for some unknown reason did not inactivate under pulse-step pulse protocol (Fig. 5.2.G, n=7).

We suspect that the differences in lipid composition of two membranes might be one of the reasons why the channels do not inactivate. The effect of crowding agent on the dose response curves is shown in Fig. 5.2 A-C. The right shift of the activation curve towards higher pipet pressures and eminent increase in closing rates were the most common effects of crowding agents on the VcMscS-1 gating. Although VcMscS-1 do not inactivate by tension alone in *E.coli* membranes, the channels underwent drastic inactivation -indicated by the red arrows- when they were exposed to moderate amount of crowding agents such as Ectoine, Trehalose and Dextran as shown in Fig. 5.2 D-F. In particular, Figure 5.2 F shows that 90 % of the VcMscS-1

population was driven to the inactivation when they were sustained under sub saturating tension for 20 s under 15% Dextran.

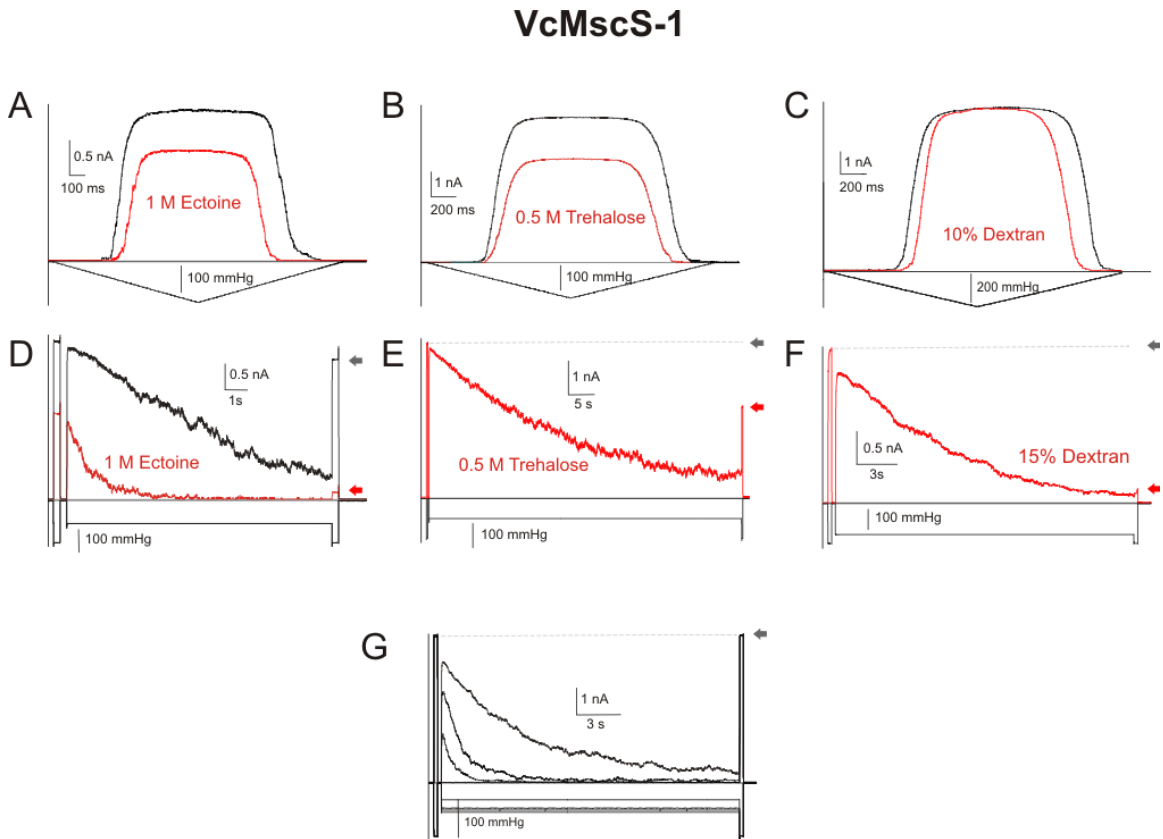


**Figure 5.2 VcMscS-1 activity under molecular crowding.** (A-C) 1s triangular ramp protocols were used to monitor the effect of crowding agents on the channels' gating profile. Under molecular crowding, more tension is required to gate the channels seen as the right shift of dose response curves toward higher pipette pressure (red traces). The partial inactivation of the channels prior to application of the experimental protocol and the decrease in the conductivity of the bath solution upon addition of crowding agents explain the decrease in overall saturating current. It should be noted when heterologously expressed in *E. coli* membrane, VcMscS-1 channels do not display any tension-induced inactivation even though the channels inactivate in their native membrane (G). The reason for the loss of the tension-induced inactivation mechanism in the *E. coli* membrane is unknown yet the channels can still be inactivated under molecular crowding (D-F).

We also tested the effects of large crowders on gating of MscL and found that unlike MscS-like channels, MscL channels were totally insensitive to the molecular crowding as expected (Fig.5.3). Since MscL cage neither changes its volume upon gating ( $\Delta V = 0$ ), the presence of crowding agents does not change the gating dynamics. This result strongly suggests that the cage domain in MscS family channels might behave as an osmotically active compartment and is also sensitive to excluded volume effects. Increase of cytoplasmic crowding as a result of osmolyte and water release is a potent terminating factor likely acting through common cytoplasmic cage domains.

Monitoring the activity of mechanosensitive channels in the presence of crowding agents might help us understand how MS channels function in their native environment and how natural transitions between open-closed-inactivated states can drastically be changed via crowding. Finding out that MscS-like channels display a crowding-induced inactivation in common might also answer many questions regarding their evolutionary roles. We conclude that inactivation of MscS-like channels driven by large osmolytes or crowding agents is a common mechanism in the family. It reflects the natural process of permeability response termination when water exits the cytoplasm together with small permeable osmolytes and the concentration (and excluded volume) of large molecules increases. This mechanism also prevents over-draining of the cytoplasm by disengaging the low-threshold channels when tension in the membrane drops far below lytic level.

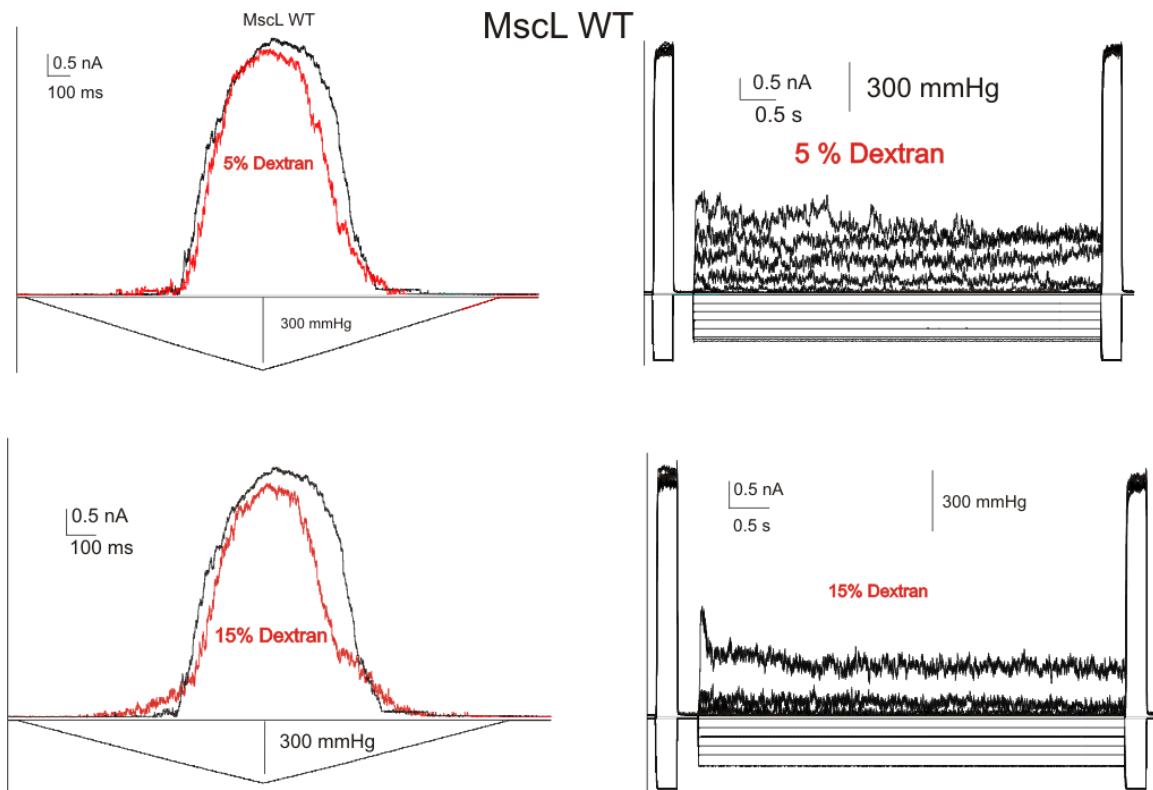


**Figure 5.3. MscL channels are insensitive to macromolecular crowding.** Unlike MscS channels, MscL channels do not have an osmotically active cage domain therefore addition of crowding agent does not cause any inactivation as hypothesized.

### Conclusion 3

For macroscopic systems where there are  $\sim 10^{23}$  degrees of freedom involved, the law of large numbers states that fluctuations are order of  $\sim 10^{-11}$ , in other words, fluctuations around the mean are negligible. Therefore, we never observe any significant deviation away from the ensemble averages and so thermodynamics works. For microscopic systems, however, large deviations from averages are now evident. It turns out that these fluctuations are not random background noise due to poor statistics ( $N \sim 1$ ) but rather they satisfy strong, yet unexpected relations.



Surprisingly, once these fluctuations are threaded properly, thermodynamic inequalities can be replaced by equalities.

In Chapter 4, we presented alternative and more reliable ways to obtain the free energy difference ( $\Delta F$ ) between the open and closed state of mechanosensitive ion channels by making use of recent developments in statistical physics. Our new approach bridges the gap between recent developments in non-equilibrium thermodynamics of small systems and ion channel biophysics. Our study also serves as an experimental verification of non-equilibrium work relations in a biological system. In addition, our study shows that a 1-s linear ramp stimulation represents the approximate dynamic boundary between equilibrium and non-equilibrium regimes of MscS operation. Our stopped-flow experiments at the same time indicate that under natural conditions of abrupt osmotic downshift MscS opens within 20 ms and therefore is stimulated in a highly non-equilibrium regime. Future studies will show whether this is an ‘imperfectness’ of a part of the well-tested (by the billion-year-long evolution) natural gating mechanism.

## Chapter 5: Supplement

### Tension-activated channels in the mechanism of osmotic fitness in *Pseudomonas*

#### *auriginosa*

Ugur Cetiner<sup>1,3,4</sup>, Ian Rowe<sup>1,2</sup>, Anthony Schams<sup>1</sup>, Christina Mayhew<sup>1</sup>, Deanna Rubin<sup>1</sup>, Andriy Anishkin<sup>1</sup> and Sergei Sukharev<sup>1,3,4</sup>

<sup>1</sup>Department of Biology, <sup>2</sup>Department of Chemistry and Biochemistry, <sup>3</sup>Institute of Physical Science and Technology, <sup>4</sup>Maryland Biophysics Program, University of Maryland, College Park, MD 20742

### Supplemental Material

#### Intensity of light scattering by bacterial suspension

Light scattering is a flexible tool with excellent time resolution that allows us to observe the time course of bacterial responses to osmotic stresses. The directional intensity of the scattered light depends on multiple factors including experimental setup, the shape of bacterial cells, and cytoplasmic composition. For a suspension of *E. coli*, light scattering can be described by the Rayleigh-Gans approximation (Koch et al., 1996):

$$I = \frac{8\pi^4 r^6 \eta_0^4}{R^2 \lambda^4} \cdot \frac{\left[\left(\frac{\eta}{\eta_0}\right)^2 - 1\right]^2}{\left[\left(\frac{\eta}{\eta_0}\right)^2 + 2\right]^2} \cdot \nu I_0 V [1 + \cos^2(\theta)] \cdot P(\theta) \quad (1)$$

where  $I$  is the intensity of the scattered light for a given direction and distance;  $r$ , the radius of the spherical equivalent of the actual particle (in our case, a rod-shaped bacterium);  $\eta_0$ , the index of refraction of the suspending medium;  $\eta$ , the index of refraction of the particle;  $V$ , the volume illuminated;  $I_0$  the intensity of the incident light;  $\nu$ , the concentration of particles;  $\theta$  the angle of observation;  $R$  the distance of the detector from the sample; and  $\lambda$ , the wavelength of light in vacuum. The factor  $[1 + \cos^2(\theta)]$ , depends on the angle of observation,  $\theta$ , relative to the forward direction of the illuminating beam. For a given physical setup, most of these factors can be combined into an empirical constant.  $P(\theta)$  is a correction function that compensates for the light interference within the particle and depends on the geometry of the scattering particle. For an ellipsoid of revolution, it is approximated as:

$$P(\theta) = (3(\sin x - x \cos x)/x^3)^2 \quad (2)$$

where

$$x = \left(\frac{4\pi a}{\lambda'}\right) \left(\sin \frac{\theta}{2}\right) \left(\sin^2 \beta + \left(\frac{b}{a}\right)^2 \cos^2 \beta\right)^{\frac{1}{2}} \quad (3)$$

$\beta$  is the angle of orientation of the ellipsoid of revolution to the direction of the light beam,  $a$  is the rotation radius of ellipsoid, and  $b/a$  is the ratio of the major to minor axis (Koch et al., 1996). To determine the amount of scattered light falling onto the detector, the equation with the substitutions should be integrated over the angular range covered by the detector and averaged over random orientations ( $\beta$  angles) of the ellipsoids in 3D space.

To enable quantitative estimation of the bacterial properties from the scattering traces, the intensity equation needs to be configured to match the specific parameters of the experimental setup (scattering angle, distance, amplification, background reflected lighting, etc.) (Foladori et al., 2008; Koch et al., 1996).

According to the equations above, the intensity of scattering is a function of several parameters characterizing the geometric and optical properties of the bacteria, primarily the size and the refraction index. The refraction index of a bacterium depends on concentration and nature of solutes in the cytoplasm. For our purpose of studying the role of MscS in bacterial response to hypoosmotic shock, all molecular species can be divided into two broad categories – permeable (ions and other low molecular weight solutes that can exit through MscS or MscL) and impermeable (proteins, nucleic acids, etc.). It has been shown (Ball and Ramsden, 1998; Craig et al., 1995) that contributions of both small solutes and macromolecules to the refraction index of solution scale linearly with their concentrations. If the bacterial cytoplasm is approximated as a uniform solution of all internal components, its refraction index can be estimated as:

$$\eta = \eta_w + \frac{d\eta}{dC_p} C_p + \frac{d\eta}{dC_i} C_i = \eta_w + \left( \frac{d\eta}{dC_p} m_p + \frac{d\eta}{dC_i} m_i \right) / V_c \quad (4)$$

where  $\eta$  is the refraction index of the cytoplasm,  $\eta_w$  refraction index of water,  $C_p$  and  $m_p$  are the concentration and total mass of the permeable species,  $C_i$  and  $m_i$  are those of impermeable species in the solution respectively, and  $V_c$  is the total volume of the bacterial cytoplasm.

Because the purpose of the current study is to estimate membrane permeability during osmotic shock, here we focus on the time course of the relative change in the cytoplasm volume and internal content rather than absolute quantification of the optical properties. From this viewpoint, the equation for the intensity of the captured scattered light can be rewritten to separate the terms that are essentially constant from the time-dependent variables:

$$I_r = I_b + Ar^6 \cdot \frac{\left[ \left( \frac{\eta_w + 3(S_p m_p + S_i m_i) / 4\pi r^3}{\eta_0} \right)^2 - 1 \right]^2}{\left[ \left( \frac{\eta_w + 3(S_p m_p + S_i m_i) / 4\pi r^3}{\eta_0} \right)^2 + 2 \right]^2} \quad (5)$$

Here  $I_r$  is the intensity of the recorded scattered light,  $I_b$  is the background light component,  $r$  is the radius of the spherical equivalent of the bacterium,  $\eta_w$  is the refraction index of water,  $\eta_0$  is the refraction index of extracellular medium,  $m_p$  and

$m_i$  are the masses of the permeable and impermeable solutes respectively,  $S_p$  and  $S_i$  are the scaling coefficients between their concentrations and contributions to the refraction index of the medium ( $S_p = d\eta/dC_p$ ,  $S_i = d\eta/dC_i$ , see equation 4) and  $A$  is the scaling coefficient for the amplitude of the scattered light that combines components for the instrumental amplification ( $A_i$ ), system geometry, angular dependence (should be integrated over the range of detection angles), light intensity etc. (notation as in the equations above):

$$A = A_i \frac{8\pi^4 \eta_0^4}{R^2 \lambda^4} \cdot \nu I_0 V \int_{\theta_{min}}^{\theta_{max}} P(\theta) [1 + \cos^2(\theta)] \sin(\theta) d\theta \quad (6)$$

Strictly speaking, the parameter  $P(\theta)$  under the integral is time-dependent as it includes the axial parameters of bacterial shape (see equations 2 and 3), which may change during the osmotic response (swelling/shrinkage). However, considering the light detector we use, and the relatively dense suspension of bacteria which causes multiple scattering events and smearing of the angular intensity peaks, the integrated value for the angular dependence should not change significantly with time. During the osmotic downshock two of the variables in equation 5 will undergo quick changes: the effective radius of the bacterium ( $r$ ) and the mass of permeable osmolytes that are confined within the cells ( $m_p$ ). The rest of the entries in the equation can be considered nearly constant. Soon after mixing/dilution bacteria swell and reach their maximum size; after that moment the cell geometry remains relatively stable. While osmolytes are escaping through mechanosensitive channels, the changes in the scattered light intensity are defined mostly by the mass of permeable osmolytes remaining inside the cell. Light scattering at this point is roughly proportional to the square of solute mass inside the cell. In the case of moderate osmotic shrinking (osmolytes remain in the cell while water is being lost), the intensity of light scattering scales as  $(1/r^2)$ , i.e., inverse to the cell surface area, or as volume to the power of  $-2/3$  (Koch, 1961).

The above analysis indicates that in the course of osmolyte efflux the refractive index difference between the cell and its environment is the major parameter with a strong dependence on time. In assumption that the cell volume changes are small, the time course of the scattering signal can be presented in the following form:

$$I = I_0 + S(m_i + m_p(t))^2,$$

where  $I$  is light intensity,  $I_0$  is background light intensity,  $S$  is scaling coefficient,  $m_i$  is mass of impermeable osmolytes, and  $m_p(t)$  is mass of permeable osmolytes as a function of time  $t$ . In the assumption that the efflux is proportional to the internal concentration (under the conditions of much lower external osmolarity)

$$\frac{dm_p}{dt} = -\frac{m_p}{\tau},$$

we may define  $\tau$  as the time constant of the permeable osmolyte release.

$$\frac{dm_p}{m_p} = -\frac{dt}{\tau}$$

$$\int \frac{1}{m_p} dm_p = \int -\frac{1}{\tau} dt$$

$$\ln m_p - \ln m_{p0} = -\frac{t}{\tau} + \frac{t_0}{\tau},$$

where  $m_{p0}$  is the initial mass of the permeable osmolytes before the release, and  $t_0$  is the time at which the exponential release has started.

$$m_p = m_{p0} e^{\frac{t_0-t}{\tau}}$$

$$I = I_0 + S(m_i + m_{p0} e^{\frac{t_0-t}{\tau}})^2$$

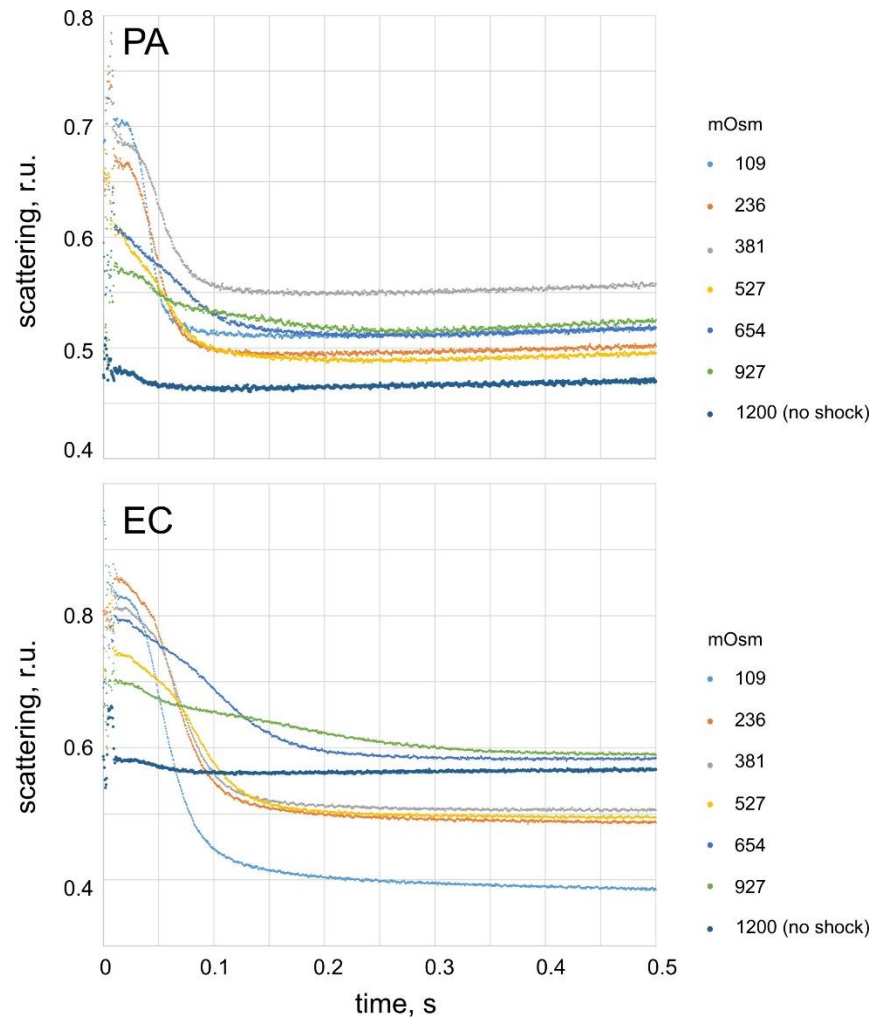
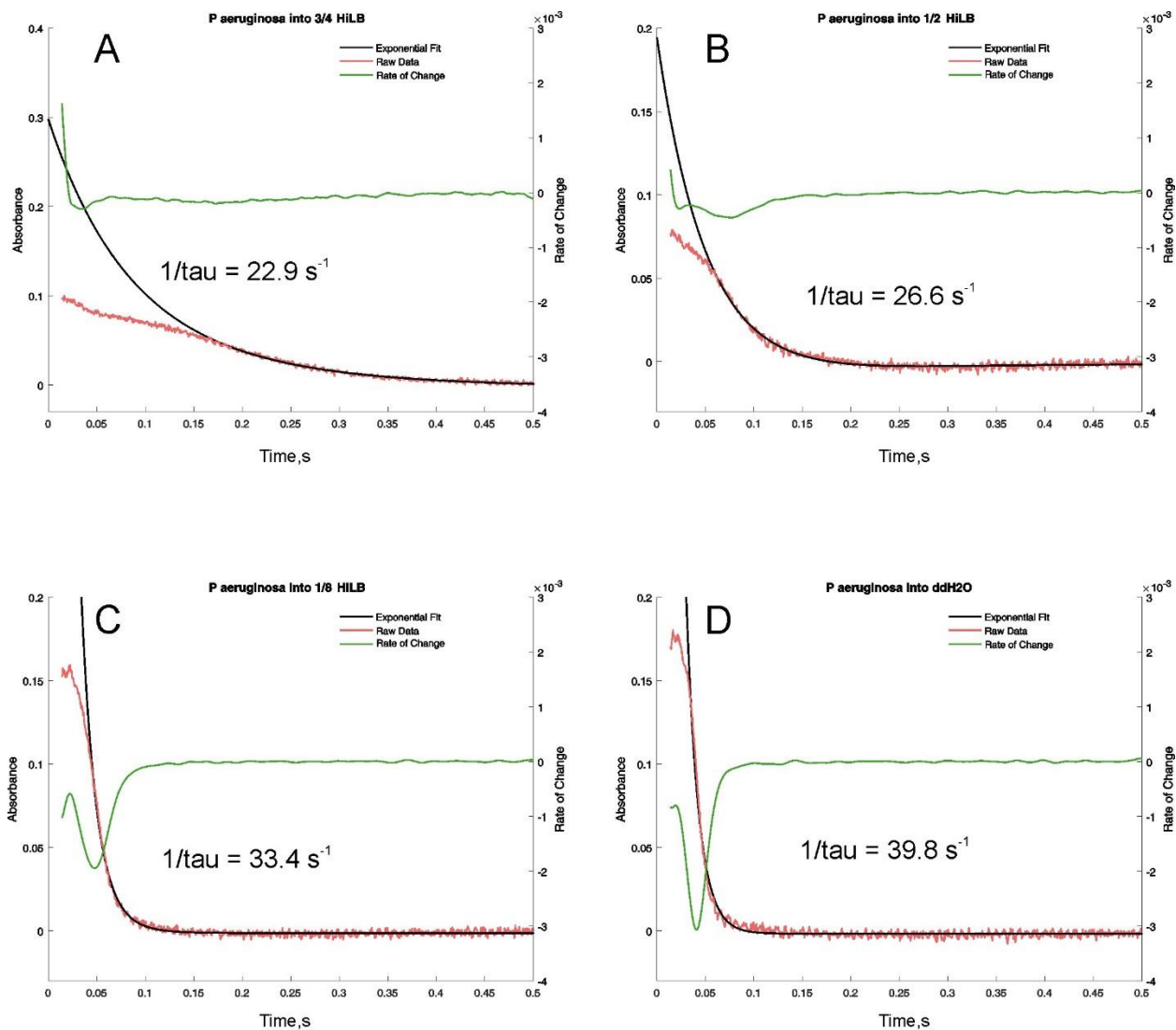
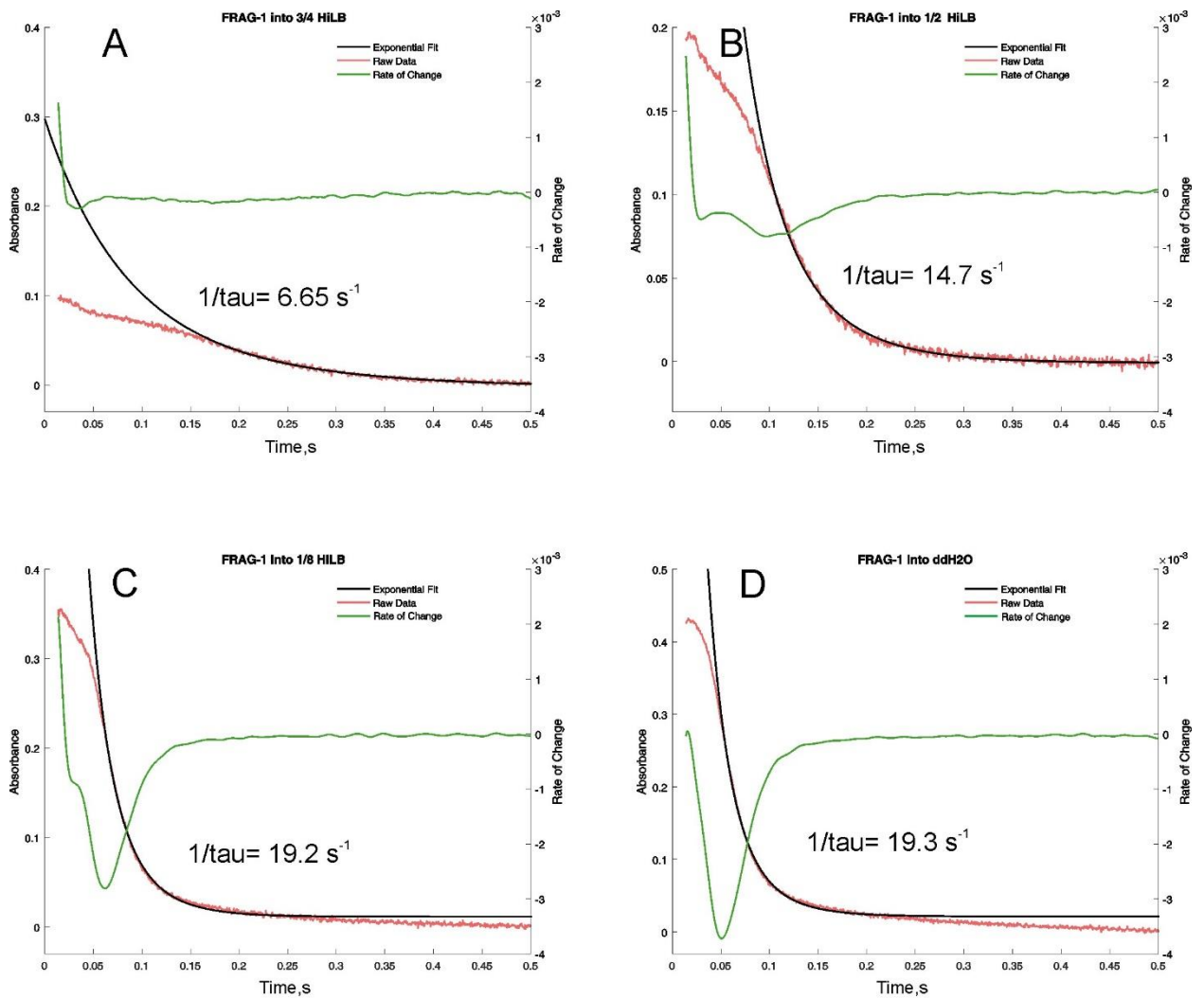


**Figure S1.** Unadjusted stopped-flow scattering traces obtained after subtraction of stray light signal. Initially, the cultures were grown in HiLB (1200 mOsm) to OD600 of 0.25, concentrated to OD600 of 2.2 and subjected to various down-shocks in the stopped-flow machine. On the right, values of end-point osmolarities are shown with color code for respective traces. The dark blue line represents the no-shock mixing control. The upper and lower graphs show experiments with PA-14 and Frag-1 strains, respectively. The deviation of no-shock (control) traces from straight line reflect possible response to shear stress.



$$I_0 + S \cdot (m_i + m_p \cdot \exp(-(t_0 - t)/\tau))^2$$

**Figure S2.** Examples of fitting curves (black) overlaid with experimental traces (red) obtained with PA-14 cultures shocked from HiLB to 3/4 HiLB (A), 1/2 HiLB (B), 1/8 HiLB (C) and distilled water (D). To obtain a maximal rate of release, fitting in most cases started at the point of steepest downfall designated by the minimum of a first derivative (green). Before fitting, the traces were adjusted such that at  $t = 0.5 \text{ s}$  the scattering signal was zero. Fitting was done in Matlab using the equation at the bottom.



$$I_0 + S^*(m_i + m_p * \exp(-(t_0 - t)/\tau))^2$$

**Figure S3.** Examples of fitting curves (black) overlaid with experimental traces (red) obtained with EC (Frag-1) cultures shocked from HiLB to 3/4 HiLB (A), 1/2 HiLB (B), 1/8 HiLB (C) and distilled water (D). As previously, fitting in most cases started at the point of steepest downfall designated by the minimum of a first derivative (green). In contrast to PA, a slow component was observed in EC traces as deviation between the experimental and fitting curves.



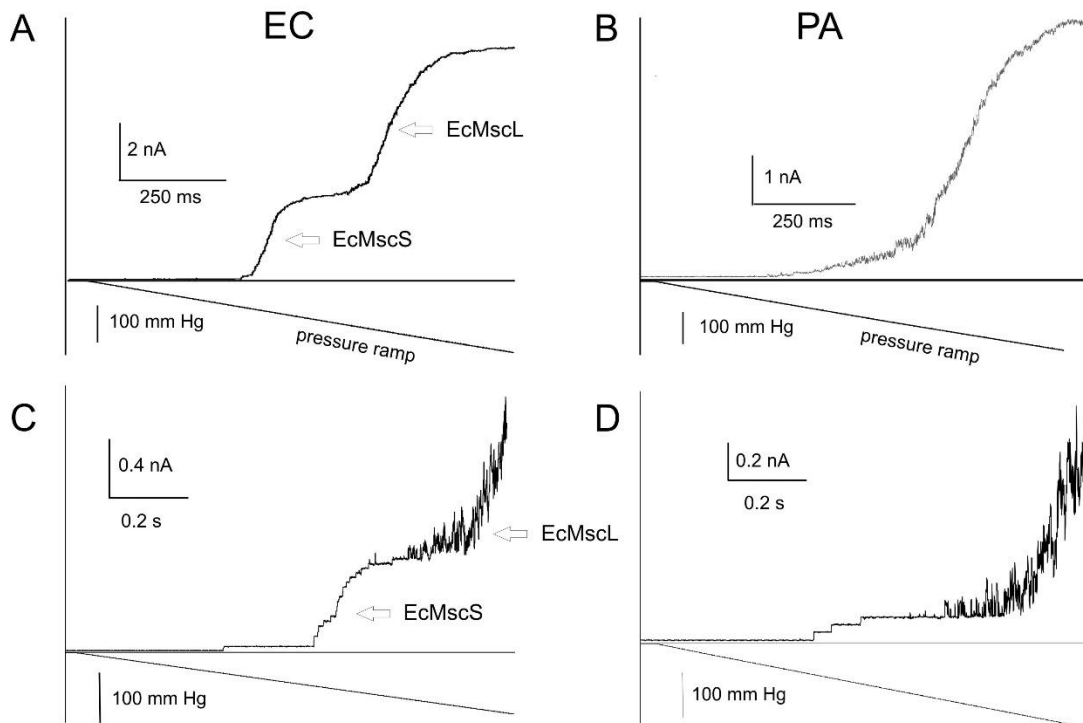


**Figure S4.** Pressure ramps applied to excised patches of EC (A, C) always reveal a larger MscS population as compared to PA (B, D). In the latter case it is not always possible to count individual channels as the current raises gradually and shows no obvious two-wave character. These traces in C, D represent clear cases when the MscS- and MscL-like channels can be easily separated and counted. 12 successful patches from *P. aeruginosa* and 9 patches from Frag-1 strain permitted quantification of channel density in these organisms (Table 1, main text)

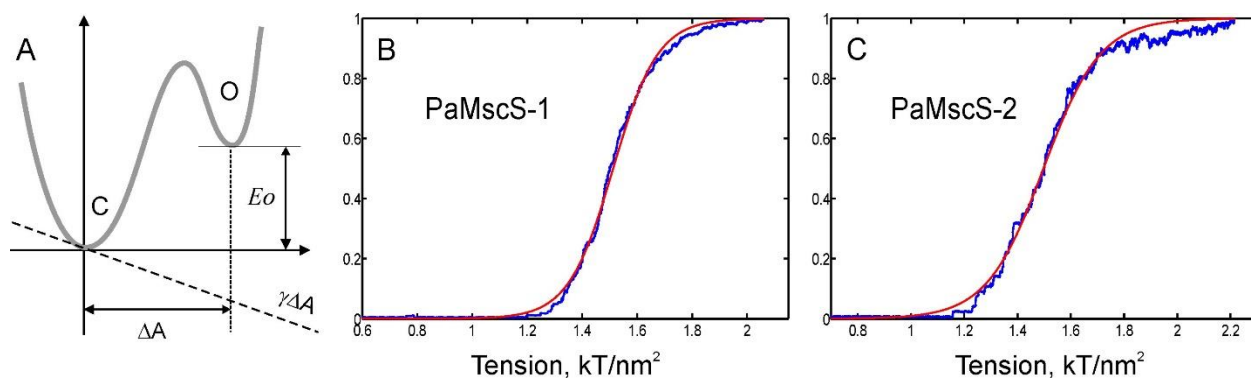


**Figure S5.** A two-state energy diagram for a tension-gated channel. (B, C) Open Probabilities ( $P_0$ ) plotted as a function of tension ( $\text{kT}/\text{nm}^2$ ) for PaMscS-1 (A) and PaMscS-2 (B).  $P_0$  was fitted to two state boltzman function  $P_0=1/(1+\exp((\Delta E-\gamma\Delta A)/kT))$  and gating parameters were extracted from the fits (red curve). The parameters of energy  $\Delta E$  and in-plane expansion  $\Delta A$  are in the text.

**Table S1.** *Pseudomonas aeruginosa* PA-14 putative proteins homologous to known MS channel proteins of *Escherichia coli*. MscS has two homologs of comparable length designated as PaMscS-1 and PaMscS-2. MscK aligns well with a single putative ‘long MscS-family’ protein PA\_66400 (1118 residues). YjeP, which is an ortholog of MscK in EC, also aligns with PA\_66400, but the alignment with MscK is better. A shorter putative 807 residue protein PA14\_46240 aligns with YjeP with a 35% identity in the characteristic MscS region. YnaI does not seem to have a direct homolog in PA-14.

EC Protein	Length of EC protein (AA)	Closest PA ortholog	Predicted length of PA protein (AA)	% identity (BLAST)
MscL	136	PA14_61050 (PaMscL)	137	64
MscS	286	PA14_57110 (PaMscS-1) PA14_65040 (PaMscS-2)	278 283	36 29
KefA/MscK	1120	PA14_66400	1118	40
YbdG	415	PA14_19230	442	44
YbiO	741	PA14_67630	735	33
YjeP	1107	PA14_46240	807	35
YnaI	343	no homolog		

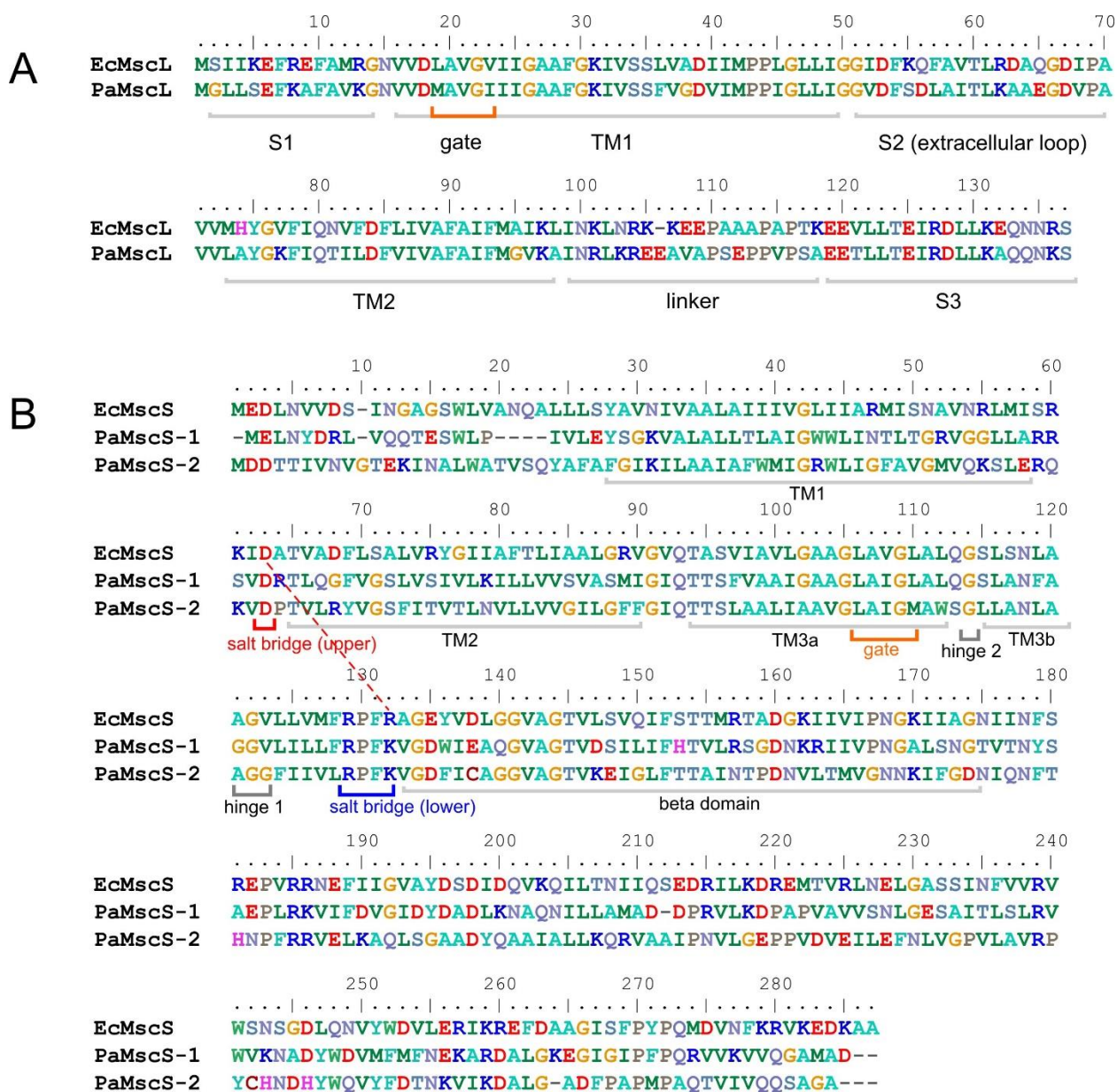


**Figure S6.** Alignments of *E. coli* and PA Msc channels orthologs. (A) Full sequence alignments of EcMscL and PaMscL. (B) Partial alignment of the core transmembrane segments of EcMscS with two PaMscS species, including the N-terminal part of the cage beta domain. The sequences predict the same position of the hydrophobic gate, salt bridges responsible for inter-domain interactions and all elements involved in inactivation, including double glycine motifs that made TM3 hinges (hinge 1) even more flexible than in EcMscS.

*Spatiotemporal relationships defining the adaptive gating of the bacterial  
mechanosensitive channel MscS*

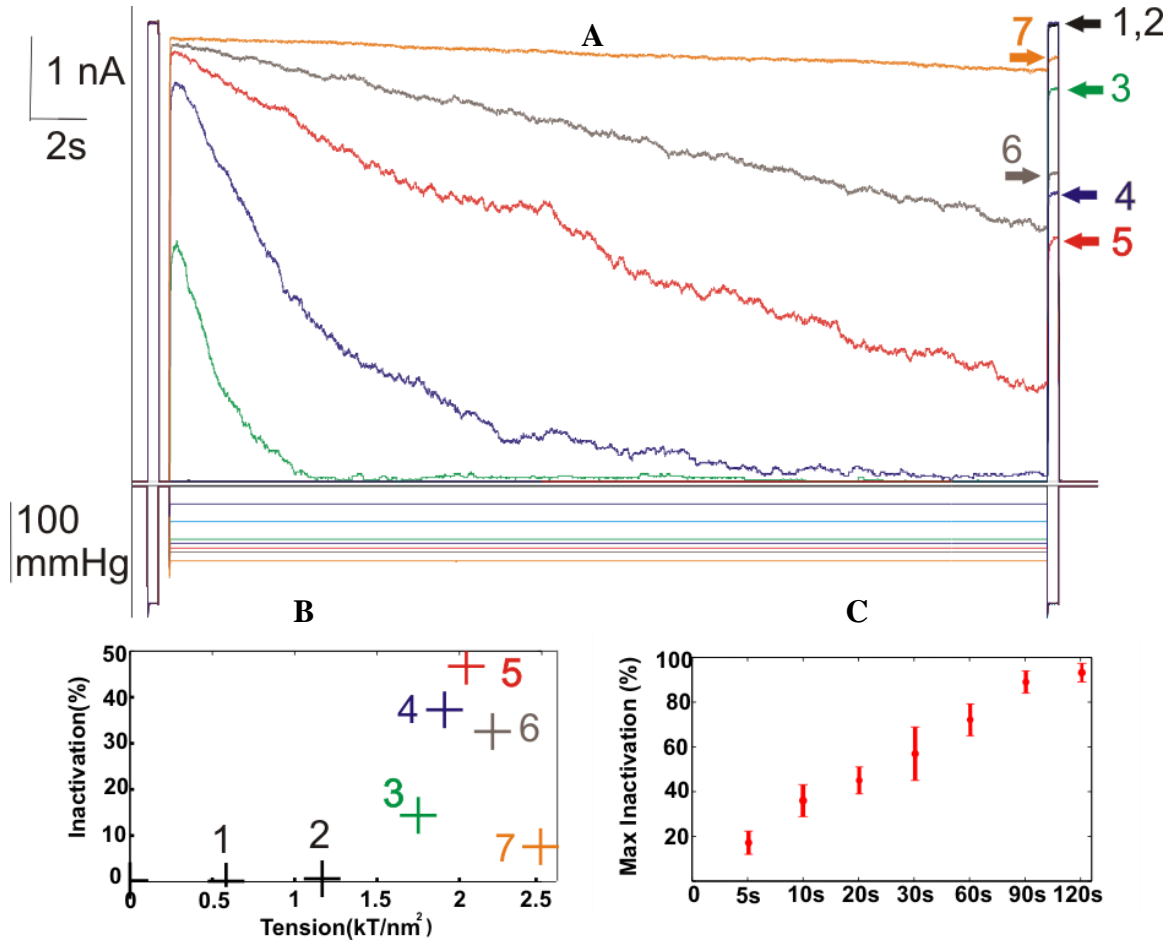


**Figure S1.** The characteristics of MscS inactivation observed in an excised patch containing approximately 200 MscS channels. A) Pulse-step-pulse protocol measures the extent of tension-driven inactivation by probing the number of active channels in the beginning and at the end of the process. An initial saturating pulse determines the total number of active channels in the membrane, followed by the application of prolonged steps of sub-saturating tensions that allows the channels to make transitions between the states. Since the channels in inactivated states are non-conductive and tension insensitive, the last saturating pulse at the end of the protocol reveals the number of channels populated in the inactivated state. B) Tension dependence of MscS inactivation obtained from Fig 1A in which the duration of sub-saturating tension was 20s. There is an optimum tension which maximizes the inactivation (5), tension values that lie below (1-2-3) or above (6-7) this point favor the closed or the open state respectively, thus decreasing the likelihood of being in the inactivated state. C) Inactivation is a relatively slow process. The amount of inactivation at maximizing tension increases with the time and becomes non negligible only if the specific range of tension values are employed for time scales longer than a few seconds.

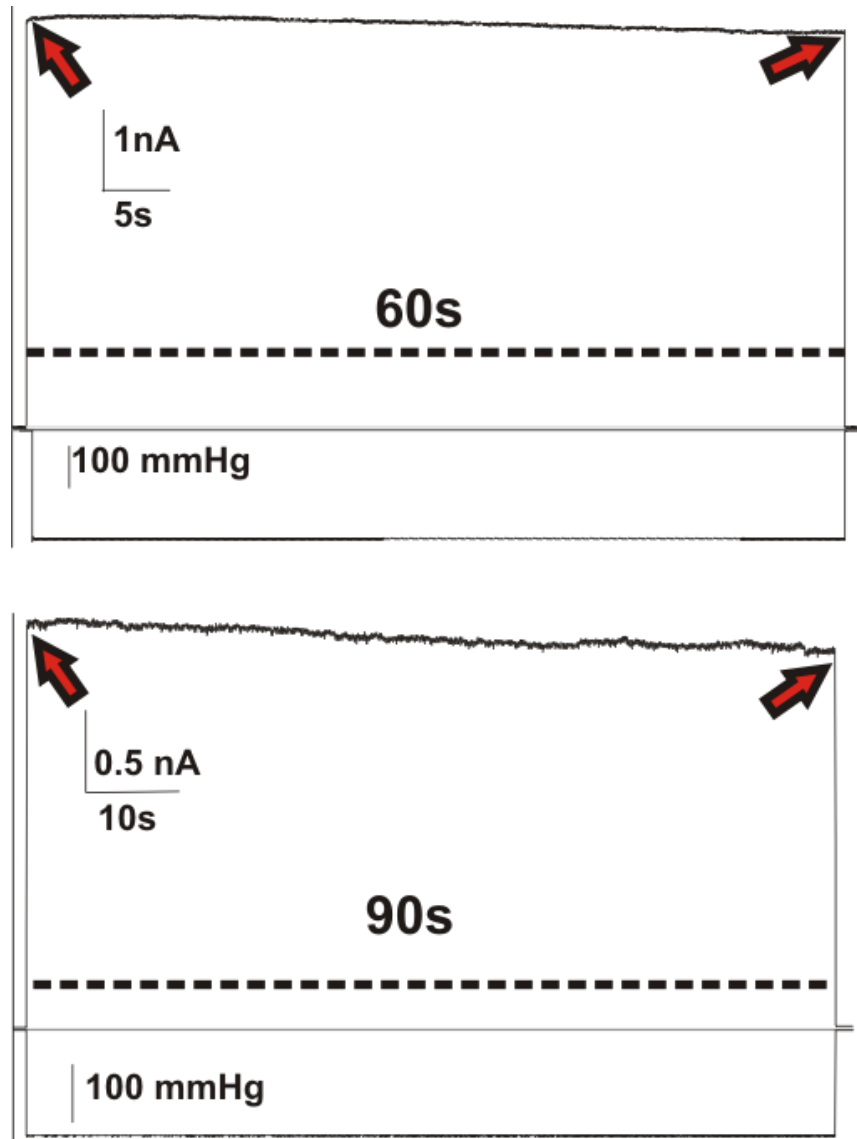


**Figure S2.** Locking the channels in the open state. The whole population of channels were conditioned in the open state by applying saturating tension at which the probability of finding a channel open,  $P_o \sim 1$ . The saturating tension was maintained for 60s and 90s. At the end of the processes, more than 95 % of the population stayed in the open state showing that there is practically no transition to the inactivated state from the open. Only the channels that are given a chance to close can make transitions to the inactivated state.

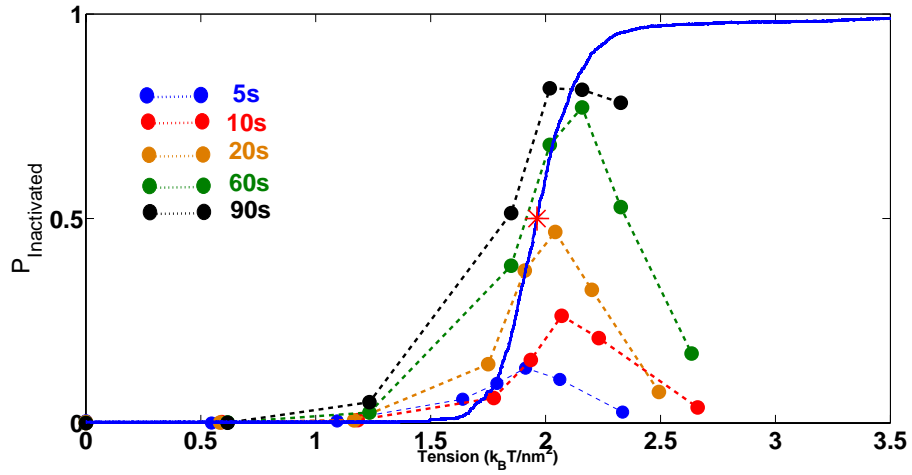


**Figure S3.** *E. coli* MscS inactivation as a function of time and tension measured by pulse-step-pulse protocol where the step duration was varied from 5s to 90s. There is a unique tension value that maximizes inactivation. Data points are the snapshots of the dynamics as the probability of being inactivated state approaches to its steady state value.

**On the convergence and uniqueness of the solution for the steady state/equilibrium distribution of states**

Below, we briefly discuss why finite-state irreducible Markov chains converge to a unique steady state. Since any Markov chain diagram can be represented in matrix a form (transition matrix), the Perron-Frobenius theorem for the positive matrices states the following:

Let  $K$  be real and  $N \times N$  matrix

$$\begin{aligned} K\vec{u} &= \lambda\vec{u} \\ \vec{v}K &= \lambda\vec{v} \end{aligned} \quad [1]$$

where  $\vec{u}$  and  $\vec{v}$  are the right and the left eigenvectors and  $\lambda$  is the eigenvalue of  $K$ .

Case 1.  $K=K^T$

- All eigenvalues are real.
- Left and right eigenvectors are identical and real.
- There are  $N$  eigenvector forming a complete set.
- $K$  is diagonalizable.

Case 2.  $K \neq K^T$

- If the eigenvalues are not degenerate, there are  $N$  eigenvectors.
- Left and right eigenvectors form a complete set but they are not identical.
- $K$  is diagonalizable.

Case 3.  $K \neq K^T$

- In case some of the eigenvalues are degenerate, if there can still be found  $N$  independent eigenvectors,  $K$  is diagonalizable. Otherwise not.

Moreover, in general for the transition rate matrices we have the following relations:

$$\frac{d\vec{p}}{dt} = R\vec{p} \Rightarrow \vec{p}(t) = e^{Rt}\vec{p}(0) \quad [2]$$

where  $\vec{p}$  is the probability vector and  $R$  is the transition rate matrix: Assuming  $R$  is diagonalizable, it can be written as  $R = UDV$ :

$$R = \begin{bmatrix} \vdots & \vdots & \cdots & \vdots \\ u_1 & u_2 & \cdots & u_N \\ \vdots & \vdots & \cdots & \vdots \end{bmatrix} \begin{bmatrix} \lambda_1 & 0 & \cdots & 0 \\ 0 & \lambda_2 & \cdots & 0 \\ \vdots & \vdots & \ddots & \vdots \\ 0 & 0 & 0 & \lambda_N \end{bmatrix} \begin{bmatrix} \cdots & v_1 & \cdots \\ \cdots & v_2 & \cdots \\ \cdots & \cdots & \cdots \\ \cdots & v_N & \cdots \end{bmatrix}$$



Where  $u$  and  $v$  are the right and the left eigenvectors of  $R$  defined as in [1]. If we define  $T(t) = e^{Rt}$ , it can be written as a summation:

$$T(t) = e^{Rt} = \sum_{n=0}^{\infty} \frac{(Rt)^n}{n!} = I + Rt + \frac{(Rt)^2}{2} + \dots$$

and taking the advantage of  $R=UDV$ , we get the following expression for  $T$ :

$$\begin{aligned} & \begin{bmatrix} \vdots & \vdots & \dots & \vdots \\ u_1 & u_2 & \dots & u_N \\ \vdots & \vdots & \dots & \vdots \end{bmatrix} \begin{bmatrix} 1 + \lambda_1 + \frac{(\lambda_1 t)^2}{2} \dots & 0 & \dots & 0 \\ 0 & 1 + \lambda_2 + \frac{(\lambda_2 t)^2}{2} \dots & \dots & 0 \\ \vdots & \vdots & \ddots & \vdots \\ 0 & 0 & 0 & 1 + \lambda_1 + \frac{(\lambda_1 t)^2}{2} \dots \end{bmatrix} \begin{bmatrix} \dots & v_1 & \dots \\ \dots & v_2 & \dots \\ \dots & \dots & \dots \\ \dots & v_N & \dots \end{bmatrix} \\ T(t) &= \begin{bmatrix} \vdots & \vdots & \dots & \vdots \\ u_1 & u_2 & \dots & u_N \\ \vdots & \vdots & \dots & \vdots \end{bmatrix} \begin{bmatrix} e^{\lambda_1 t} & 0 & \dots & 0 \\ 0 & e^{\lambda_2 t} & \dots & 0 \\ \vdots & \vdots & \ddots & \vdots \\ 0 & 0 & 0 & e^{\lambda_N t} \end{bmatrix} \begin{bmatrix} \dots & v_1 & \dots \\ \dots & v_2 & \dots \\ \dots & \dots & \dots \\ \dots & v_N & \dots \end{bmatrix} \end{aligned}$$

So  $R$  and  $T$  are closely related.  $Ru_i = \lambda_i u_i$  and  $Tu_i = \mu_i u_i$  where  $\mu_i = e^{\lambda_i t}$ .

Notice, Perron-Frobenius theorem for primitive matrices states that

- $\exists \mu_{PF} \in \mathbb{R}$
- $\mu_{PF} > |\mu_i|$
- $Tu = \mu_{PF} u$  where each elements of  $u$  is positive.
- $\mu_{PF}$  is simple root of  $|T - \lambda I|$ .

Moreover since  $[1 \ 1 \ \dots \ 1]T = [1 \ 1 \ \dots \ 1]$ ,  $\exists \pi$  such that  $T\pi = \pi$  giving us  $\mu_{PF} = 1$ . To finalize:

$$\vec{p}(t) = e^{Rt} \vec{p}(0) = T \vec{p}(0)$$

Since  $T$  is diagonalizable, it has  $N$  independent eigenvectors forming a complete set. Therefore,  $\vec{p}(0)$  can be expressed as a linear combination of  $u$ 's, namely  $\vec{p}(0) = \sum_i^N c_i u_i$ .

$$\begin{aligned} \vec{p}(t) &= T \vec{p}(0) = T \sum_i^N c_i u_i = \sum_i^N c_i \mu_i u_i = \sum_i^N c_i e^{\lambda_i t} u_i \\ &= \pi + \sum_{\mu_i \neq \mu_{PF}}^N c_i e^{\lambda_i t} u_i \end{aligned}$$

$$\lim_{t \rightarrow \infty} \vec{p}(t) = \lim_{t \rightarrow \infty} \left( \pi + \sum_{\mu_i \neq \mu_{PF}}^N c_i e^{\lambda_i t} u_i \right) = \pi$$

Since  $\mu_{PF} = 1 > |\mu_i|$

$$\lim_{t \rightarrow \infty} \sum_{\substack{N \\ \mu_i \neq \mu_{PF}}} c_i e^{\lambda_i t} u_i \rightarrow 0$$

Regardless of the initial conditions,  $\vec{p}(t)$  converges to  $\pi$ .

### Derivation of the 3-state steady-state model for MscS transitions

$$\vec{p}(t) = \begin{pmatrix} C \\ O \\ I \end{pmatrix} \text{ and } R = \begin{bmatrix} -k_{CO} - k_{CI} & k_{OC} & k_{IC} \\ k_{CO} & -k_{OC} & 0 \\ k_{CI} & 0 & -k_{IC} \end{bmatrix}$$

$$\vec{p}(t) = \sum_i^3 c_i e^{\lambda_i t} u_i = c_1 e^{\lambda_1 t} u_1 + c_2 e^{\lambda_2 t} u_2 + c_3 e^{\lambda_3 t} u_3$$

Where  $\lambda_i$ 's are the eigenvalues and  $u_i$ 's are the corresponding eigenvectors of R.

$$\lambda_1 = 0$$

$$\lambda_2 = -\frac{k_{IC}}{2} - \frac{k_{CI}}{2} - \frac{k_{CO}}{2} - \frac{k_{OC}}{2} - \left( \frac{\sqrt{k_{IC}^2 + 2k_{IC}k_{CI} - 2k_{IC}k_{CO} - 2k_{IC}k_{OC} + k_{CI}^2 + 2k_{CI}k_{CO} - 2k_{CI}k_{OC} + k_{CO}^2 + 2k_{CO}k_{OC} + k_{OC}^2}}{2} \right)$$

$$\lambda_3 = -\frac{k_{IC}}{2} - \frac{k_{CI}}{2} - \frac{k_{CO}}{2} - \frac{k_{OC}}{2} + \left( \frac{\sqrt{k_{IC}^2 + 2k_{IC}k_{CI} - 2k_{IC}k_{CO} - 2k_{IC}k_{OC} + k_{CI}^2 + 2k_{CI}k_{CO} - 2k_{CI}k_{OC} + k_{CO}^2 + 2k_{CO}k_{OC} + k_{OC}^2}}{2} \right)$$

As  $t \rightarrow \infty$ , the only surviving term is  $c_1 e^{\lambda_1 t} u_1 = c_1 e^0 u_1 = c_1 u_1 = \pi = \vec{p}(\infty)$ . The right eigenvector is given by:

$$u_1 = \begin{pmatrix} \frac{k_{IC}}{k_{CI}} \\ \frac{k_{IC}k_{CO}}{k_{CI}k_{OC}} \\ 1 \end{pmatrix}$$

and  $c_1$  can be found via normalization giving  $\pi_I$ :

$$\pi_I = \frac{1}{\frac{k_{IC}}{k_{CI}} + \frac{k_{IC} k_{CO}}{k_{CI} k_{OC}} + 1}$$

Another way of getting the steady state solution of the eqn is to note the following:  $\frac{d\vec{\pi}}{dt} = 0$

$$\frac{d\vec{\pi}}{dt} = R\vec{\pi} = \begin{bmatrix} -k_{CO} - k_{CI} & k_{OC} & k_{IC} \\ k_{CO} & -k_{OC} & 0 \\ k_{CI} & 0 & -k_{IC} \end{bmatrix} \begin{pmatrix} \pi_C \\ \pi_O \\ \pi_I \end{pmatrix} = 0$$

Which gives the set of equations:

$$\begin{aligned} -(k_{CO} + k_{CI}) \pi_C + k_{OC} \pi_O + k_{IC} \pi_I &= 0 \\ k_{CO} \pi_C - k_{OC} \pi_O &= 0 \\ k_{CI} \pi_C - k_{IC} \pi_I &= 0 \end{aligned}$$

solving the equations, we got  $\pi_C = \frac{k_{IC}}{k_{CI}} \pi_I$ ,  $\pi_O = \frac{k_{IC} k_{CO}}{k_{CI} k_{OC}} \pi_I$ . Using the normalization:

$$\pi_C + \pi_O + \pi_I = 1 \Rightarrow \pi_I \left( \frac{k_{IC}}{k_{CI}} + \frac{k_{IC} k_{CO}}{k_{CI} k_{OC}} + 1 \right) = 1$$

$$\pi_{In} = \frac{1}{\frac{k_{IC}}{k_{CI}} + \frac{k_{IC} k_{CO}}{k_{CI} k_{OC}} + 1}$$

$$\pi_I = \frac{1}{\frac{k_{IC}^0}{k_{CI}^0} e^{-\beta\gamma A_{Inactivated}} + \frac{k_{IC}^0}{k_{CI}^0} e^{-\beta\gamma A_{Inactivated}} \frac{k_{CO}^0}{k_{OC}^0} e^{\beta\gamma A_{Open}} + 1}$$

It is also possible to obtain at what tension the expression for  $\pi_{In}$  is maximized by solving the equation below:

$$\frac{d\pi_{In}}{d\gamma} = 0$$

$$\frac{-d \left( \frac{k_{IC}^0}{k_{CI}^0} e^{-\beta\gamma A_{Inactivated}} + \frac{k_{IC}^0}{k_{CI}^0} e^{-\beta\gamma A_{Inactivated}} \frac{k_{CO}^0}{k_{OC}^0} e^{\beta\gamma A_{Open}} + 1 \right)}{\left( \frac{k_{IC}^0}{k_{CI}^0} e^{-\beta\gamma A_{Inactivated}} + \frac{k_{IC}^0}{k_{CI}^0} e^{-\beta\gamma A_{Inactivated}} \frac{k_{CO}^0}{k_{OC}^0} e^{\beta\gamma A_{Open}} + 1 \right)^2} = 0$$

$$-\frac{k_{IC}^0}{k_{CI}^0} \beta A_{Inactivated} e^{-\beta\gamma A_{Inactivated}} + \frac{k_{IC}^0}{k_{CI}^0} \frac{k_{CO}^0}{k_{OC}^0} \beta (A_{Open} - A_{Inactivated}) e^{\beta\gamma (A_{Open} - A_{Inactivated})} = 0$$

or

$$\frac{k_{IC}^0}{k_{CI}^0} \frac{k_{CO}^0}{k_{OC}^0} \beta (A_{Open} - A_{Inactivated}) e^{\beta\gamma (A_{Open} - A_{Inactivated})} = \frac{k_{IC}^0}{k_{CI}^0} \beta A_{In} e^{-\beta\gamma A_{Inactivated}}$$

$$e^{\beta\gamma A_{Open}} = \frac{k_{OC}^0}{k_{CO}^0} \frac{A_{Inactivated}}{(A_{Open} - A_{Inactivated})}$$

$$\beta\gamma A_{Open} = \ln \left( \frac{k_{OC}^0}{k_{CO}^0} \frac{A_{Inactivated}}{(A_{Open} - A_{Inactivated})} \right)$$

$$\gamma = \gamma^* = \beta^{-1} A_{Open}^{-1} \ln \left( \frac{k_{OC}^0}{k_{CO}^0} \frac{A_{Inactivated}}{(A_{Open} - A_{Inactivated})} \right)$$

Noticing,  $\frac{k_{OC}^0}{k_{CO}^0} = e^{\beta(E_{CB} - E_{OB})} = e^{\beta\Delta G} = e^{\beta\gamma_{0.5} A_{Open}}$

$$\gamma^* = \beta^{-1} A_{Open}^{-1} \left( \ln e^{\beta\gamma_{0.5} A_{Open}} + \ln \frac{A_{Inactivated}}{A_{Open} - A_{Inactivated}} \right)$$

$$\boxed{\gamma^* = \gamma_{0.5} + \beta^{-1} A_{Open}^{-1} \ln \frac{A_{Inactivated}}{A_{Open} - A_{Inactivated}}}$$

Which can be written as:

$$\boxed{A_{Inactivated} = A_{Open} \left( \frac{e^{\beta A_{Open} (\gamma^* - \gamma_{0.5})}}{1 + e^{\beta A_{Open} (\gamma^* - \gamma_{0.5})}} \right)}$$

## The relationships between expansion areas and gating models of MscS

The obtained protein expansion parameters may provide some insight into the structural aspect of MscS gating and suggest the character of helical arrangement in each of the states and motions during the transitions. Existing structural models of MscS gating have been overviewed in [48]. The very first MscS structure (2OAU), solved in an apparently non-conductive conformation, was considered to represent the resting state [114]. The crystal structure of the A106V mutant (2VV5), solved with a conductive (partially open) pore, was chosen as an approximation for the open conformation [47]. Fig. S4 represents the surfaces and lateral area profiles of the two crystallographic states which indicate that during the predicted C->O transition the transmembrane barrel of MscS expands asymmetrically relative to the bilayer midplane, with the majority of area change taking place near the periplasmic rim and a limited (4.6 nm<sup>2</sup>) expansion at the level of the gate. Notably, the gate is located at the level of the cytoplasmic polar head groups of the lipid bilayer that transmit most of the lateral tension from the bilayer to the channel surface, and tension in the inner leaflet was predicted to drive the opening transition most effectively [45,46]. Both putative closed and open states in this gating concept exhibit splayed peripheral helices uncoupled from the gate, and there was no provision for the inactivated state [47,48]. The alternative model proposed in [49] and supported by functional data interprets the initial non-conductive structure with the uncoupled TM1-TM2 helices as the inactivated state. The physical connection between the peripheral TM1-TM2 helices receiving force from the membrane and the gate-forming TM3s was restored through the cycles of modeling that achieved a tight, almost parallel packing of TM1-TM2 pairs along TM3s [45,50]. The gating cycle was presented as tension-driven alternative transitions into either an open state characterized by straightened TM3s or an inactivated state with the pore closed by kinked TM3s and TM1-TM2 pairs uncoupled from the gate [49]. Both transitions imply outward motion of the protein-lipid boundary, with the opening producing a larger protein expansion. Fig. S4B shows the contours of the three states, which illustrate a more uniform expansion of the barrel as the channel transitions to the open state and a preferential expansion in the cytoplasmic leaflet of the membrane during inactivation (12.1 nm<sup>2</sup> at the tension-bearing level of the gate). The experimentally estimated area changes (Table 1) appear to be more consistent with the structural models rather than expansion area estimate from the non-conducting and conducting crystal structures.

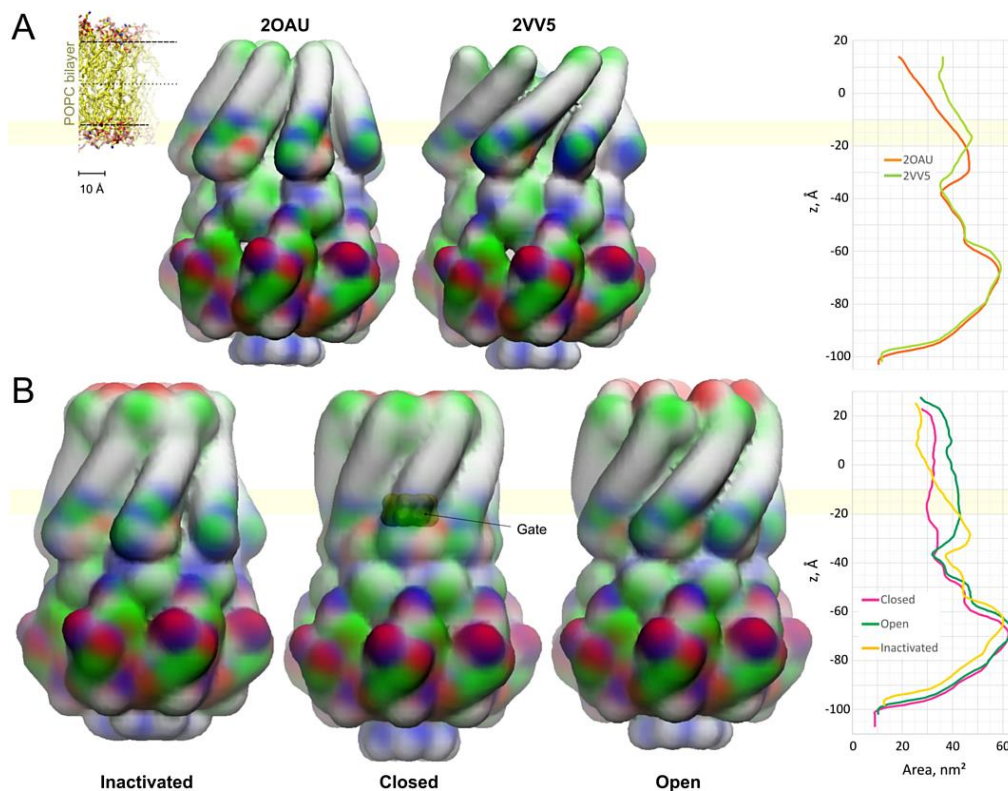
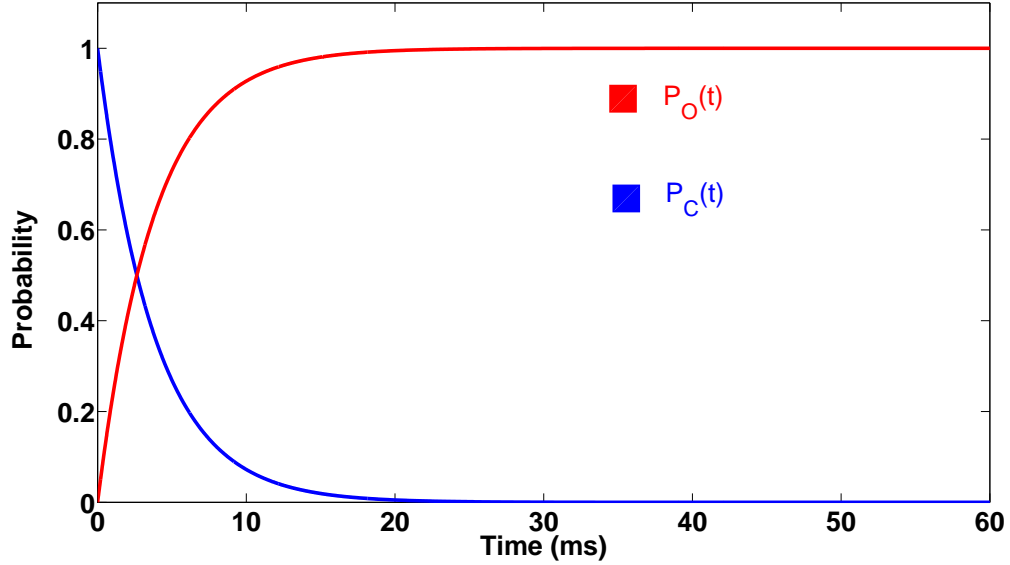
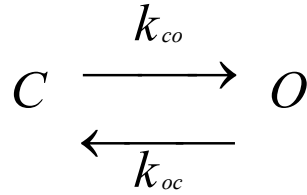


**Figure. S4.** The representative crystal structures and structural models representing the MscS functional cycle. (A) The crystal structures of the non-conductive (2OAU) and conductive states (2VV5), and the plot of their in-plane area illustrating expansion predominantly at the outer rim. (B) The three models created based on the 2OAU structure as a template, simulated in an explicit lipid bilayer and refined through symmetry-driven simulate annealing [50,148] representing compact (closed), fully open and inactivated (uncoupled) states. The inactivated state is closest to the initial 2OAU structure. For clarity, all the structures are shown in a smoothed representation based on the coordinates of the backbone. The surfaces are colored by the residue type: nonpolar (white), polar (green), acidic (red) and basic (blue). The pale-yellow horizontal area near  $-20\text{Å}$  indicates the level of the channel gate in the crystal structures and homology models. Located right at the level of the polar lipid headgroups of the cytoplasmic monolayer, it agrees with *E. coli* MscS opening and inactivation being most sensitive to the tension at that level in the inner leaflet. The area profiles along the channel axis illustrate the strongest expansion at the level of the channel gate,  $12.1\text{ nm}^2$  for the C $\rightarrow$ O transition and a smaller expansion of  $9.3\text{ nm}^2$  associated with inactivation, whereas crystal structures predict expansion of only  $4.6\text{ nm}^2$  at this tension-bearing level. The pale-yellow horizontal area near  $-20\text{Å}$  indicates the level of the channel gate in the crystal structures and homology models. Located right at the level of the polar lipid headgroups of the cytoplasmic monolayer, it agrees with *E. coli* MscS opening and inactivation being most sensitive to the tension at that level.

Recovery of equilibrium free energy from non-equilibrium thermodynamics with mechanosensitive ion channels in E.coli



**SI Figure S1.** Two-state model of MscS gating. Transition rates display exponential dependence on the tension. The system's relaxation to the equilibrium distribution ( $\pi$ ) at  $3 \text{ k}_B \text{T}/\text{nm}^2$  is shown in the figure where  $\pi_C = k_{oc}/(k_{oc} + k_{co})$  and  $\pi_O = k_{co}/(k_{oc} + k_{co})$ . The closed  $\leftrightarrow$  open equilibration happens in a few milliseconds. Specifically, in less than 10 ms  $|P_O(t) - \pi_O| \leq 1/4$  or  $|P_C(t) - \pi_C| \leq 1/4$ . The rate constants at  $3 \text{ k}_B \text{T}/\text{nm}^2$  were evaluated based on the values given in the Table 1 of (Cetiner and Sukharev 2017).



$k_{xy}$  represents the transition rate, probability per unit time, to make a transition from state X to state Y and is described by the Arrhenius-type relation:  $k_{xy} = k_{xy}^0 \exp(\beta\gamma\Delta A_{xB})$  where  $k_{xy}^0$  is the intrinsic rate (frequency) of the system's attempts to overcome the barrier between states X and Y in the absence of the tension.  $\Delta A_{xB}$  is the expansion area from state X to the barrier,  $\gamma$  is the applied tension and  $\beta=1/kT$ . Thus in the presence of tension, states with larger area become more favorable.

The solution for the two-state model at constant tension is given by the following expression:

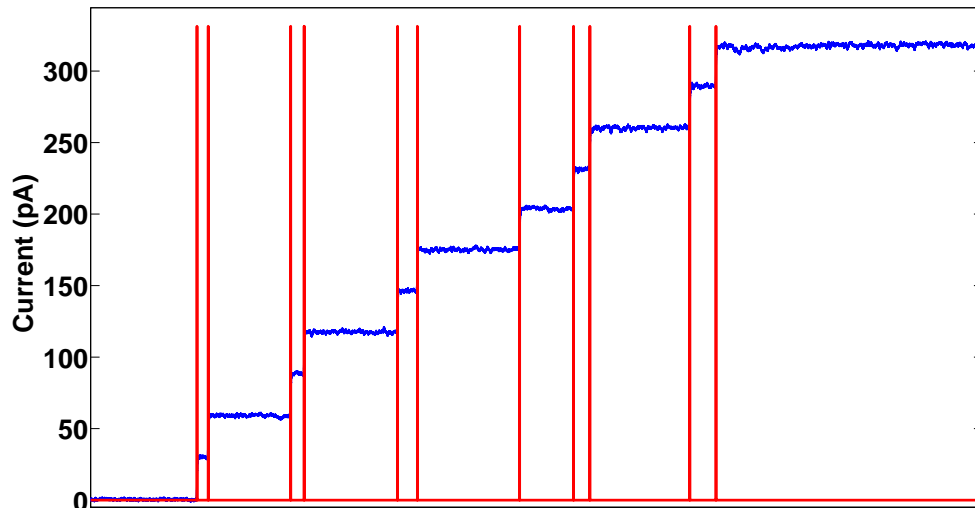
$$P_C(t) = \frac{k_{oc}}{k_{oc} + k_{co}} + \frac{k_{co}}{k_{oc} + k_{co}} e^{-(k_{co} + k_{oc})t}$$

$$P_O(t) = \frac{k_{co}}{k_{oc} + k_{co}} - \frac{k_{co}}{k_{oc} + k_{co}} e^{-(k_{co} + k_{oc})t}$$

As exponential terms die off, probabilities relaxes to a unique equilibrium distribution ( $\pi$ ) where  $\pi_C = k_{oc}/(k_{oc} + k_{co})$  and  $\pi_O = k_{co}/(k_{oc} + k_{co})$ .

At  $3 k_B T/nm^2$ , for  $k_{oc}^0 = 9897 s^{-1}$ ,  $k_{co}^0 = 4e - 6 s^{-1}$ ,  $\Delta A_{cB} = 7 nm^2$  and  $\Delta A_{oB} = 5 nm^2$ , the solutions are depicted in the SI Figure 1.

### Detection of single channel events



**SI Figure S2.** An Edge Detector program

(<http://cismm.web.unc.edu/resources/tutorials/edge-detector-1d-tutorial/>) was employed to detect the single channel events. A membrane with 11 mechanosensitive channels where each single channel event corresponds a step-wise increase in the current. Since MscS has a conductance of 1 nS, at 30 mV, the height of each step is  $\sim 30$  pA.



## Bennett's Acceptance Ratio Method

Bennett's method is obtained by first multiplying both sides of eqn [2] by a real, but otherwise arbitrary function of work,  $f_\mu(W)$  parameterized by  $\mu$  and integration from  $-\infty$  to  $+\infty$ :

$$\int_{-\infty}^{+\infty} f_\mu(W) P_{C \rightarrow O}(W) e^{-\beta W} dW = \int_{-\infty}^{+\infty} f_\mu(W) P_{O \rightarrow C}(-W) e^{-\beta \Delta F} dW$$

yields:

$$\langle f_\mu(W) e^{-\beta W} \rangle_{C \rightarrow O} = e^{-\beta \Delta F} \langle f_\mu(W) \rangle_{O \rightarrow C}$$

Taking the logarithm of both sides gives a simple expression for  $\Delta F$ :

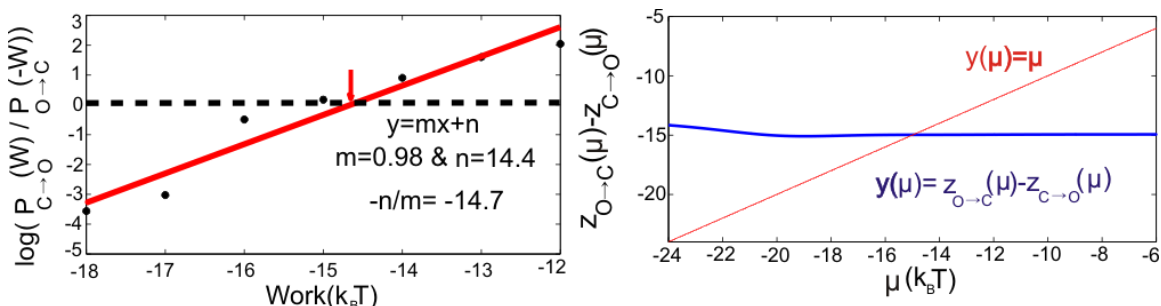
$$\beta \Delta F = z(\mu)_{O \rightarrow C} - z(\mu)_{C \rightarrow O} \quad [*]$$

Where  $z(\mu)_{O \rightarrow C} \equiv \ln \langle f_\mu(W) \rangle_{O \rightarrow C}$  and  $z(\mu)_{C \rightarrow O} \equiv \langle f_\mu(W) e^{-\beta W} \rangle_{C \rightarrow O}$

Bennett showed that among all possible choices for  $f_\mu(W)$ , the one that minimizes the statistical variance of [\*] is:

$$f_\mu(W) = \frac{1}{1 + \frac{N_O}{N_C} e^{\beta(W-\mu)}}$$

Where  $N_O$  and  $N_C$  are the number of realizations obtained for the opening ( $C \rightarrow O$ ) and closing events ( $O \rightarrow C$ ). Notice that [\*] indicates that the difference,  $z(\mu)_{O \rightarrow C} - z(\mu)_{C \rightarrow O}$  is constant regardless of the values that  $\mu$  takes. It is, then, possible to obtain the best estimate for  $\Delta F$  from the intersection of the curves  $y(\mu) = \mu$  with  $y(\mu) = z(\mu)_{O \rightarrow C} - z(\mu)_{C \rightarrow O}$  as shown in SI Fig 4B which reports  $\Delta F$  to be  $-15.0 \pm 0.5 k_B T$  as in good agreement with the overlapping distribution method.



**SI Figure S3.** (A) Semi-logarithmic plot of the ratio of the work distributions in the Fig 4 as a function of work provides the Crooks' estimate for the free energy. The slope is 0.98 and the line intersects with work axis at  $-14.7 k_B T$ . (B) Bennett's acceptance ratio method recovers the free energy from the intersection of the  $y(\mu) = \mu$  with  $y(\mu) = z(\mu)_{O \rightarrow C} - z(\mu)_{C \rightarrow O}$ .

## Overlapping Distributions Method

To drive the Overlapping Distributions Method [190], we first take the log of both side of the Crooks Fluctuation Theorem:

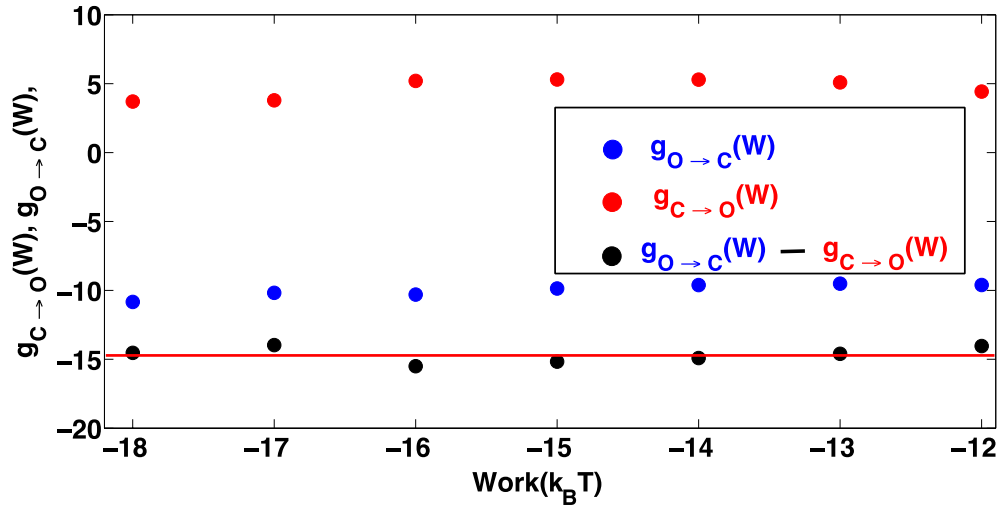
$$\log\left(\frac{P_{C\rightarrow O}(W)}{P_{O\rightarrow C}(-W)}\right) = \log(e^{\beta(W-\Delta F)}) \rightarrow \log(P_{C\rightarrow O}(W)) - \log(P_{O\rightarrow C}(-W)) = \beta(W - \Delta F)$$

Let us define  $g_{C\rightarrow O}(W)$  and  $g_{O\rightarrow C}(W)$  as:

$$g_{C\rightarrow O}(W) \equiv \log(P_{C\rightarrow O}(W)) - \frac{\beta W}{2} \text{ and } g_{O\rightarrow C}(W) \equiv \log(P_{O\rightarrow C}(-W)) + \frac{\beta W}{2}$$

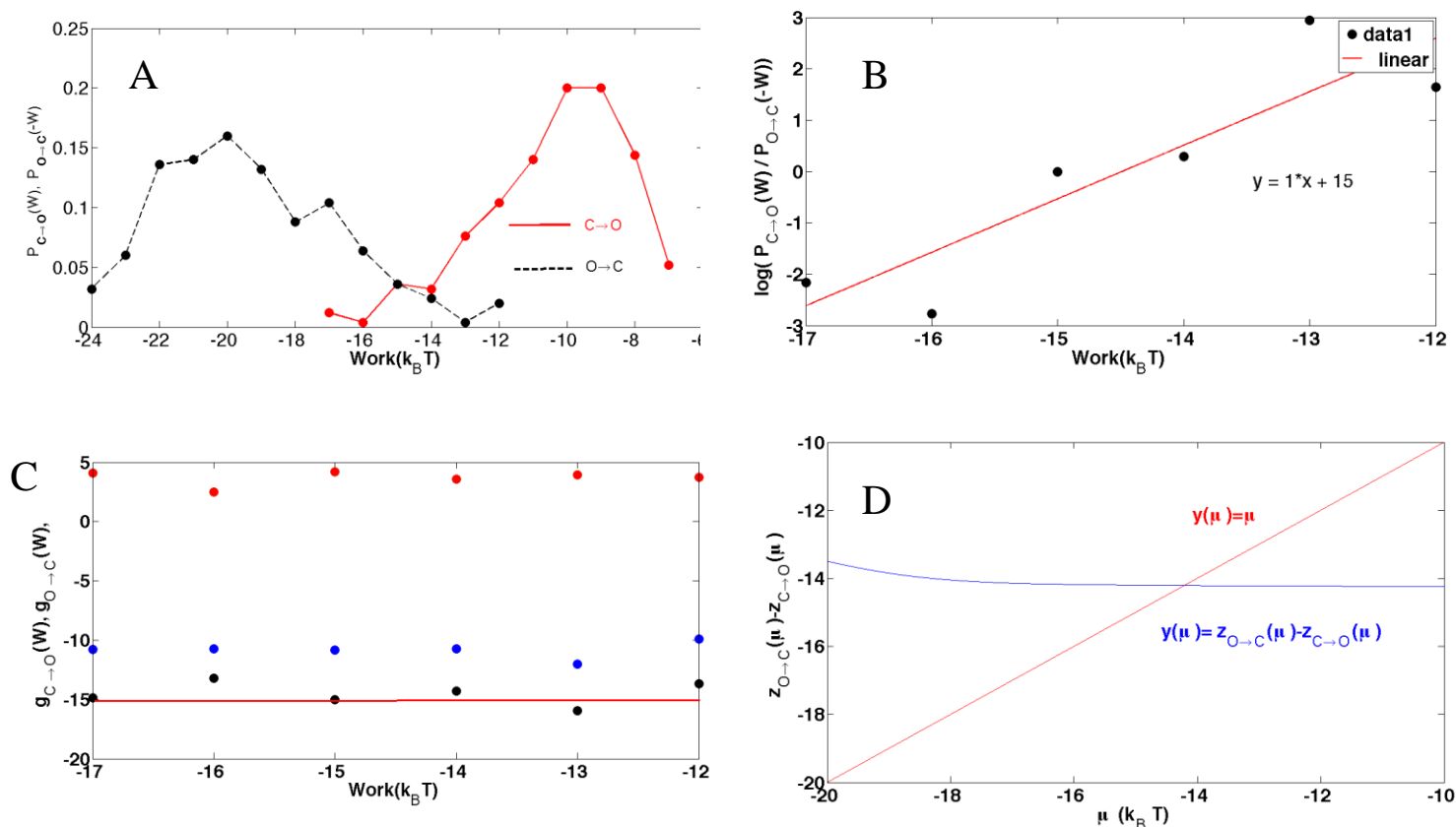
Then the free energy difference can be obtained by using the following relation:

$$g_{O\rightarrow C}(W) - g_{C\rightarrow O}(W) = \beta\Delta F$$



**SI Figure S4.** Overlapping Distributions Method. The plot of  $g_{C\rightarrow O}(W)$ ,  $g_{O\rightarrow C}(W)$  and the difference,  $g_{O\rightarrow C}(W) - g_{C\rightarrow O}(W)$ , as a function of  $W$ . The difference can be used to extract  $\Delta F$ . In this plot,  $\Delta F = -14.7$

## Markov Chain Simulation Two-State Model

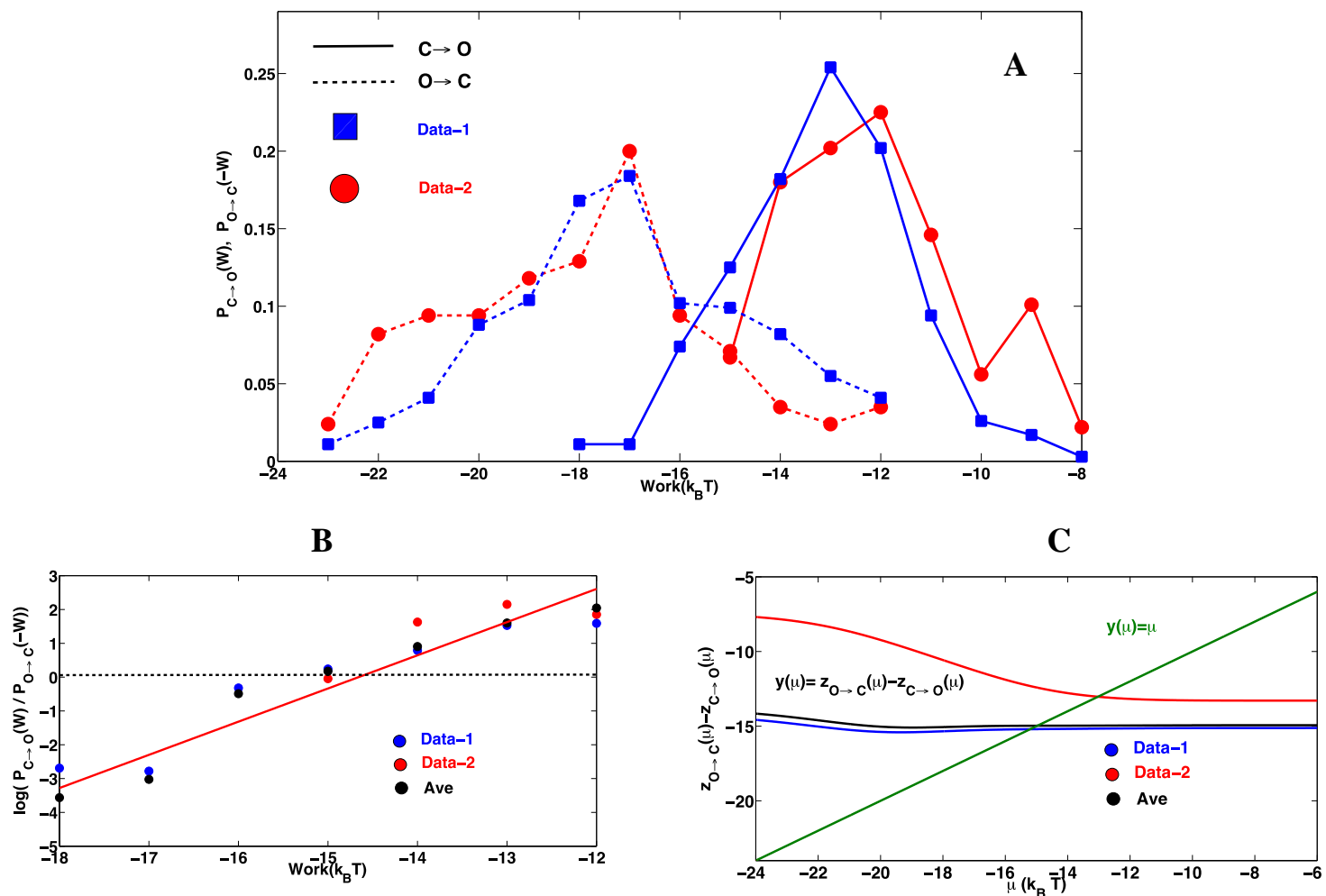


**SI Figure S5** (A) Histograms of the work distributions (B) Semi-logarithmic plot of the ratio of the work distributions (C) Overlapping Distributions Method (D) Bennett's acceptance ratio method. Simulation was performed using the experimental protocol in the main text as stimulus with the following parameters:  $k_{oc}^0 = 9897 \text{ s}^{-1}$ ,  $k_{co}^0 = 4 \text{ e} - 6 \text{ s}^{-1}$ ,  $\Delta A_{cB} = 7 \text{ nm}^2$  and  $\Delta A_{oB} = 5 \text{ nm}^2$ .

N	$\Delta F$ Jarzynski	$\Delta F$ Crooks	$\Delta F$ Bennett	$\Delta F$ Overlapping
250	-14.5	-15.0	-14.3	-14.5

$$\Delta F_0 = \Delta F + \gamma \Delta A|_0^{\tau} \Rightarrow \Delta F_0 = -14.3 + 3 \times 12 = 21.7 k_B T$$

## Reproducibility of work distributions



**SI Figure S6.** (A) The work distributions obtained from two different membranes for the typical experimental protocol where the membrane tension is increased to its final value of  $3 \text{ k}_B\text{T}/\text{nm}^2$  in a second and is decreased back to zero with the same rate after 1s equilibration time. The free energy difference predicted by various means such as the plot of  $\log(P_{C \rightarrow O}(W)/P_{O \rightarrow C}(-W))$  as a function  $W/k_B T$  (B) and the Bennett's acceptance ratio method (C) is listed in the Supplementary Table 1 for two different membranes under the same experimental protocol.

Table 1	$\langle W \rangle_{C \rightarrow O}$	$\sigma_{C \rightarrow O}$	$\langle W \rangle_{O \rightarrow C}$	$\sigma_{O \rightarrow C}$	$\langle W_{Diss} \rangle$	$\Delta F$ Linear Response	$\Delta F$ Jarzynski	$\Delta F$ Crooks	$\Delta F$ Crossing	$\Delta F$ Bennet's	$\Delta F$ Overlapping
Data-1	-13.2 (N=351)	1.74	17.0 (N=364)	2.49	3.8	-14.3	-14.7	-14.9	-15.5	-15.2	-14.8
Data-2	-12.1 (N=89)	1.85	17.9 (N=85)	2.77	5.8	-14.0	-13.5	-15.8	-15.0	-13.0	-14.9

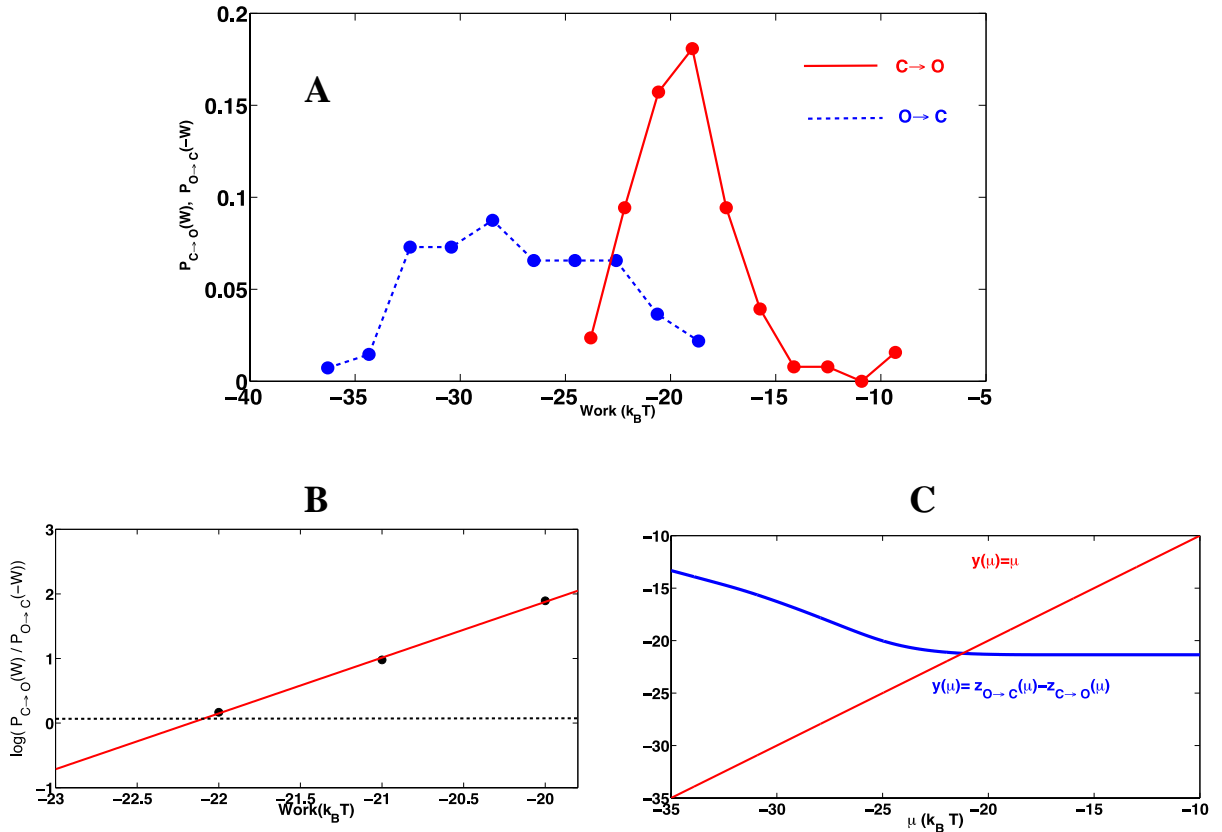
## Recovery of free energy under different experimental protocols

The  $\Delta F$  predicted by the fluctuation theorems refers to the free energy difference between two equilibrium states associated with the initial and final value of the work parameter (system + driving force). For the typical experimental protocol carried in this paper,  $\Delta F \equiv F(\gamma_\tau = 3 \text{ k}_B\text{T/nm}^2) - F(\gamma_0 = 0 \text{ k}_B\text{T/nm}^2)$ , whereas  $\Delta F_0$  denotes the free energy difference between the closed and open state of the system in the absence of the tension which is experimentally the more relevant parameter to obtain.  $\Delta F_0$  can easily be recovered by adding the corresponding boundary term to  $\Delta F$ ,  $\Delta F_0 = \Delta F + \gamma\Delta A|_0^\tau$ . As a sanity check, we tried a different protocol where the tension is increased to  $\gamma_\tau = 3.6 \text{ k}_B\text{T/nm}^2$  in 250 millisecond and decreased back to 0 with the same rate after equilibration. The free energy difference in this case,  $\Delta F'$  is different than our typical:

$\Delta F' = F(\gamma_\tau = 3.6 \text{ k}_B\text{T/nm}^2) - F(\gamma_0 = 0 \text{ k}_B\text{T/nm}^2)$  yet  $\Delta F_0$  can still be recovered within experimental uncertainty even though the statistics are not as rich. The summary of the results for this protocol is provided in the Table 2.

$$\Delta F_0 = \Delta F' + \gamma\Delta A|_0^\tau$$

$$\Delta F_0 = -21.2 + 3.6 \times 12 = 22 \text{ kT}$$



**SI Figure S7. (A)** Histogram of work distributions obtained from a different experimental protocol where the membrane tension is increased to its final value of  $3.6 \text{ k}_B\text{T}/\text{nm}^2$  in 250 milliseconds and is decreased back to zero with the same rate after 1s equilibration time. Note that this process is more dissipative than the typical experimental protocol. As expected, the fluctuation theorems give a different  $\Delta F' = F(\gamma_\tau = 3.6 \text{ k}_B\text{T}/\text{nm}^2) - F(\gamma_0 = 0 \text{ k}_B\text{T}/\text{nm}^2)$  nevertheless,  $\Delta F_0$ , which is the free energy difference between the closed and open state of the channel in the absence of the membrane tension, can still be recovered by adding the corresponding boundary term.  $\Delta F'$  obtained by using different estimators such the plot of  $\log(P_{C \rightarrow O}(W)/P_{O \rightarrow C}(-W))$  as a function  $W/\text{k}_B\text{T}$  (**B**) and the Bennet's acceptance ratio method (**C**) is listed in Table 2.

Table 2	$\langle W \rangle_{C \rightarrow O}$	$\sigma_{C \rightarrow O}$	$\langle W \rangle_{O \rightarrow C}$	$\sigma_{O \rightarrow C}$	$\langle W_{Diss} \rangle$	$\Delta F$ Linear Response	$\Delta F$ Jarzynski	$\Delta F$ Crooks	$\Delta F$ Crossing	$\Delta F$ Bennet's	$\Delta F$ Overlapping
Data-1	-19.2 (N=79)	2.70	26.9 (N=70)	4.42	7.7	-20.0	-20.7	-22.3	-22.8	-21.2	-22.0

Lastly, as we stated in the main text, it is possible perform a sanity check for the two-state assumption and  $\Delta A$ . If we repeat the measurements for different values of  $\gamma_\tau$ , the change in  $\Delta F$  with respect to  $\gamma_\tau$  should reveal  $\Delta A$ .

Let us estimate average  $\Delta A$  based on two different values of  $\gamma_\tau$  used in this paper:  $\gamma_\tau^1 = 3 \text{ k}_B\text{T}/\text{nm}^2$  and  $\gamma_\tau^2 = 3.6 \text{ k}_B\text{T}/\text{nm}^2$ .

$$|\Delta A| = \left| \frac{\Delta F^2 - \Delta F^1}{\gamma_\tau^2 - \gamma_\tau^1} \right| = \left| \frac{F(\gamma_\tau^2 = 3.6 \frac{\text{k}_B\text{T}}{\text{nm}^2}) - F(\gamma_\tau^1 = 3 \frac{\text{k}_B\text{T}}{\text{nm}^2})}{(3.6 - 3)} \right|$$

Table 3	$\Delta F$ Jarzynski	$\Delta F$ Crooks	$\Delta F$ Bennett	$\Delta F$ Crossing	$\Delta F$ Overlapping
$\gamma_\tau^1 = 3 \text{ k}_B\text{T}/\text{nm}^2$	-14.5	-14.7	-15.0	-15.3	-14.7
$\gamma_\tau^2 = 3.6 \text{ k}_B\text{T}/\text{nm}^2$	-20.7	-22.3	-21.2	-22.8	-22.0
$ \Delta A , \text{nm}^2$	10.3	12.7	10.3	12.5	12.2

The average  $\Delta A$  based on two different experimental protocols is determined as  $11.6 \text{ nm}^2$  which is in good agreement with MD simulations of crystallographic structures of the closed and open states where the membrane displayed area of activation ( $C \rightarrow O$ ) is predicted to be  $12.1 \text{ nm}^2$

## Bibliography

- [1] F. Sachs, *Physiology (Bethesda)* **25**, 50 (2010).
- [2] S. Sukharev and F. Sachs, *J Cell Sci* **125**, 3075 (2012).
- [3] C. Kung, *Nature* **436**, 647 (2005).
- [4] C. Ellison and Y. V. Brun, *Curr Biol* **25**, R113 (2015).
- [5] N. Baeyens and M. A. Schwartz, *Mol Biol Cell* **27**, 7 (2016).
- [6] J. M. Tarbell and M. Y. Pahakis, *J Intern Med* **259**, 339 (2006).
- [7] S. W. Moore, P. Roca-Cusachs, and M. P. Sheetz, *Dev Cell* **19**, 194 (2010).
- [8] T. D. Ross, B. G. Coon, S. Yun, N. Baeyens, K. Tanaka, M. Ouyang, and M. A. Schwartz, *Curr Opin Cell Biol* **25**, 613 (2013).
- [9] A. L. Berrier and K. M. Yamada, *J Cell Physiol* **213**, 565 (2007).
- [10] B. Martinac and A. Kloda, *Prog Biophys Mol Biol* **82**, 11 (2003).
- [11] B. Martinac, *J Cell Sci* **117**, 2449 (2004).
- [12] Y. Ben-Shahar, *Adv Genet* **76**, 1 (2011).
- [13] D. E. Clapham, *Nature* **426**, 517 (2003).
- [14] B. Coste, B. Xiao, J. S. Santos, R. Syeda, J. Grandl, K. S. Spencer, S. E. Kim, M. Schmidt, J. Mathur, A. E. Dubin, M. Montal, and A. Patapoutian, *Nature* **483**, 176 (2012).
- [15] S. E. Kim, B. Coste, A. Chadha, B. Cook, and A. Patapoutian, *Nature* **483**, 209 (2012).
- [16] P. A. Gottlieb and F. Sachs, *Nature* **483**, 163 (2012).
- [17] G. Makshev and E. S. Haswell, *Proc Natl Acad Sci USA* **109**, 19015 (2012).
- [18] K. M. Veley, S. Marshburn, C. E. Clure, and E. S. Haswell, *Curr Biol* **22**, 408 (2012).
- [19] E. S. Hamilton, A. M. Schlegel, and E. S. Haswell, *Annu Rev Plant Biol* **66**, 113 (2015).
- [20] D. Basu and E. S. Haswell, *Curr Opin Plant Biol* **40**, 43 (2017).
- [21] S. S. Ranade, R. Syeda, and A. Patapoutian, *Neuron* **87**, 1162 (2015).
- [22] S. Sukharev and D. P. Corey, *Sci STKE* **2004**, re4 (2004).
- [23] E. S. Haswell, R. Phillips, and D. C. Rees, *Structure* **19**, 1356 (2011).

- [24] L. Margulis, D. Sagan, and L. Thomas, *Microcosmos: Four Billion Years of Microbial Evolution*, Reprint (University of California Press, 1997).
- [25] H. Ochman, J. G. Lawrence, and E. A. Groisman, *Nature* **405**, 299 (2000).
- [26] D. S. Cayley, H. J. Guttman, and M. T. Record, *Biophys J* **78**, 1748 (2000).
- [27] Y. Deng, M. Sun, and J. W. Shaevitz, *Phys Rev Lett* **107**, 158101 (2011).
- [28] J. M. Wood, *Microbiol Mol Biol Rev* **63**, 230 (1999).
- [29] U. Çetiner, I. Rowe, A. Schams, C. Mayhew, D. Rubin, A. Anishkin, and S. Sukharev, *J Gen Physiol* **149**, 595 (2017).
- [30] M. Bialecka-Fornal, H. J. Lee, and R. Phillips, *J Bacteriol* **197**, 231 (2015).
- [31] G. Calamita, W. R. Bishai, G. M. Preston, W. B. Guggino, and P. Agre, *J Biol Chem* **270**, 29063 (1995).
- [32] G. Calamita, *Mol Microbiol* **37**, 254 (2000).
- [33] R. N. Finn and J. Cerdà, *Biol Bull* **229**, 6 (2015).
- [34] S. I. Sukharev, P. Blount, B. Martinac, F. R. Blattner, and C. Kung, *Nature* **368**, 265 (1994).
- [35] N. Levina, S. Töttemeyer, N. R. Stokes, P. Louis, M. A. Jones, and I. R. Booth, *EMBO J* **18**, 1730 (1999).
- [36] R. J. Britten and F. T. McCLURE, *Bacteriol Rev* **26**, 292 (1962).
- [37] E. Neher and B. Sakmann, *Nature* **260**, 799 (1976).
- [38] O. P. Hamill, A. Marty, E. Neher, B. Sakmann, and F. J. Sigworth, *Pflugers Arch* **391**, 85 (1981).
- [39] B. Sakmann and E. Neher, *Annu Rev Physiol* **46**, 455 (1984).
- [40] B. Martinac, M. Buechner, A. H. Delcour, J. Adler, and C. Kung, *Proc Natl Acad Sci USA* **84**, 2297 (1987).
- [41] A. H. Delcour, B. Martinac, J. Adler, and C. Kung, *Biophys J* **56**, 631 (1989).
- [42] S. I. Sukharev, B. Martinac, V. Y. Arshavsky, and C. Kung, *Biophys J* **65**, 177 (1993).
- [43] Y. Li, P. C. Moe, S. Chandrasekaran, I. R. Booth, and P. Blount, *EMBO J* **21**, 5323 (2002).
- [44] R. B. Bass, P. Strop, M. Barclay, and D. C. Rees, *Science* **298**, 1582 (2002).
- [45] V. Belyy, A. Anishkin, K. Kamaraju, N. Liu, and S. Sukharev, *Nat Struct Mol Biol* **17**, 451 (2010).



- [46] V. Belyy, K. Kamaraju, B. Akitake, A. Anishkin, and S. Sukharev, *J Gen Physiol* **135**, 641 (2010).
- [47] W. Wang, S. S. Black, M. D. Edwards, S. Miller, E. L. Morrison, W. Bartlett, C. Dong, J. H. Naismith, and I. R. Booth, *Science* **321**, 1179 (2008).
- [48] J. H. Naismith and I. R. Booth, *Annu Rev Biophys* **41**, 157 (2012).
- [49] B. Akitake, A. Anishkin, N. Liu, and S. Sukharev, *Nat Struct Mol Biol* **14**, 1141 (2007).
- [50] A. Anishkin, B. Akitake, and S. Sukharev, *Biophys J* **94**, 1252 (2008).
- [51] B. Akitake, A. Anishkin, and S. Sukharev, *J Gen Physiol* **125**, 143 (2005).
- [52] A. C. Hurst, P. A. Gottlieb, and B. Martinac, *Eur Biophys J* **38**, 415 (2009).
- [53] M. Boer, A. Anishkin, and S. Sukharev, *Biochemistry* **50**, 4087 (2011).
- [54] T. Ursell, J. Kondev, D. Reeves, P. A. Wiggins, and R. RobPhillips, in *Mechanosensitive Ion Channels*, edited by A. Kamkin and I. Kiseleva (Springer Netherlands, Dordrecht, 2008), pp. 37–70.
- [55] D. P. Corey and A. J. Hudspeth, *J Neurosci* **3**, 962 (1983).
- [56] O. P. Hamill and D. W. McBride, *Trends Neurosci* **17**, 439 (1994).
- [57] V. S. Markin and F. Sachs, *Phys Biol* **1**, 110 (2004).
- [58] E. Perozo, A. Kloda, D. M. Cortes, and B. Martinac, *Nat Struct Biol* **9**, 696 (2002).
- [59] D. Colquhoun and A. G. Hawkes, *Proc R Soc Lond, B, Biol Sci* **199**, 231 (1977).
- [60] D. Colquhoun, C. J. Hatton, and A. G. Hawkes, *J Physiol (Lond)* **547**, 699 (2003).
- [61] F. Qin, A. Auerbach, and F. Sachs, *Biophys J* **70**, 264 (1996).
- [62] J. R. Norris, *Markov Chains*, illustrated, reprint (Cambridge University Press, 1998).
- [63] O. Raz, Y. Subaşı, and C. Jarzynski, *Phys. Rev. X* **6**, 021022 (2016).
- [64] A. B. Kolomeisky and M. E. Fisher, *Annu Rev Phys Chem* **58**, 675 (2007).
- [65] H. Qian, *J Phys Condens Matter* **17**, S3783 (2005).
- [66] C. Bustamante, J. Liphardt, and F. Ritort, *Phys Today* **58**, 43 (2005).
- [67] G. E. Crooks, *J. Stat. Mech.* **2011**, P07008 (2011).
- [68] E. H. Feng and G. E. Crooks, *Phys. Rev. Lett.* **101**, (2008).

- [69] F. Ritort, in *Poincaré Seminar 2003*, edited by J. Dalibard, B. Duplantier, and V. Rivasseau (Birkhäuser Basel, Basel, 2004), pp. 193–226.
- [70] C. Jarzynski, *Proc Natl Acad Sci USA* **98**, 3636 (2001).
- [71] C. Jarzynski, *Annu. Rev. Condens. Matter Phys.* **2**, 329 (2011).
- [72] C. Jarzynska, *Eur. Phys. J. B* **64**, 331 (2008).
- [73] E. Boksenbojm, B. Wynants, and C. Jarzynski, *Physica A: Statistical Mechanics and Its Applications* **389**, 4406 (2010).
- [74] D. Collin, F. Ritort, C. Jarzynski, S. B. Smith, I. Tinoco, and C. Bustamante, *Nature* **437**, 231 (2005).
- [75] G. N. Bochkov and E. Kuzovlev, (n.d.).
- [76] G. N. Bochkov and Y. E. Kuzovlev, *Soviet Journal of Experimental and Theoretical Physics* **49**, (1979).
- [77] D. J. Evans, E. G. Cohen, and G. P. Morriss, *Phys Rev Lett* **71**, 2401 (1993).
- [78] D. J. Evans and D. J. Searles, (n.d.).
- [79] G. Gallavotti and E. G. D. Cohen, *J Stat Phys* **80**, 931 (1995).
- [80] G. Gallavotti and E. G. Cohen, *Phys Rev Lett* **74**, 2694 (1995).
- [81] J. Kurchan, *J Phys A Math Gen* **31**, 3719 (1998).
- [82] J. L. Lebowitz and H. Spohn, *Journal of Statistical Physics* (1999).
- [83] C. Maes, *Journal of Statistical Physics* (1999).
- [84] G. Hummer and A. Szabo, *Proc Natl Acad Sci USA* **98**, 3658 (2001).
- [85] C. Jarzynski, *Phys. Rev. Lett.* **78**, 2690 (1997).
- [86] G. E. Crooks, *Phys Rev E Stat Phys Plasmas Fluids Relat Interdiscip Topics* **60**, 2721 (1999).
- [87] G. E. Crooks, *Phys. Rev. E* **61**, 2361 (2000).
- [88] C. Jarzynski, *J. Stat. Mech.* **2004**, P09005 (2004).
- [89] G. N. Lewis, *Proc Natl Acad Sci USA* **11**, 179 (1925).
- [90] G. Crooks, *Journal of Statistical Physics* (1998).
- [91] M. D. Edwards, S. Black, T. Rasmussen, A. Rasmussen, N. R. Stokes, T. L. Stephen, S. Miller, and I. R. Booth, *Channels (Austin)* **6**, 272 (2012).

- [92] U. Schumann, M. D. Edwards, T. Rasmussen, W. Bartlett, P. van West, and I. R. Booth, *Proc Natl Acad Sci U S A* **107**, 12664 (2010).
- [93] P. Blount and P. C. Moe, *Trends Microbiol* **7**, 420 (1999).
- [94] I. R. Booth and P. Blount, *J Bacteriol* **194**, 4802 (2012).
- [95] M. Bialecka-Fornal, H. J. Lee, H. A. DeBerg, C. S. Gandhi, and R. Phillips, *PLoS ONE* **7**, e33077 (2012).
- [96] I. Rowe, M. Elahi, A. Huq, and S. Sukharev, *J Gen Physiol* **142**, 75 (2013).
- [97] A. Kloda, E. Petrov, G. R. Meyer, T. Nguyen, A. C. Hurst, L. Hool, and B. Martinac, *Int J Biochem Cell Biol* **40**, 164 (2008).
- [98] K. D. Mena and C. P. Gerba, *Rev Environ Contam Toxicol* **201**, 71 (2009).
- [99] L. Hall-Stoodley, J. W. Costerton, and P. Stoodley, *Nat Rev Microbiol* **2**, 95 (2004).
- [100] R. Mittal, S. Aggarwal, S. Sharma, S. Chhibber, and K. Harjai, *J Infect Public Health* **2**, 101 (2009).
- [101] W. A. Agger and A. Mardan, *Clin Infect Dis* **20**, 302 (1995).
- [102] M. Hogardt and J. Heesemann, *Int J Med Microbiol* **300**, 557 (2010).
- [103] J. M. Wood, E. Bremer, L. N. Csonka, R. Kraemer, B. Poolman, T. van der Heide, and L. T. Smith, *Comp Biochem Physiol, Part A Mol Integr Physiol* **130**, 437 (2001).
- [104] M. R. D'Souza-Ault, L. T. Smith, and G. M. Smith, *Appl Environ Microbiol* **59**, 473 (1993).
- [105] A. Aspedon, K. Palmer, and M. Whiteley, *J Bacteriol* **188**, 2721 (2006).
- [106] T. Hoshino, *J Bacteriol* **139**, 705 (1979).
- [107] J. Glick and N. Garber, *J Gen Microbiol* **129**, 3085 (1983).
- [108] W. Epstein, *FEMS Microbiol Lett* **39**, 73 (1986).
- [109] L. N. Csonka, *Microbiol Rev* **53**, 121 (1989).
- [110] J. M. Wood, *Sci STKE* **2006**, pe43 (2006).
- [111] C. Kung, B. Martinac, and S. Sukharev, *Annu Rev Microbiol* **64**, 313 (2010).
- [112] S. I. Sukharev, P. Blount, B. Martinac, and C. Kung, *Annu Rev Physiol* **59**, 633 (1997).
- [113] E. Perozo and D. C. Rees, *Curr Opin Struct Biol* **13**, 432 (2003).
- [114] S. Steinbacher, R. Bass, P. Strop, and D. C. Rees, in *Mechanosensitive Ion Channels, Part A* (Elsevier, 2007), pp. 1–24.

- [115] M. Reuter, N. J. Hayward, S. S. Black, S. Miller, D. T. Dryden, and I. R. Booth, *J R Soc Interface* **11**, 20130850 (2014).
- [116] D. B. Rhoads, F. B. Waters, and W. Epstein, *J Gen Physiol* **67**, 325 (1976).
- [117] P. Blount, S. I. Sukharev, M. J. Schroeder, S. K. Nagle, and C. Kung, *Proc Natl Acad Sci USA* **93**, 11652 (1996).
- [118] G. Sezonov, D. Joseleau-Petit, and R. D'Ari, *J Bacteriol* **189**, 8746 (2007).
- [119] A. L. Koch, *Annu Rev Microbiol* **50**, 317 (1996).
- [120] A. L. Koch, *Biochimica et Biophysica Acta* **51**, 429 (1961).
- [121] E. Rojas, J. A. Theriot, and K. C. Huang, *Proc Natl Acad Sci USA* **111**, 7807 (2014).
- [122] W. W. Baldwin, M. J. Sheu, P. W. Bankston, and C. L. Woldringh, *J Bacteriol* **170**, 452 (1988).
- [123] M. P. van Heeswijk and C. H. van Os, *J Membr Biol* **92**, 183 (1986).
- [124] W. W. Baldwin and P. W. Bankston, *Appl Environ Microbiol* **54**, 105 (1988).
- [125] K. Okada, P. C. Moe, and P. Blount, *J Biol Chem* **277**, 27682 (2002).
- [126] C. Maurel, F. Tacnet, J. Güclü, J. Guern, and P. Ripoché, *Proc Natl Acad Sci USA* **94**, 7103 (1997).
- [127] S. Cayley and M. T. Record, *J Mol Recognit* **17**, 488 (2004).
- [128] E. G. Hubert, C. S. Potter, T. J. Hensley, M. Cohen, G. M. Kalmanson, and L. B. Guze, *Infect Immun* **4**, 60 (1971).
- [129] S. Sukharev, *Biophys J* **83**, 290 (2002).
- [130] S. I. Sukharev, W. J. Sigurdson, C. Kung, and F. Sachs, *J Gen Physiol* **113**, 525 (1999).
- [131] P. Moe and P. Blount, *Biochemistry* **44**, 12239 (2005).
- [132] K. Kamaraju, V. Belyy, I. Rowe, A. Anishkin, and S. Sukharev, *J Gen Physiol* **138**, 49 (2011).
- [133] H. Benamara, C. Rihouey, T. Jouenne, and S. Alexandre, *Biochim Biophys Acta* **1808**, 98 (2011).
- [134] D. B. Roszak and R. R. Colwell, *Microbiol Rev* **51**, 365 (1987).
- [135] L. Volkers, Y. Mechioukhi, and B. Coste, *Pflugers Arch* **467**, 95 (2015).
- [136] C. Heurteaux, G. Lucas, N. Guy, M. El Yacoubi, S. Thümmel, X. D. Peng, F. Noble, N. Blondeau, C. Widmann, M. Borsotto, G. Gobbi, J. M. Vaugeois, G. Debonnel, and M. Lazdunski, *Nat Neurosci* **9**, 1134 (2006).

- [137] A. Alloui, K. Zimmermann, J. Mamet, F. Duprat, J. Noël, J. Chemin, N. Guy, N. Blondeau, N. Voilley, C. Rubat-Coudert, M. Borsotto, G. Romey, C. Heurteaux, P. Reeh, A. Eschalier, and M. Lazdunski, *EMBO J* **25**, 2368 (2006).
- [138] K. Retailleau and F. Duprat, *J Physiol (Lond)* **592**, 2453 (2014).
- [139] C. M. Walsh, D. M. Bautista, and E. A. Lumpkin, *Curr Opin Neurobiol* **34**, 133 (2015).
- [140] D. L. Prole and C. W. Taylor, *PLoS ONE* **8**, e66068 (2013).
- [141] E. S. Haswell, R. Peyronnet, H. Barbier-Brygoo, E. M. Meyerowitz, and J. M. Frachisse, *Curr Biol* **18**, 730 (2008).
- [142] Y. Nakagawa, T. Katagiri, K. Shinozaki, Z. Qi, H. Tatsumi, T. Furuichi, A. Kishigami, M. Sokabe, I. Kojima, S. Sato, T. Kato, S. Tabata, K. Iida, A. Terashima, M. Nakano, M. Ikeda, T. Yamanaka, and H. Iida, *Proc Natl Acad Sci U S A* **104**, 3639 (2007).
- [143] P. Blount, S. I. Sukharev, P. C. Moe, M. J. Schroeder, H. R. Guy, and C. Kung, *EMBO J* **15**, 4798 (1996).
- [144] C. Berrier, M. Besnard, B. Ajouz, A. Coulombe, and A. Ghazi, *Journal of Membrane Biology* **151**, 175 (1996).
- [145] I. R. Booth, *Curr Opin Microbiol* **18**, 16 (2014).
- [146] K. Kamaraju and S. Sukharev, *Biochemistry* **47**, 10540 (2008).
- [147] K. Kamaraju, P. A. Gottlieb, F. Sachs, and S. Sukharev, *Biophys J* **99**, 2870 (2010).
- [148] A. Anishkin, K. Kamaraju, and S. Sukharev, *J Gen Physiol* **132**, 67 (2008).
- [149] J. Huang, S. Rauscher, G. Nawrocki, T. Ran, M. Feig, B. L. de Groot, H. Grubmüller, and A. D. MacKerell, *Nat Methods* **14**, 71 (2017).
- [150] W. Humphrey, A. Dalke, and K. Schulten, *J Mol Graph* **14**, 33 (1996).
- [151] G. I. Bell, *Science* **200**, 618 (1978).
- [152] J. I. Steinfeld, J. S. Francisco, and W. L. Hase, *Chemical Kinetics and Dynamics* (Prentice Hall Englewood Cliffs, New Jersey, 1989).
- [153] J. Schnakenberg, *Rev. Mod. Phys.* **48**, 571 (1976).
- [154] J. R. Norris, *Markov Chains* (Cambridge university press, 1998).
- [155] Y. Nakayama, K. Yoshimura, and H. Iida, *Biophys J* **105**, 1366 (2013).
- [156] M. Schlierf, H. Li, and J. M. Fernandez, *Proc Natl Acad Sci U S A* **101**, 7299 (2004).
- [157] C. Nicolai and F. Sachs, *Biophys. Rev. Lett.* **08**, 191 (2013).

- [158] J. B. S. Haldane, *The Rationalist Annual* **148**, 3 (1929).
- [159] A. I. I. Oparin and S. Morgulis, *The Origin of Life*, 2nd ed. (Dover Publications, Mineola, New York, 1953).
- [160] T. J. Silhavy, D. Kahne, and S. Walker, *Cold Spring Harb Perspect Biol* **2**, a000414 (2010).
- [161] B. Martinac, Y. Saimi, and C. Kung, *Physiol Rev* **88**, 1449 (2008).
- [162] J. M. Wood, *J Gen Physiol* **145**, 381 (2015).
- [163] C. S. Chiang, A. Anishkin, and S. Sukharev, *Biophys J* **86**, 2846 (2004).
- [164] H. R. Malcolm and J. A. Maurer, *Chembiochem* **13**, 2037 (2012).
- [165] C. D. Cox, Y. Nakayama, T. Nomura, and B. Martinac, *Pflugers Arch* **467**, 3 (2015).
- [166] R. Buda, Y. Liu, J. Yang, S. Hegde, K. Stevenson, F. Bai, and T. Pilizota, *Proc Natl Acad Sci U S A* **113**, E5838 (2016).
- [167] E. Petrov, D. Palanivelu, M. Constantine, P. R. Rohde, C. D. Cox, T. Nomura, D. L. Minor, and B. Martinac, *Biophys J* **104**, 1426 (2013).
- [168] A. Kloda and B. Martinac, *Eur Biophys J* **31**, 14 (2002).
- [169] T. Hatano and S. Sasa, *Phys Rev Lett* **86**, 3463 (2001).
- [170] S. X. Sun, *J Chem Phys* **118**, 5769 (2003).
- [171] D. J. Evans, *Mol Phys* **101**, 1551 (2003).
- [172] H. Oberhofer, C. Dellago, and P. L. Geissler, *J Phys Chem B* **109**, 6902 (2005).
- [173] A. Imparato and L. Peliti, *Europhys. Lett.* **70**, 740 (2005).
- [174] U. Seifert, *Phys Rev Lett* **95**, 040602 (2005).
- [175] J. Liphardt, S. Dumont, S. B. Smith, I. Tinoco, and C. Bustamante, *Science* **296**, 1832 (2002).
- [176] F. Douarche, S. Ciliberto, A. Petrosyan, and I. Rabbiosi, *Europhys. Lett.* **70**, 593 (2005).
- [177] G. M. Wang, E. M. Sevick, E. Mittag, D. J. Searles, and D. J. Evans, *Phys Rev Lett* **89**, 050601 (2002).
- [178] V. Blickle, T. Speck, L. Helden, U. Seifert, and C. Bechinger, *Phys Rev Lett* **96**, 070603 (2006).
- [179] N. C. Harris, Y. Song, and C. H. Kiang, *Phys Rev Lett* **99**, 068101 (2007).
- [180] O. P. Saira, Y. Yoon, T. Tanttu, M. Möttönen, D. V. Averin, and J. P. Pekola, *Phys Rev Lett* **109**, 180601 (2012).

- [181] S. An, J. Zhang, M. Um, D. Lv, Y. Lu, J. Zhang, Z. Yin, H. T. Quan, and K. Kim, *Nat Phys* **11**, 193 (2014).
- [182] C. Jarzynski, *Phys Rev E Stat Nonlin Soft Matter Phys* **73**, 046105 (2006).
- [183] J. Gore, F. Ritort, and C. Bustamante, *Proc Natl Acad Sci U S A* **100**, 12564 (2003).
- [184] U. Cetiner and S. Sukharev, *bioRxiv* (2017).
- [185] T. Ursell, *Bilayer Elasticity in Protein and Lipid Organization*, Paperback; 2009-07-19 (VDM Verlag, 2009).
- [186] M. Sotomayor and K. Schulten, *Biophys J* **87**, 3050 (2004).
- [187] C. Jarzynski, *Comptes Rendus Physique* **8**, 495 (2007).
- [188] J. Horowitz and C. Jarzynski, *J. Stat. Mech.* **2007**, P11002 (2007).
- [189] F. Ritort, C. Bustamante, and I. Tinoco, *Proc Natl Acad Sci U S A* **99**, 13544 (2002).
- [190] C. H. Bennett, *J Comput Phys* **22**, 245 (1976).
- [191] M. R. Shirts, E. Bair, G. Hooker, and V. S. Pande, *Phys Rev Lett* **91**, 140601 (2003).
- [192] D. Frenkel, B. Smit, and M. A. Ratner, *Phys Today* **50**, 66 (1997).
- [193] J. Hermans, *J Phys Chem* **95**, 9029 (1991).
- [194] B. Efron, *Ann. Statist.* **7**, 1 (1979).
- [195] U. Cetiner and S. Sukharev, *BioRxiv* (2017).
- [196] M. Manosas and F. Ritort, *Biophys J* **88**, 3224 (2005).
- [197] J. D. Wen, M. Manosas, P. T. Li, S. B. Smith, C. Bustamante, F. Ritort, and I. Tinoco, *Biophys J* **92**, 2996 (2007).
- [198] M. Manosas, J. D. Wen, P. T. Li, S. B. Smith, C. Bustamante, I. Tinoco, and F. Ritort, *Biophys J* **92**, 3010 (2007).
- [199] F. Ritort, in *Advances in Chemical Physics*, edited by S. A. Rice (John Wiley & Sons, Inc., Hoboken, NJ, USA, 2007), pp. 31–123.
- [200] I. Rowe, A. Anishkin, K. Kamaraju, K. Yoshimura, and S. Sukharev, *J Gen Physiol* **143**, 543 (2014).
- [201] W. Grajkowski, A. Kubalski, and P. Kopyrowski, *Biophys J* **88**, 3050 (2005).
- [202] H. Machiyama, H. Tatsumi, and M. Sokabe, *Biophys J* **97**, 1048 (2009).
- [203] V. A. Parsegian, R. P. Rand, and D. C. Rau, *Meth Enzymol* **259**, 43 (1995).

- [204] V. A. Parsegian, R. P. Rand, and D. C. Rau, *Proc Natl Acad Sci U S A* **97**, 3987 (2000).
- [205] J. Zimmerberg and V. A. Parsegian, *Nature* **323**, 36 (1986).
- [206] J. Zimmerberg, F. Bezanilla, and V. A. Parsegian, *Biophys J* **57**, 1049 (1990).
- [207] G. Ehrenstein, H. Lecar, and R. Nossal, *J Gen Physiol* **55**, 119 (1970).
- [208] S. J. Schein, M. Colombini, and A. Finkelstein, *J Membr Biol* **30**, 99 (1976).